

# Silica passivation layer on aluminium brazing sheets

Inaugural-Dissertation

zur

Erlangung des Doktorgrades  
der Mathematisch-Naturwissenschaftlichen Fakultät  
der Universität zu Köln  
vorgelegt von

Kathrin Schäuble

aus Stuttgart

Köln 2010

Berichterstatter: Prof. Dr. Gerd Meyer  
Prof. Dr. Herman Terry

Prüfungsvorsitzender: Prof. Dr. Reinhard Strey

Schriftführer: Dr. Ingo Pantenburg

Tag der mündlichen Prüfung: 16.04.2010

## **Abstract**

*The request for more efficient fuel economy to save raw materials and to reduce air pollution becomes more and more crucial in the automotive industry. To fulfil this demand by weight reduction, conventional materials such as steel and copper are replaced by light metals. Due to its beneficial material properties e. g. low density, high strength, good formability and high thermal conductivity, aluminium becomes a frequently used candidate. Particularly in the heat-exchanger industry this change has already taken place. Heat-exchangers made of aluminium brazing sheets are used in various applications e. g. climate control, engine and transmission cooling and charge air cooling. Brazing sheets consist of a multilayer alloy system. A typical material combination in this field is an Al-Mn core alloy (AA3xxx) clad on one or both sides with an Al-Si alloy (AA4xxx). The benefit for this combination is given by the difference in the melting points of the two alloys. During the brazing process (around 590 °C) the core alloy provides structural integrity while the low melting point clad alloy melts and flows to provide upon cooling metallic bonding between the various components of the heat-exchanger.*

*Due to the various conditions that a heat-exchanger is exposed to during its service life such as heating and cooling cycles, salt water environment on the surface and mechanical loading, the corrosion performance is a crucial point since it might cause perforation of the material resulting in a complete failure of the system.*

*In order to understand the corrosion behaviour of the brazing sheets, it is necessary to have a deeper look at the microstructure, which is mainly determined by the composition of the alloying elements and heat treatments. The addition of alloying elements such as copper and iron provides beneficial material properties e. g. strength, good formability and brazeability, but can also change the corrosion mechanism from pitting, which is the preferred attack in pure aluminium, to more aggressive forms of localized attack, like intergranular and exfoliation corrosion. Furthermore thermal treatments such as solution heat treatment, aging, homogenisation or brazing significantly change the microstructure and hence modify the corrosion behaviour.*

*To fulfil the requested corrosion performance, which is usually performed by salt spray testing (SWAAT), it is often necessary to apply a pre-treatment on the heat-exchanger.*

*Besides protecting the aluminium brazing sheet of corrosion attack, the pre-treatment has to contain environmental friendly and low costs components.*

*After accelerated corrosion testing of AA4045/3003/4045 brazing sheets by SWAAT and electrochemical techniques, the corrosion propagation was attributed to potential differences within the brazing sheet causing a galvanically driven perforation of the core material by the diffusion zone. Furthermore a correlation between the SWAAT and potentiodynamic and potentiostatic polarization measurements is observed, offering a substitution of the SWAAT by these electrochemical techniques and hence reducing the testing time from several weeks (SWAAT) to less than one day.*

*Corrosion prevention is achieved by immersing of the brazing sheets in an aqueous sodium silicate solution. The resulting silica passivation layer consists mainly of a dense  $\text{SiO}_2$  network and provides a reduction of around 80% of the corrosion propagation during SWAAT exposure. It is shown that the barrier properties are dependent on the respective pre-treatments conditions such as bath concentrations, curing times, curing temperatures and dipping times.*

## **Zusammenfassung**

Aufgrund steigender Preise der verbleibenden Rohstoffe rückt ein effizienterer Treibstoffverbrauch in der Automobilindustrie immer mehr in den Mittelpunkt. Gewichtsreduktion ist eine Möglichkeit den Benzinverbrauch zu reduzieren um somit auch Umweltbelastung durch weniger Abgase zu minimieren. Besonders im Bereich der Wärmetauscherindustrie hat Aluminium konventionelle Materialien wie Kupfer und Stahl fast vollständig ersetzt. Eine hohe thermische Leitfähigkeit kombiniert mit einer geringen Dichte macht Aluminium zum idealen Material für den Gebrauch von Wärmetauschern. Heutzutage werden schätzungsweise 80% aller Fahrzeuge mit Aluminiumwärmetauschern bestehend aus Lotblechen ausgestattet.

Dieses Lotblech besteht aus einer Kernlegierung, die auf einer oder beiden Seiten mit einer Plattierschicht, bestehend aus einer anderen Aluminiumlegierung, umhüllt ist. Der Vorteil dieser Konstruktion liegt in den unterschiedlichen Schmelzpunkten der Legierungen. Während des Lötens schmilzt nur die Lotplattierung und dichtet aufgrund von wirkenden Kapillarkräften die Verbindungen beim Abkühlen ab. Im Gegensatz dazu, bleiben die Kernlegierungen in ihrer Form bestehen. Da Wärmetauscher während ihrer Laufleistung unterschiedlichen korrosiven Medien von Innen (Kühlmittel) als auch von Außen (Kondensationswasser) ausgesetzt sind, ist die Korrosionsbeständigkeit des Materials ein sehr wichtiger Faktor.

Die Korrosionseigenschaften werden durch die Mikrostruktur bestimmt, die hauptsächlich durch die zugefügten Legierungselemente und die durchgeführten Wärmebehandlungen (z. B. Homogenisierung, Alterung, Löten) charakterisiert ist. Die hohen Temperaturen während des Lötvorgangs fördern die Diffusion verschiedener Legierungselemente ins Materialinnere oder in Richtung der Oberfläche. Si wandert von der Lotlegierung in Richtung der Kernlegierung und initiiert dabei die Ausscheidung von manganhaltigen Partikeln. Die hohe Partikeldichte in diesem Bereich reduziert das Korrosionspotential und verursacht somit eine erhöhte Korrosionsrate. In den neueren Generationen von Legierungen (long life alloys) wird diese vermehrte Ausscheidung gefördert und somit eine bevorzugte Auflösung der Lotplattierung bzw. Diffusionszone initiiert um den Angriff der Kernlegierungen zu verhindern und damit eine Perforation des Wärmetauschers zu vermeiden.

Ebenso kann der Korrosionsschutz durch eine passende Vorbehandlung erfolgen. Wichtig dabei ist vor allem eine kostengünstige und umweltfreundliche Anwendung. Eine oft verwendete Komponente, die diesen Anforderungen entspricht sind Silikatverbindungen. Auf Materialien wie Stahl, Kupfer und Zink haben sich die Silikatbeschichtungen bereits bewährt. Jedoch sind aufgrund der Komplexität der Silikatchemie noch viele Fragen weitgehend unbeantwortet. Auch sind bis jetzt kaum Untersuchungen durchgeführt worden, um die Kompatibilität der Silikatbeschichtungen auf Aluminiumsubstraten zu analysieren.

Ein Standardtest für die Korrosionsbeständigkeit für Aluminiumwärmetauscher ist der so genannte sea water acetic acid test (SWAAT). Dieser Salzsprühtest dient dazu die Betriebsbedingungen naturgetreu zu simulieren und einen beschleunigten Korrosionsangriff zu initiieren. In der Industrie als Qualitätstest oft verlangt, zeigt dieser Test jedoch trotzdem deutliche Schwächen aufgrund der geringen Reproduzierbarkeit und abhängig von der Materialqualität eine relative lange Testdauer von bis zu mehreren Wochen.

Nach ausführlichen Korrosionstests (Salzsprühtests und Polarisationsmessungen) konnte die Korrosionsursache in Potenzialdifferenzen innerhalb der Lötplatten ermittelt werden. Diese unterschiedlichen Korrosionspotenziale bewirken eine galvanische Auflösung des unedleren Kernmaterials durch die edleren Bereiche der Diffusionszone beziehungsweise der Lotplattierung. Ein Vergleich der Korrosionsergebnisse mittels der Salzsprühtests und den elektrochemischen Messmethoden zeigte den gleichen Korrosionsverlauf. Diese Korrelation ermöglicht es die Dauer des Korrosionstests von teilweise mehreren Wochen (Salzsprühtests) auf wenige Stunden (elektrochemische Methoden) zu reduzieren.

Die Aufbringung der hydrophilen Silikatpassivierungsschicht auf die Aluminium Lotplatten zeigte bis zu 80% weniger Korrosionsangriff während des Salzsprühtests. Diese Schutzfunktion ergibt sich aufgrund der dicht vernetzten SiO<sub>2</sub>-Struktur innerhalb der hydrophilen Passivierungsschicht. Die im Rahmen dieser Arbeit getesteten Beschichtungsbedingungen (Badkonzentration, Härtungstemperatur, Härtungszeit und Abscheidungszeit) zeigten einen Einfluss auf die Qualität der Passivierungseigenschaften der Silikatschichten.

<b>I.</b>	<b>INTRODUCTION .....</b>	<b>2</b>
<b>I.1</b>	<b>Background .....</b>	<b>2</b>
<b>I.2</b>	<b>Outline of the thesis .....</b>	<b>5</b>
<b>II.</b>	<b>STATE OF THE ART.....</b>	<b>9</b>
<b>II.1</b>	<b>Aluminium brazing sheets in automotive application .....</b>	<b>9</b>
<b>II.2</b>	<b>Production of aluminium brazing sheets.....</b>	<b>10</b>
<b>II.3</b>	<b>Influence of the brazing process on the microstructure .....</b>	<b>11</b>
<b>II.4</b>	<b>Corrosion of aluminium and its alloys.....</b>	<b>14</b>
<b>II.5</b>	<b>Types of corrosion.....</b>	<b>18</b>
II.5.1	Uniform corrosion .....	18
II.5.2	Pitting corrosion .....	18
II.5.3	Transgranular and intergranular corrosion .....	20
II.5.4	Corrosion of aluminium brazing sheets: re-solidified clad .....	22
II.5.5	Corrosion of aluminium brazing sheets: core material .....	22
<b>II.6</b>	<b>Accelerated corrosion testing.....</b>	<b>25</b>
II.6.1	SWAAT.....	25
II.6.2	Electrochemical investigation .....	25
<b>II.7</b>	<b>Anti-corrosion coating for aluminium: silica passivation layer .....</b>	<b>26</b>
II.7.1	Chemistry of silica.....	27
II.7.2	Water Soluble silica: sodium silicate.....	29
<b>III.</b>	<b>EXPERIMENTAL .....</b>	<b>37</b>
<b>III.1</b>	<b>Introduction .....</b>	<b>37</b>
<b>III.2</b>	<b>Substrate .....</b>	<b>37</b>

<b>III.3</b>	<b>Pre-treatment of the samples .....</b>	<b>38</b>
<b>III.4</b>	<b>Mechanical transformation of the aluminium substrates.....</b>	<b>38</b>
<b>III.5</b>	<b>Deposition of the passivation layer .....</b>	<b>40</b>
III.5.1	Sodium silicate solution .....	40
III.5.2	Diluting sodium silicate solution .....	40
III.5.3	Silicate film deposition .....	40
<b>III.6</b>	<b>Accelerated corrosion testing.....</b>	<b>42</b>
III.6.1	Sea Water Acetic Acid Test (SWAAT).....	42
III.6.2	Electrochemical techniques .....	43
<b>III.7</b>	<b>Analytical methods.....</b>	<b>44</b>
III.7.1	Scanning Electron Microscopy (SEM).....	44
III.7.2	X-ray Photoelectron Spectroscopy (XPS) .....	45
III.7.3	Raman Spectroscopy.....	45
<hr/>		
<b>IV.</b>	<b>ACCELERATED CORROSION TESTING.....</b>	<b>49</b>
<b>IV.1</b>	<b>Introduction .....</b>	<b>49</b>
<b>IV.2</b>	<b>Characterization of the material.....</b>	<b>50</b>
IV.2.1	Microstructure after mechanical transformation .....	54
<b>IV.3</b>	<b>Morphological results of AA4045/3003/4045 during SWAAT exposure.....</b>	<b>55</b>
<b>IV.4</b>	<b>Electrochemical analysis.....</b>	<b>57</b>
IV.4.1	Recording the Open-Circuit-Potential (OCP) of aluminium brazing sheets.....	58
IV.4.2	Potentiodynamic polarization curves of aluminium brazing sheets .....	61
IV.4.3	Morphology of attack after OCP measurements.....	63
IV.4.4	Morphology of attack after potentiodynamic polarization scans .....	63
IV.4.5	Morphology of attack after potentiodynamic polarization at the 1st and 2nd breakdown potential	65
IV.4.6	Potentiostatic polarization at the breakdown potentials .....	66
IV.4.7	Comparison of corrosion propagation by potentiostatic polarization and SWAAT.....	68
IV.4.8	Effect of brazing temperature on the open circuit potential.....	70
IV.4.9	Effect of brazing temperature on the potentiodynamic polarization .....	71
IV.4.10	Effect of the brazing temperature on the morphology of attack.....	72
IV.4.11	Effect of mechanical transformation on the open circuit potential.....	75

IV.4.12	Effect of mechanical transformation on the potentiodynamic polarization .....	76
IV.4.13	Effect of mechanical transformation on the morphology of attack .....	77
<b>IV.5</b>	<b>Conclusion.....</b>	<b>77</b>
<hr/>		
<b>V.</b>	<b>INVESTIGATION OF THE SODIUM SILICATE PASSIVATION LAYER ....</b>	<b>83</b>
<hr/>		
<b>V.1</b>	<b>Introduction .....</b>	<b>83</b>
<b>V.2</b>	<b>Raman analysis .....</b>	<b>84</b>
V.2.1	Sodium silicate in aqueous solution: .....	84
V.2.2	Deposition of sodium silicate on aluminium:.....	85
V.2.3	Discussion.....	86
<b>V.3</b>	<b>Morphology of the aluminium surface after deposition of sodium silicate .....</b>	<b>87</b>
<b>V.4</b>	<b>Thickness of the passivation layer .....</b>	<b>95</b>
<b>V.5</b>	<b>Mechanism of the deposition.....</b>	<b>97</b>
<b>V.6</b>	<b>In-situ OCP measurements .....</b>	<b>99</b>
<b>V.7</b>	<b>Discussion.....</b>	<b>100</b>
<b>V.8</b>	<b>Constitution of the silicate passivation layer .....</b>	<b>101</b>
V.8.1	XPS analysis .....	102
V.8.2	Structure of the silica layer .....	105
<b>V.9</b>	<b>Uniformity of the silica passivation layer after deposition on aluminium substrates.....</b>	<b>112</b>
V.9.1	Discussion.....	114
<b>V.10</b>	<b>Conclusion.....</b>	<b>116</b>
<hr/>		
<b>VI.</b>	<b>BARRIER PROPERTIES OF THE SILICA COATING.....</b>	<b>120</b>
<hr/>		
<b>VI.1</b>	<b>Introduction .....</b>	<b>120</b>
<b>VI.2</b>	<b>SWAAT performance of pre-treated aluminium substrates.....</b>	<b>120</b>
<b>VI.3</b>	<b>Breakdown of the passivation layer.....</b>	<b>125</b>
<hr/>		

<b>VI.4</b>	<b>Electrochemical measurements.....</b>	<b>126</b>
VI.4.1	Potentiodynamic polarization curves on coated AA4045/3003/4045 brazing sheets .....	127
VI.4.2	Potentiodynamic polarization curves on coated Al99,99% .....	129
VI.4.3	Potentiostatic polarization curves with Al 99.99% .....	130
<b>VI.5</b>	<b>Conclusion.....</b>	<b>137</b>
<hr/>		
<b>VII.</b>	<b>CONCLUSIONS.....</b>	<b>140</b>

---

## CHAPTER ONE

---

# INTRODUCTION

# I. INTRODUCTION

## I.1 Background

A very important aspect in the automotive industry is the reduction of overall weight in a vehicle, in order to reduce the impact on fuel economy. It is estimated that a 10% reduction of weight results in 8-10% improvement of fuel economy<sup>1</sup>. This makes aluminium a frequently used candidate to substitute heavier materials such as steel and copper.

The use of aluminium is already widespread in the sector of heat-exchangers. They are made of aluminium brazing sheets and are used for engine and transmission cooling, charge air coolers and climate control<sup>1</sup>. The most common combination of alloys within a brazing sheet, used in heat-exchangers, is an aluminium-manganese core alloy (AA3xxx series) clad on one or both sides with an aluminium-silicon alloy (AA4xxx series). The benefit of this combination is due to the lower melting point of the Al-Si alloy<sup>2</sup>. This property ensures proper joining conditions between the different parts e. g. tubes and fins of the heat exchanger during the brazing process. A schematic representation is given in Figure I.1-1.

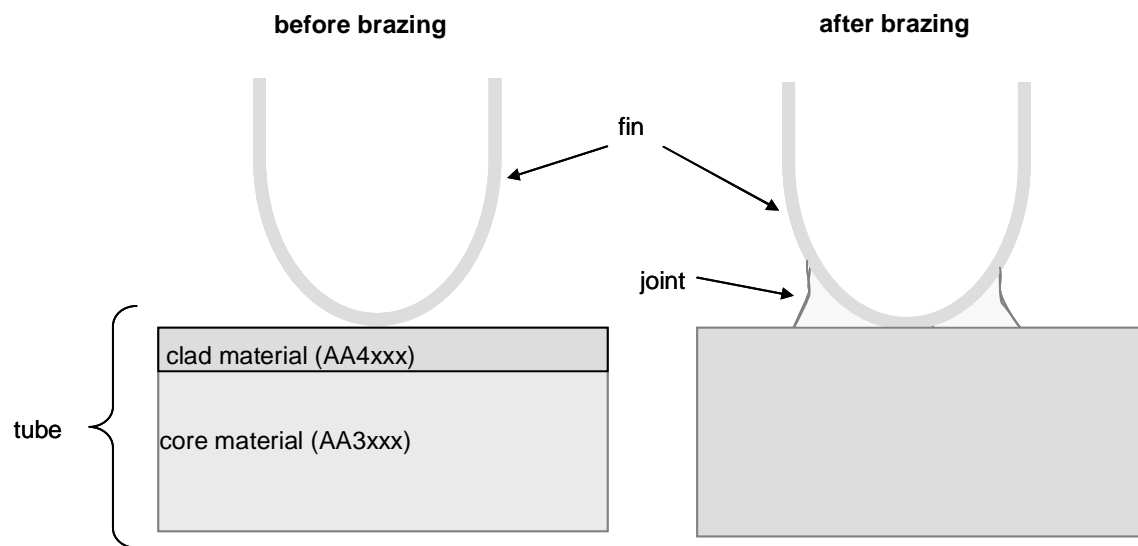


**Figure I.1-1:** Schematic principle of joining with brazing sheet.

The requirements in terms of material properties for aluminium brazing sheets are quite diverse and depend on the application they are produced for. Strong corrosion resistance is one of the key requests that a brazing sheet has to fulfil.<sup>1</sup> Particularly in the life time of a heat-exchanger, corrosion is a crucial point, since the perforation of the material by corrosion attack results in a complete failure of the system due to leaking of the cooling liquid.<sup>3</sup>

In order to understand the corrosion behaviour of the brazing sheets, it is necessary to have a deeper look at the microstructure, which is mainly determined by the composition of the alloying elements and heat treatments. Hence, several publications can be found on the influence of alloying elements and heat treatments<sup>4,5,6,7</sup> on the microstructure. The addition of alloying elements such as copper and iron can change the corrosion mechanism from pitting, which is the preferred attack in pure aluminium, to more aggressive forms of localized attack, such as intergranular and exfoliation corrosion. Furthermore thermal treatment such as solution heat treatment, aging, homogenisation or brazing might significantly change the microstructure. This is associated to a modification of the corrosion behaviour.<sup>8,9,10,11,2</sup>

During brazing silicon diffuses into the core material and precipitates in small particles together with aluminium and manganese in an area between the core and clad material. This area, which is called the band of dense precipitates (BDP) has a lower corrosion potential than the core material and acts as a sacrificial layer, keeping the corrosion in the outer layer and preventing the perforation of the material.<sup>1</sup> A schematic illustration of the diffusion process is presented in Figure I.1-2. This beneficial behaviour as sacrificial anode of the clad material and the diffusion zone, is used in the newer generation of the brazing sheets, the long life material. However for the conventional alloys the diffusion zone is not significant and hence the corrosion propagates into the core material. In order to overcome this behaviour a specific pre-treatment is necessary to protect the system against corrosion and to ensure a long service life. Besides a strong corrosion resistance, the pre-treatment is environmentally friendly and consists of readily available and inexpensive materials. Combining all these properties, sodium silicates have been used as corrosion inhibitors for steel and galvanized steel for years<sup>12,13,14</sup> but have not been applied on aluminium substrates.

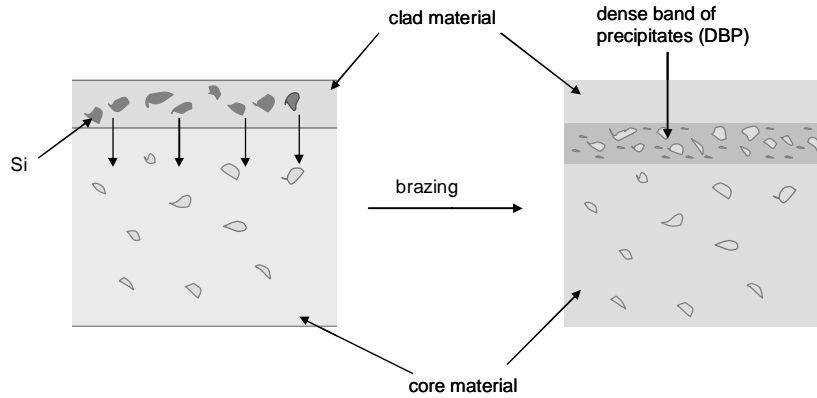


**Figure I.1-2:** Schematic illustration of the diffusion process of the alloying elements occurring during the brazing cycle.

The conditions for the lifetime of a heat exchanger are simulated in salt spray tests to gain information about the corrosion performance. The standard accelerated corrosion test for aluminium is the sea water acetic acid test (SWAAT), which simulates lifetime service. Although it is often requested as quality control in the industry it presents some drawbacks such as its long duration and low reproducibility.<sup>2</sup>

In the first section of this thesis, the corrosion behaviour of AA4045/3003/4045 brazing sheets has been extensively investigated by means of conventional salt spray testing (SWAAT) and electrochemical techniques such as open circuit potential (OCP), potentiodynamic polarization and potentiostatic polarization measurements. These techniques overcome the drawbacks of the SWAAT and enable an investigation of the corrosion behaviour of the material. During this study the focus was given to localized attack (pitting, intergranular corrosion).

Section two deals with the deposition of a silicate passivation layer on aluminium. The focus was on the effect of the deposition conditions on the uniformity of the silicate layer. Finally in section three the barrier properties of the silicate passivation layer are investigated. This part presents the link between the characterization of the corrosion behaviour of the bare material and the corrosion performance of the coated material and deals with the characterization of the passivation layer.

## I.2 Outline of the thesis

Figure I.2-1 presents the layout of the thesis. The thesis is divided in three main parts:

1. State of the art
2. Results and discussion
3. Conclusions

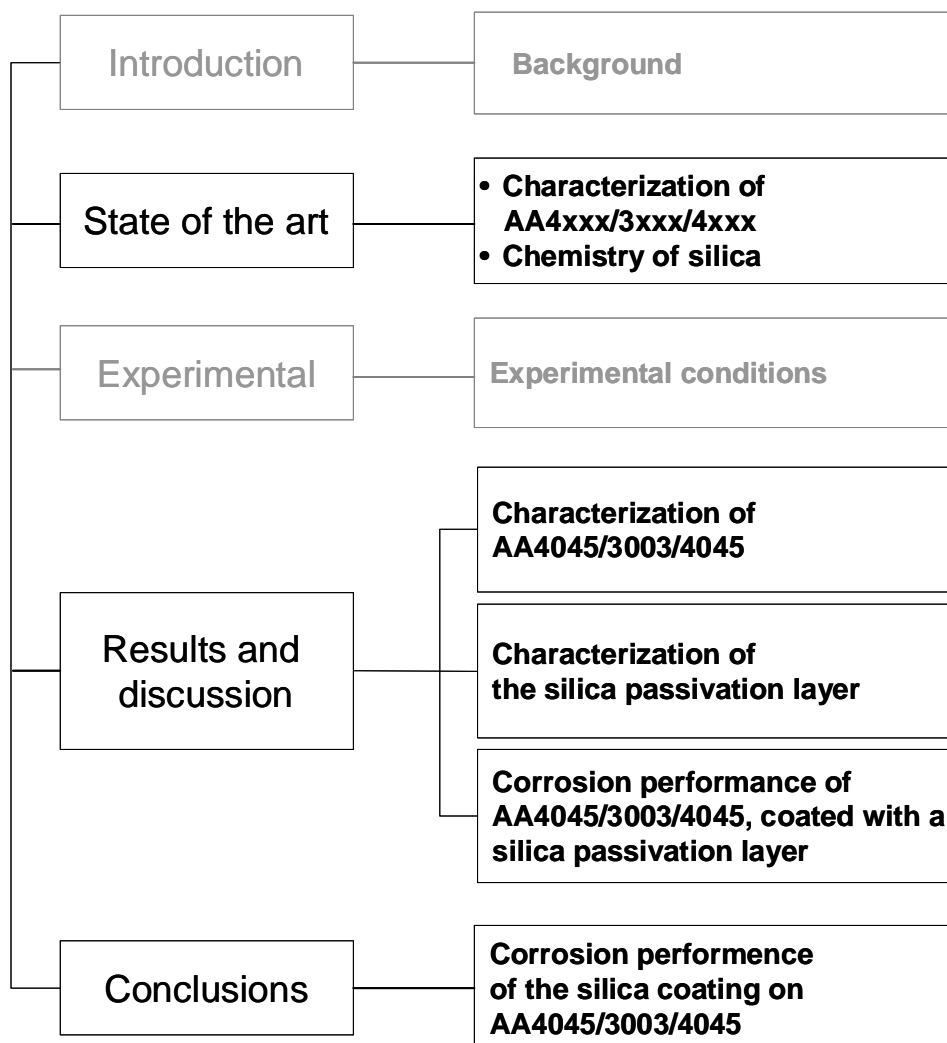


**Figure I.2-1:** Layout of the thesis.

State of the art covers two main parts. The first part is focused on the literature of the microstructure and electrochemical properties of AA4xxx/3xxx/4xxx brazing sheets. The second part deals with the chemistry of silica in aqueous solution and deposited on a surface.

The section Results and discussion is divided in three chapters that contain the experimental approach of this work. The first section reports the correlation between the microstructure and the corrosion behaviour of AA4045/3003/4045 brazing sheets, investigated by conventional salt spray testing (SWAAT) and electrochemical techniques. In addition it introduces potentiodynamic and potentiostatic polarization scans as an alternative to the SWAAT. The second part is dedicated to the chemistry of silica in aqueous solution and deposited on aluminium. Particularly the chemical state of the layer after deposition on the substrate is the focus of the discussion. In the third part the corrosion performance of AA4045/3003/4045 coated with the silicate passivation layer is discussed. This chapter is the link between the characterization of the brazing sheets (Chapter IV) and the chemistry of silica (Chapter V). Moreover the correlation between the deposition conditions and the barrier properties are reported.

Finally the conclusions are presented in Chapter VII, the electrochemical behaviour of bare AA4045/3003/4045 brazing sheets and of the same substrate coated with a silica passivation layer.

---

## CHAPTER TWO

---

State of the art

### **Abstract**

*Since this thesis is divided in three parts, the state of the art reveals an overview about the different fields. The first section is dedicated to aluminium brazing sheets. Particularly the morphological as well as the electrochemical properties will be in the focus. The second section deals with the chemistry of silica. Since the silica chemistry is very complex and involved in various fields, this review sticks to the applications concerning this work. For this purpose the focus is on the conditions of sodium silicates in aqueous solution and the deposition of sodium silicates on a solid surface. The last section is attributed to the barrier properties of sodium silicates after deposition on a metal surface.*

## II. State of the art

### II.1 Aluminium brazing sheets in automotive application

There is a great demand to reduce the weight of vehicles due to the trend for reduction of energy consumption and air pollution in automotive industry. To satisfy this request light metals like aluminium are widely used in various parts of a vehicle. For heat exchanger application an assembly of AA4xxx/3xxx/4xxx alloys (**Figure II.1-1 B**) is very common<sup>15</sup>. From the aluminium manufacturing industry the brazing sheets are usually delivered as coils (**Figure II.1-1 A**) to the processing industry. These coils are produced in various lengths and widths.<sup>16</sup> **Figure II.1-1** presents a schematic illustration of the aluminium brazing sheets (B) produced as coils (A).

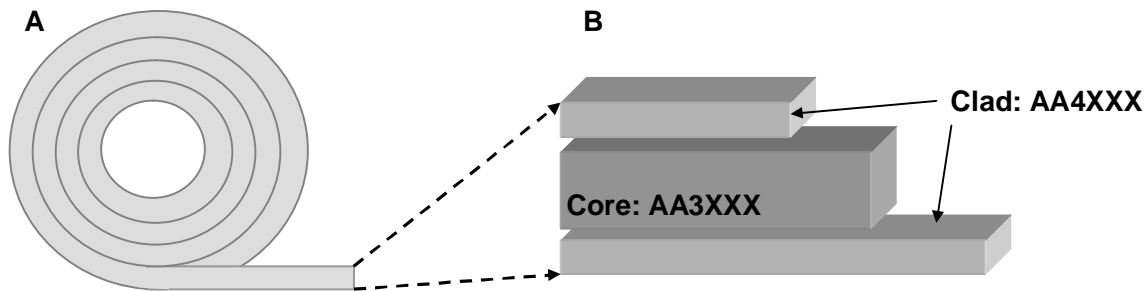


**Figure II.1-1:** Schematic illustration of brazing sheets (B) produced as coils (A).

The beneficial effect of an aluminium manganese core alloy (AA3xxx series) sheathed with an Al-Si clad alloy (AA4xxx series) is based on the difference in melting points. By reaching the final temperature during the brazing process the clad alloy is completely molten and ensures proper joining properties between the different parts of the heat exchanger whereas the core alloy provides constant material properties<sup>2</sup>. Among good brazeability properties, the most crucial factors for the quality of brazing sheets are corrosion resistance, formability and strength. In the following sections these factors will be considered in detail.

## II.2 Production of aluminium brazing sheets

Figure II.2-1 illustrates a schematic of the main production steps of aluminium brazing sheets, consisting of a 3xxx core alloy clad on both sides with a 4xxx alloy.

In the first step the ingots of the different alloys are cast (1). Depending on the final application of the material, the ingots are either homogenised at elevated temperatures or produced without this step. The heat treatment is required for high strength alloys, since it provides the elements time to diffuse and order themselves in a more stable state. However homogenisation increases the susceptibility to localized attack since the alloying elements precipitate in the grain boundaries increasing the potential differences between the different phases in the microstructure. The braze filler material (AA4xxx) is attached to the core alloy (AA3xxx) through warm and cold rolling steps, respectively (2). Usually the clad material is a very thin layer, having a thickness of approximately 5-10% of the total gauge.

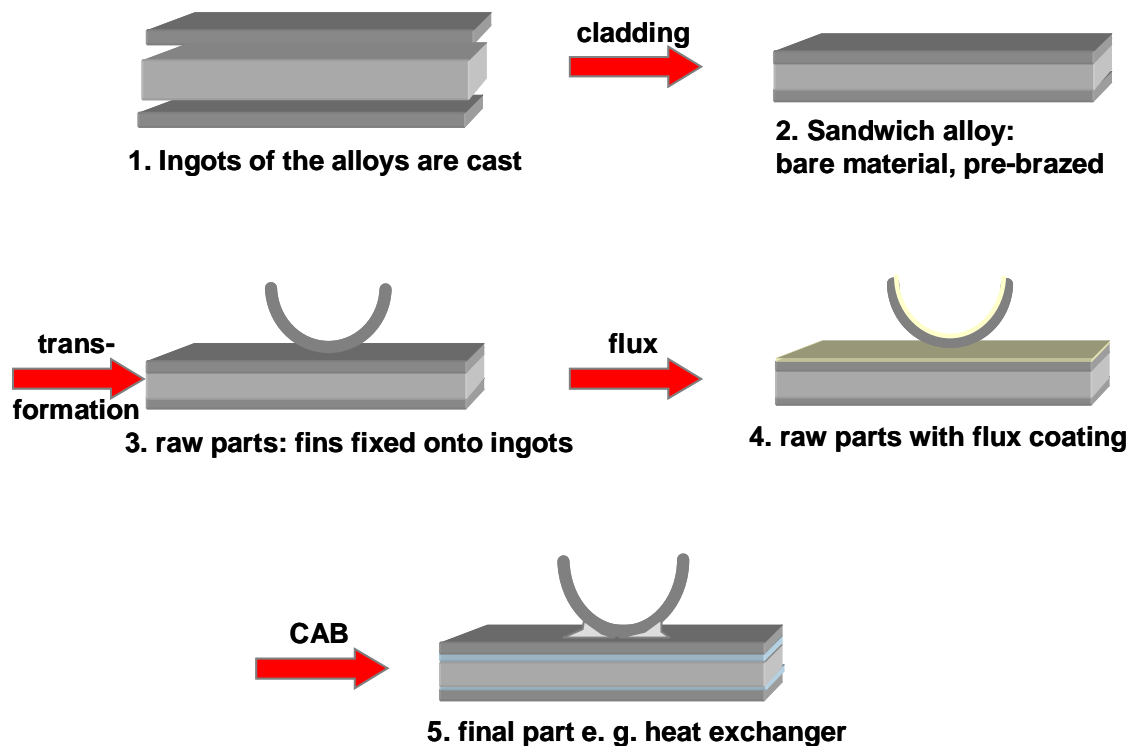


Figure II.2-1: Schematic about a production line for aluminum brazing sheets.

During the aluminium processing the wrought products are mechanically transformed e. g. by deep drawing, to apply the designated shape (3). Usually three different parts are used in a heat-exchanger:

**Tube:** the tubes are used for distributing the cooling liquid in the system. Hence a perforation by corrosion attack in that part results in a breakdown of the entire system. The tubes are made of brazing sheets having a thickness of 0.2 – 0.4 mm.

**Fin:** the fins are attached to the tubes to enlarge the surface of the system and hence to ensure an efficient heat exchanging. They are normally made of the core material, having a thickness of around 0.1 mm. Quite often the fins act as sacrificial anodes for the tubes.

**Header plate:** the header plates are located at both sides as final plates of the heat-exchanger. Since they give the strength at the outer parts of the system the thickness of these plates is significant higher compared to the tubes and fins.

Prior to the brazing process the raw parts are coated with flux (4). The heater cores used for this work were treated with Nocolok-Flux® from Solvay. This solution contains various potassium fluorides compounds ( $KAlF_4$ ,  $K_2AlF_5$ ) and is applied via spraying. The high temperatures (580 - 600°C) during the Controlled Atmosphere Brazing (CAB) process melt the flux and the fluoride components remove the oxide layer of the (aluminium) substrate. This behaviour ensures connection between the bare metal substrates within the system<sup>17</sup>. In the same way the clad material melts and provides a proper metallic bonding between the different parts of an evaporator. On the other hand, due to the higher melting point of AA3xxx the specific structure of the core material is kept<sup>18</sup> (5).

### II.3 Influence of the brazing process on the microstructure

In recent years the brazing technique for joining metal parts has been used more and more, replacing the mechanical assembly in mass production<sup>16</sup>. Cost and safety reasons as well as good recycling properties initiated this change, due to lower working temperature during brazing in comparison to soldering and welding.

Up to a brazing temperature of 560°C there is an equal heat distribution between the filler alloy, the core material and the flux layer. Increasing the temperature the flux begins to

melt and at around 575°C it starts to remove the oxide layer, to ensure a uniform wetting. At 577°C the filler material begins to melt and finally at around 590°C (depending on the filler alloy) it is completely molten and distributed by the capillary forces over the surface. The temperature is kept constant for around 4 minutes. During that time, diffusion of the alloying elements occurs and the diffusion zone at the interface clad/ core is formed. After re-solidification of the filler material an increased amount of the clad material covers the formed brazed joints and a thin film is distributed on the remaining surface.

Although the total gauge of the brazing sheet remains constant during the brazing process<sup>19</sup>, there is a strong modification on the metallurgical phases during the heat treatment. Changing the microstructure of the core and the clad material influences the mechanical (formability and strength) as well as the physical properties (density and conductivity) of the brazing sheet.

### Influence of the brazing process on the clad alloy

Meijers et al.<sup>2</sup> investigated the solidification of an AA4xxx filler alloy after the brazing process and defined the most important properties. Hereby the growth of  $\alpha$ -aluminium dendrites starts at the core-filler interface, due to the good nucleation sites of primary aluminium dendrites. The various amount of silicon in solid solution ( $[Mn]_{ss}$ ) reaches a maximum at the eutectic temperature of 577° C. This behaviour is presented in the Al-Si phase diagram (Figure II.3-1).

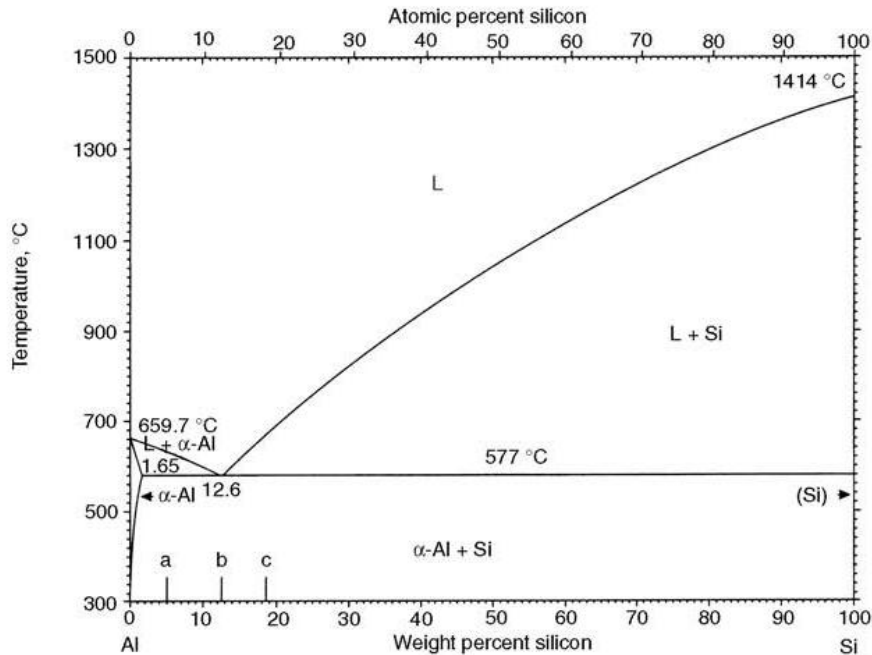


Figure II.3-1: Aluminium-Silicon equilibrium diagram<sup>16</sup>

Since the dendrites grow with decreasing temperature, their amount of silicon increases. This means that increasing silicon content gradually follows the growing direction from the nucleation to the edges. At the eutectic the silicon content is 12,6wt%, hence this is the last part to solidify. In this area the structure consists of alternating  $\alpha$ -aluminium plates and silicon. However the aluminium grains in the eutectic have a different composition, since all residual elements will be present either in solid solution in the aluminium located in the eutectic or precipitate as small intermetallics.

#### Influence of the brazing process on the core alloy and on the phase transformation

AA3xxx series, which are frequently used as core alloys contain manganese as the main alloying element. Further elements can be iron, magnesium, copper, zinc and silicon. In the literature the main intermetallic phases found in the 3xxx series contain Al-Fe-Mn. Due to the low amount of Si in the core alloy, hardly any silicon containing particles are observed.<sup>15</sup> Before brazing the core alloy mainly contains  $Al_6(Fe,Mn)$  precipitates. After brazing this is still the case in the core material but due to the inward diffusion of silicon from the clad material, large quantities of  $\alpha$ -AlMnSi precipitates have formed and are visible as a dense band of precipitates (DBP). Besides, (Al), Si,  $\alpha$ -Al(Fe,Mn)Si and

$\text{Al}_6(\text{Mn,Fe})$  are found in the brazed material. This diffusion process is described in detail in the literature.<sup>20,21</sup> Tierce et al.<sup>15</sup> observed different areas where the brazing process shows various influence on the change of the microstructure. The dominant phase in all areas was cubic  $\alpha\text{-Al}(\text{Fe,Mn})\text{Si}$  in various shapes.

In the area of the brazed joint, it was present either as Chinese script and blocklike precipitate.

In the residual clad, the heterogeneous phase is present as plates within aluminium grains and again as blocklike precipitates in the grain boundaries. In an additional investigation of Lacaze and Tierce<sup>18</sup> they found that this part, observed as a white film covering the flat surface, appears through re-solidification of the remaining molten cladding. They assume that the formation of the aluminium grains on the surface appears during the re-solidification process and the valleys between the grains develop through solidification shrinkage.

The third area was observed away from the brazed joint. Small precipitates were found, which is called 'band of dense precipitates' (BDP). This band appears due to silicon diffusion from the molten clad to the core material. It can be clearly seen in the modification of  $\text{Al}_6(\text{Mn,Fe})$  precipitates, being mainly present in the core material before the brazing step. During brazing and the resulting diffusion due to the high temperature, they show additional silicon and are mainly modified to  $\alpha\text{-Al}(\text{Fe,Mn})\text{Si}$  precipitates. This is confirmed by the observation of Alexander et al.<sup>22</sup> during homogenisation of AA3xxx aluminium alloys.

The thickness of the BDP is given by the diffusion depth of silicon (usually between 20 and 60  $\mu\text{m}$ ), which is in turn dependent on the heat treatment (temperature and time) during the brazing process.

### II.4 Corrosion of aluminium and its alloys

This section aims a short introduction of the general corrosion behaviour of aluminium substrates. The focus is given to localized attack (pitting, intergranular corrosion) since these types of corrosion are of crucial importance in the brazing sheets. Furthermore a detailed discussion about the corrosion properties of the brazing sheets will be given.

Due to its strong affinity to oxygen, aluminium has a strong corrosion resistance.<sup>23</sup> Once freshly produced aluminium being in contact with the atmosphere, the surface is immediately covered by a thin, but dense natural oxide layer. The structure of the films is dependent on the atmospheric conditions. Layers formed under low temperatures and dry air usually consist of an amorphous structure of aluminium oxide and reach a thickness of 2 to 3 nm during a few minutes. This process is limited to around 6-8 nm after a few days. At higher temperatures (above 450°C) the kinetics of the growth are increased and the amorphous layer transforms in crystalline  $\gamma$ -Al<sub>2</sub>O<sub>3</sub>. In moist air, the oxide layer grows very fast and consists of two layers. Next to the bulk material a barrier layer, consisting of dense, amorphous aluminium oxide is built up and on top, a porous, hydrous covering layer is connected, containing some crystalline parts of Al(OH)<sub>3</sub>.

A breakdown of the natural oxide layer can result from chemical attack, like anions and/or mechanical damage. Depending on the moisture in the environment, once the oxide layer is damaged new oxide is built on the following way to cover the bare material by the following reactions:

1) dissolution of aluminium at the anode:



2) hydrogen evolution and oxygen reduction occurs at the cathode:



Once the solubility product is exceeded, aluminium hydroxide is deposited at the corroded area, blocking the further corrosion attack.

Corrosion can be defined as the reaction between a metal and its surrounding environment, causing a visible change of the metal. Usually this is based on electrochemical reasons, but also chemical or metallurgical causes are possible.

The corrosion is mainly influenced

- on the aggressiveness of the electrolyte,
- by the chemical and metallurgical structure of the material,
- on local potential shifts
- on surface conditions
- by bi-metallic contacts.

Very important for the corrosion resistance of the native oxide layer is the pH of the electrolyte. Figure II.4-1 shows the correlation between pH ranges and solubility of the protective oxide layer in a Pourbaix diagram of aluminium.

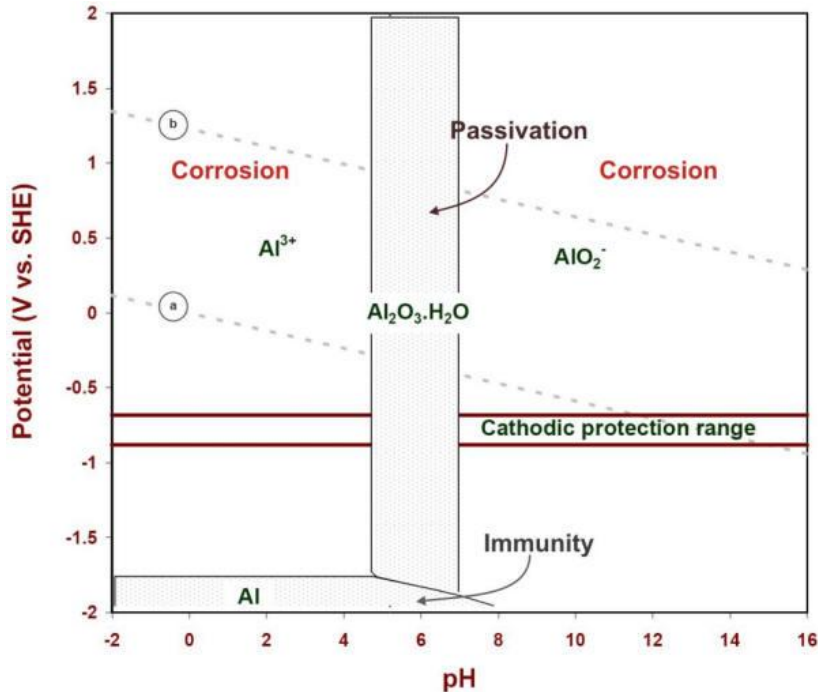


**Figure II.4-1:** Pourbaix diagram of aluminium.<sup>16</sup>

Between pH 4.5 and 8.5 the layer is to a large extent insoluble, which means the metal is protected against corrosion. Also in the region labelled as immune, the oxide film protects against corrosion. However in the region with a pH less than 4.5 or higher than 8.5 the metal is thermodynamically stable as ionic (soluble) product and therefore susceptible to corrosion attack.

The highest corrosion resistance is found at pure aluminium (Al99,99%) which decreases with increasing amount of alloying elements. For instance magnesium and silicon reduce the corrosion resistance only slightly, whereas copper and a combination of iron and silicon have a strong detrimental influence on the corrosion behaviour. A correlation of some alloying elements on the corrosion behaviour is given in Figure II.4-2.

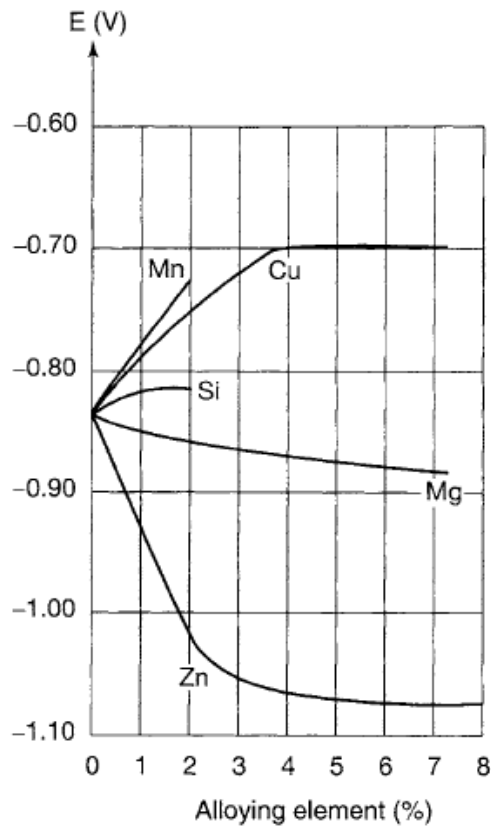


Figure II.4-2: Influence of alloying elements on the corrosion potential of aluminium.<sup>24</sup>

Besides the type, concentration and distribution of alloying elements in the aluminium matrix play an important role. Since heat treatments and mechanical transformations are mainly responsible for the structure of metallurgical phases, involving the alloying elements, this are also factors influencing the corrosion behaviour. Heat treatments can cause internal tensions through intermetallic phases in over-saturated aluminium alloys. Being aware of that, intergranular- and/ or stress-corrosion cracking can be avoided. In liquid aluminium the alloying elements are entirely soluble, however in the solid state there are limits of the solubility. Usually hard and brittle heterogeneous structural constituents are built through the alloying elements or in combination with aluminium, constructing intermetallic phases. These failures in the aluminium matrix determine the chemical and physical properties of the material.<sup>25</sup> To estimate the effects of the alloying elements equilibrium diagrams are considered. However these diagrams are showing the

equilibrium state, which can, for instance due to supersaturation caused by fast cooling rates differ from the real behaviour.

Another factor on corrosion is the roughness of the surface. Increasing the roughness of a surface decreases the corrosion resistance. Furthermore the uniformity of the surface is very important. Areas of different roughness can be the weakest point for starting the corrosion at the rougher side. Besides that a high surface roughness can cause failures in coating systems due to various thicknesses of passivation layers.

### II.5 Types of corrosion

#### II.5.1 Uniform corrosion<sup>16</sup>

Especially in an acidic and alkaline environment, the native oxide layer reveals a high solubility. Under these conditions small pits (diameter of around one micrometer) can develop well distributed over the entire surface. The uniform and continuous decrease in thickness of the metal can be measured through determining the mass loss.

#### II.5.2 Pitting corrosion<sup>25</sup>

The localized form of corrosion starts at various sites on the surface, where a defect of the oxide layer occurs. Irregularly shaped pits and cavities are formed and cause a roughened and less reflective surface. Pitting corrosion occurs if there is contact with aqueous media, like water and moisture. Another accelerating factor is chloride. A schematic illustration of the initiation and propagation of pitting corrosion is given in Figure II.5-1.

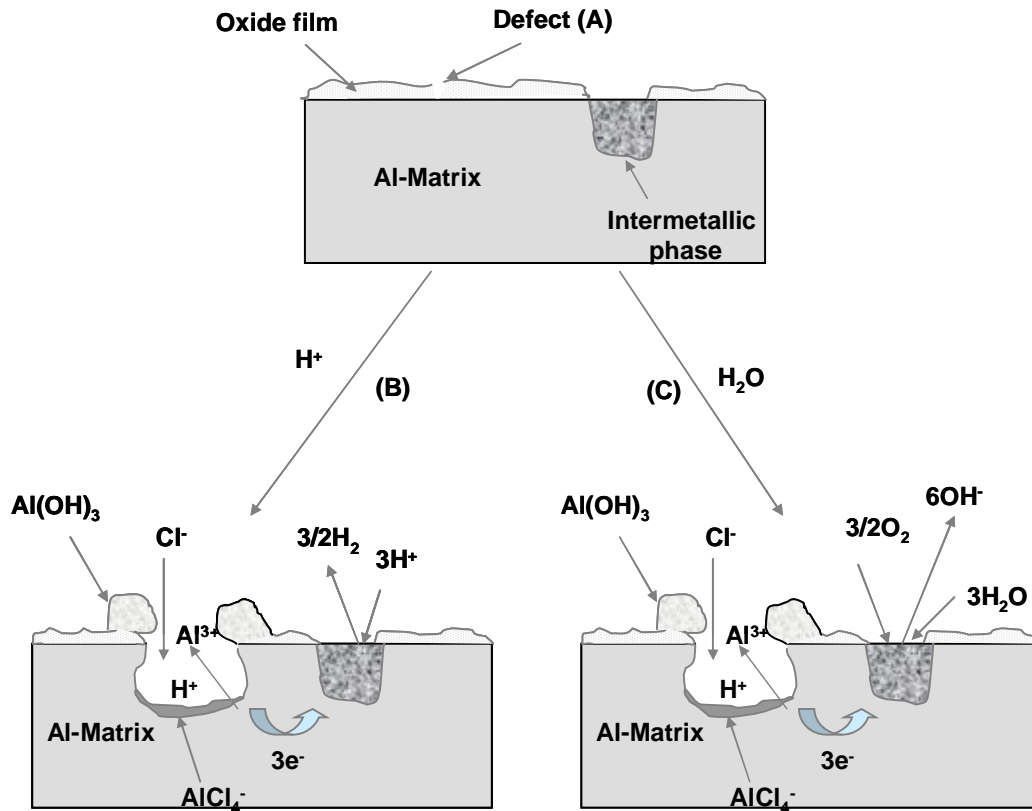


Figure II.5-1: Schematic illustration concerning the initiation and propagation of pitting.

First the chloride ions adsorb on the surface, preferentially at weak points of the natural oxide layer (A). Microcracks are formed resulting in the initiation of pitting corrosion. Once the growing stops, the pit will be repassivated. If pitting starts again the pits will grow at different places.

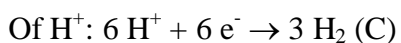
The intermetallic phases act as cathodes and reduce the oxygen concentration. At areas, where the oxide layer cracks, aluminium is immediately oxidized and the pit starts growing. At the same time, aluminium and chloride ions will form an intermediate complex ( $\text{AlCl}_4^-$ ).

Propagation of pitting is due to the following reactions:

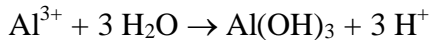
Oxidation at the anode:



Reduction at the cathode:



Due to the formation of  $\text{OH}^-$  and/ or the consumption of  $\text{H}^+$ , the pH of the environment will increase. Besides that the formation of  $\text{Al}^{3+}$  in the pit causes a diffusion of  $\text{Cl}^-$  ions in the cavity to neutralize the solution and form an intermediate complex of hydrochlorinated  $\text{AlCl}_4^-$ . The hydrolysis of these complexes will lead to a decrease of the pH ( $< 3$ ) according to the following equation:



This aggressive medium will accelerate the corrosion propagation.

Due to the high concentration of  $\text{Al}^{3+}$  at the pit bottom, the ions will diffuse outside of the cavity. As soon as they enter the alkaline environment at the pit opening they precipitate as  $\text{Al}(\text{OH})_3$  what can be seen as white voluminous and gelatinous pustules. The deposition of the corrosion products hinders to successive diffusion of ions inside the pits and vice versa and therefore slows down or even stops the corrosion propagation.

### II.5.3 Transgranular and intergranular corrosion

Within the bulk material corrosion can either spread randomly (transgranular corrosion) or follow a specific way along the grain boundaries (intergranular attack).

The first path has no preference in attacking the different metallurgical phases in the metal. Due to its name, trans-granular or trans-crystalline corrosion, it propagates within the grains.

The latter has its preferential way along the grain boundaries. The precipitation and/ or segregation of alloying elements along the grain boundaries results in electrochemical potential differences between noble alloying elements located in the boundaries and the solute-depleted aluminium matrix in the direct vicinity. Due to this difference the dissolution of the aluminium matrix along the grain boundaries is galvanically driven by the intermetallic precipitates. The second possibility is that the intermetallics are less noble than the surrounding aluminium matrix. In this case the particles will be dissolved. Figure II.5-2 shows the propagation of intergranular corrosion (IGC) of a cross-section of an AA4045/3003/4045 brazing sheet.

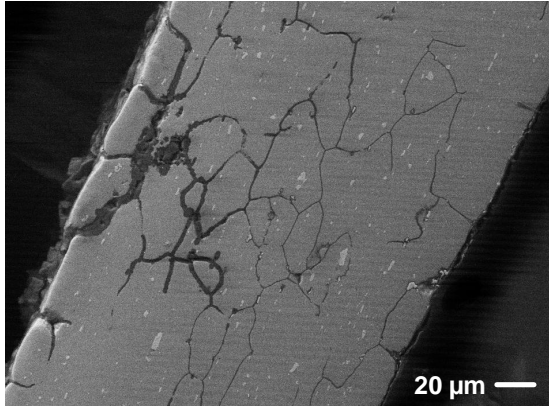


**Figure II.5-2:** Cross-section of an AAxxx/3xxx/4xxx brazing sheet. IGC propagates along the grain boundaries and perforates the material.

The corrosion path goes along the grain boundaries and creates fine cracks, which propagate through the entire brazing sheet and cause perforation of the material.

Different research groups investigated the influencing factors, making a material susceptible to pitting and/ or intergranular corrosion. In the beginning of the seventies Galvele and Micheli<sup>26</sup> investigated the correlation between anions such as chloride and intergranular attack of Al-Cu alloys. They found that intergranular attack is caused by a difference in pitting potentials between grain boundaries and grain bodies, but not to a difference of corrosion potentials. A lot of subsequent publications showed the influence of aging due to the effect on the pitting potential. Muller and Galvele<sup>27</sup> showed the correlation between IGC and the Co concentration in Al-Cu alloys. The pitting potential increased with increasing Cu content, having the maximum in the limited solubility of copper in aluminium. Buchheit, Moran and Stoner<sup>5</sup> distinguished local corrosion morphologies. They observed two different forms of pitting. Either pitting corrosion is caused through dissolution of the intermetallic phase, where they found a correlation between increasing subgrain boundary pitting due to increasing subgrain boundary participations. Or as a second form, pitting occurs locally by a galvanical attack, since the intermetallics show a cathodic behaviour and dissolve the adjacent aluminium matrix. These results were confirmed with other alloys.<sup>28</sup>

### II.5.4 Corrosion of aluminium brazing sheets: re-solidified clad

In the following sections the corrosion behaviour of aluminium brazing sheets is in the focus. Due to the assembly of different alloys within the brazing sheets, the discussion of the corrosion behaviour is divided in two parts: local attack in the clad material and in the core alloy.

The corrosion initiation in heat-exchangers occurs in the re-solidified clad, which is in contact with a (detrimental) environment. After one or two days the clad is penetrated by intergranular corrosion. A first explanation would be the presence of silicon, which has a nobler corrosion potential in comparison to aluminium. It acts as a cathode and accelerates the dissolution of  $\alpha$ -aluminium, adjacent to the silicon particles in the eutectic of the re-solidified clad material. A second reason is that the alloying elements as well as small intermetallics are present in a higher density in the  $\alpha$ -aluminium than in the primary aluminium grains, hence making the first one more susceptible to corrosion attack. However it has to be mentioned that silicon, although much nobler than aluminium, does not act as a strong cathode, but supports the corrosion initiation among aluminium.

Tierce et al.<sup>15</sup> investigated the corrosion behaviour of the different phases occurring in AA4343/3003/4343 brazing sheets. They confirmed the conclusion of Meijers et al.<sup>2</sup> that silicon is not responsible for the corrosion initiation. Due to electrochemical measurements and morphological investigations they observed that the initiation of corrosion occurs at the interphase  $\alpha$ -Al(Mn,Fe)Si particle/ aluminium matrix. First the particle started to dissolve, which could be observed in a re-deposition of the alloying elements such as Mn, Fe and Si around the particles. After that the reactivity changes and the dissolution of the aluminium matrix, located in the vicinity of the  $\alpha$ -Al(Mn,Fe)Si particle starts.

### II.5.5 Corrosion of aluminium brazing sheets: core material

Meijers et al.<sup>2</sup> investigated the corrosion behaviour of different aluminium brazing sheets. As an example of a commercially standard alloy they used AA3003. During exposure to the Salt Water Acetic Acid Test (SWAAT), they followed the corrosion propagation in the clad and in the core material. The corrosion mechanism in the clad material, as

discussed in the last section, differs from the one found in the core material. After the corrosion initiates in the re-solidified clad with intergranular corrosion (IGC) through the eutectic, the core material is galvanically by the diffusion zone. Exposing the material for several days to the salt spray test, morphological investigations showed hardly any attack of the  $\alpha$ -aluminium grains in the re-solidified clad. In comparison to that, in the eutectic of the re-solidified clad and in the core material, strong attack was observed. They explained this behaviour due to potential differences occurring between the clad, the diffusion zone and the core material. As discussed previously, the diffusion process of the alloying elements takes place during the brazing process, which has a crucial effect on the microstructure and hence on the corrosion behaviour of the material. They performed potential mapping of the different regions by means of Atomic Force Microscopy (AFM), to explain the corrosion behaviour. As a result, the clad material showed a higher potential than the core material (about 100 mV), while the diffusion zone showed a more noble potential than the clad material (about 75 mV). This result is in correlation with the investigations of the corrosion propagation during SWAAT exposure. After the corrosion initiated in the re-solidified clad, it continued in the core material, whereas the diffusion zone was hardly affected. The potential differences within the brazing sheet are summarized in [Figure II.5-3](#).

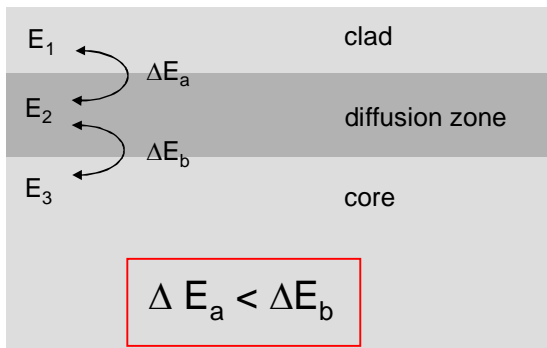


**Figure II.5-3:** Potential differences within the clad, the diffusion zone and the core material.

As the brazing process has a crucial effect on the corrosion behaviour, several publications appeared on rolled aluminium alloys, taken into consideration the effect of heat treatment on the microstructure.

Afseth et al.<sup>29,30,11</sup> published several reports on the influence of heat treatment on filiform corrosion of AA3005. They described a drastic degradation of corrosion resistance after exposing the metal to temperatures above 350°C. Due to morphological investigations in the as-received material they found a deformed near-surface area of approximately 1µm, formed during rolling. In that region several nucleation sites are formed, resulting in enhanced precipitation of second phase particles during annealing. This active near-surface layer showed preferential attack of corrosion, due to potential difference caused between intermetallics and matrix. Different pre-treatment steps like acid cleaning and/ or chromating did not show the desired improvement in corrosion resistance of heat treated material<sup>29</sup>. They also investigated the electrochemical behaviour of AA3005 after heat treatment and observed an increase of the anodic current density in comparison to the cold rolled, hard temper substrate. For this purpose they assumed a change in the protective oxide layer during heat treatment.<sup>30</sup> Gundersen et al.<sup>31</sup> observed an electrochemical activation of AA3102 in a chloride containing electrolyte after heat treatment. An explanation was found in the enrichment of lead, which is present as a trace element in the oxide-metal interface, destabilizing the native oxide layer. Additionally lead showed sacrificial properties, protecting the surface against pitting corrosion.

Sinyaviskii et al.<sup>32</sup> investigated the mechanism of intergranular corrosion (IGC) of AA3003 and AA3105 clad with AA4045. They investigated the initial semi-cold-hardened state after vacuum brazing. Initially AA3003 and AA3105 were not susceptible to IGC, which changed dramatically after heating. They concluded that there are two different forms of IGC. In low-alloy or pure aluminium mainly crystallographic IGC occurs, due to formation of active areas consisting of high angle boundaries during re-crystallization. To balance this effect they proposed an increase of the re-crystallization temperature. In medium or high-alloy materials another form called structure-decomposition was found. To reduce it, they suggested controlling the heat treatments to assure an even distribution of partly coherent phases and thus having less potential difference between grain boundaries and the matrix.

## II.6 Accelerated corrosion testing

### II.6.1 SWAAT

The SWAAT is a commonly used salt spray test for aluminium brazing sheets. It is often used as a quality control and therefore requested in industry. The test criteria of this salt spray test are the days till perforation of the material occurs. This is done by setting the heater core under a pressure of 10 bar. If a loss of pressure occurs the test is failed. Depending on the material the SWAAT duration can take a few days up to several weeks. Nowadays a SWAAT performance of minimum 20 days is requested. Although the test is generally accepted as a good simulation of service life, there are several drawbacks like its long duration and the low reproducibility. A deeper look at the SWAAT is done by Meijers et al.<sup>2</sup> They investigated the sample size as a possibility of the large scatter in the performance of aluminium brazing sheets found with the SWAAT. However there was no clear correlation between these factors, hence it is still not completely known what really causes such a large scatter in the results.

This was the driving force to find an alternative accelerated corrosion test to overcome the drawbacks resulting from SWAAT. Electrochemical techniques enable reliable and reproducible results for the investigation of the corrosion mechanism. Nevertheless it was necessary to perform some tests with common salt spray test to have the basic conditions for the corrosion behaviour. These results were compared with the results achieved with electrochemical tests.

### II.6.2 Electrochemical investigation

#### Open circuit potential (OCP)

The OCP gives an insight in the composition of an alloy, since the corrosion potential of a material is determined by the composition in solid solution (aluminium matrix) and by the second phase particles. Since the solid solution is mainly determining the properties of the microstructure, it is supposed to have a strong influence on the OCP. But also the second phase particles can be reflected in the potential transients. In AA4045/3003/4045 brazing sheets mainly the alloying elements (Si, Mn, Fe) and the heat treatments have an

influence on the microstructure and hence are reflected in the OCP. Mn has the strongest effect in shifting the OCP to more noble potentials. Since Mn is present in solid solution and in intermetallic phases it reduces the potential difference between the matrix and the particles and hence increases the corrosion resistance<sup>33</sup>. Si slightly increases the OCP due to an increase of the corrosion potential of the aluminium matrix. However it reduces the content of Mn in solid solution due to the formation of Si and Mn containing precipitates. Fe shifts the OCP in negative direction, because it shows mainly present in precipitates reducing the corrosion potential of the matrix.

#### Potentiodynamic polarization measurements

During potentiodynamic polarization scans the current density is measured as a function of the applied potential. The current density is calculated by the current flowing into the sample in correlation to the surface of the sample. Potentiodynamic polarization scans reveal information about the susceptibility to localized corrosion, concerning the

- number and position of breakdown potentials
- value of the current density during anodic and cathodic polarization
- evolution of the curve during re-passivation

Aluminium brazing sheets usually reveal two breakdown potentials. These potentials can be attributed to the initiation of pitting and intergranular corrosion, respectively.

### II.7 Anti-corrosion coating for aluminium: silica passivation layer

The following sections are dedicated to the chemistry of silica. In this work, silica is used to name the general description of  $(\text{SiO}_2)_n$  including all its amorphous, crystalline, hydrated or hydroxylated forms according to Iler et al.<sup>34</sup>

Silica is the most abundant component existing in the earth's crust, although its behaviour in solution as well as its interactions with a metal (surface) are still not very well known. It exists in different forms due to transformations caused by heat treatments. The most common crystalline form is quartz, the main component of sand, which ranges from huge crystals to amorphous looking powders. By changing the conditions additional structures can be produced:

Quartz (870°C)  $\leftrightarrow$  tridymite (1470°C)  $\leftrightarrow$  cristobalite (1700°C)  $\leftrightarrow$  vitreous

The soluble form of silica is the monomeric element consisting of  $\text{Si}(\text{OH})_4$ , which is called monosilicic or orthosilicic acid. The dissolution is based on the reaction:



Willey<sup>35</sup> assumed that the hydrated form is surrounded by 4 water molecules, each linked to one OH group,  $\text{Si}(\text{OH}:\text{OH}_2)_4$ .

In acid to neutral solutions of low concentrations ( $\text{Si} < 0,1 \text{ m}$ ) the only existing compound is orthosilicic acid in the tetrahydroxy form.<sup>36</sup> By increasing the pH, silica reacts with hydroxyl ions to form silicate ions in the following way<sup>37</sup>:



Below the solubility limit of amorphous silica ( $< 2\text{mmol/l}$ <sup>38</sup>), the main components in solution are the monomers  $\text{Si}(\text{OH})_4$ ,  $\text{SiO}(\text{OH})_3^-$  and  $\text{SiO}_2(\text{OH})_2^{2-}$ . The correlation between the specific compounds and the pH is given in [Figure II.7-1](#)<sup>39</sup>.

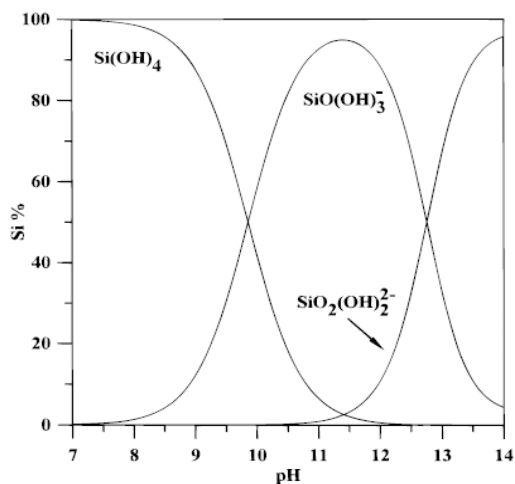


**Figure II.7-1:** Distribution of silicate species at 25°C as a function of pH in a 0,001 M Si solution.<sup>36</sup>

### II.7.1 Chemistry of silica

Different theories exist about the polymerization reaction occurring among silicid acid components. In 1863, first studies were performed in this field, but for a long time the debate was, whether  $\text{Si}(\text{OH})_4$  polymerized into the chains and these branched and cross-linked or if there is an evolution of discrete particles prior to the branch and cross-linking step. In 1940, Carmen<sup>40</sup> was the first one summing up the polymerization in the following three steps:

1. Polymerization of Si(OH)<sub>4</sub> to form particles
2. Growth of particles
3. Linking the particles, to build up a network of branched and linked silica.

The general reaction is given by

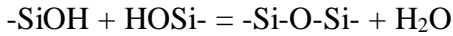
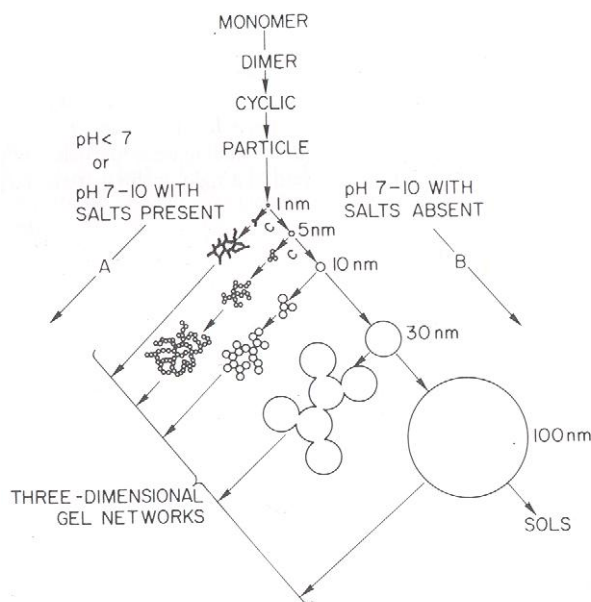


Figure II.7-2 shows a detailed illustration for the polymerization steps, introduced by Iler.<sup>34</sup>

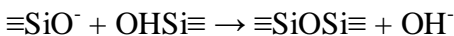


**Figure II.7-2:** Polymerization behaviour of silica. In basic solutions (B) the particles grow in size with decrease in numbers, in acid solution or in the presence of salts (A), particles aggregate into three-dimensional networks and form gels<sup>34</sup>.

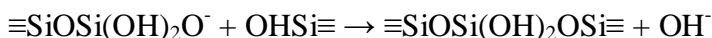
Polymerization at pH 2 to 7:

At pH 2 the polymerization is quite slow (in the range of hours), which makes it possible to clarify the different stages.

First there is a reaction between an ionized monomer and a non-ionized silanol group creating the dimer as follows



Since the dimer is a stronger acid than the monomer, the reaction will continue between the non-ionized silanol and dimers



The dimer becomes a linear tetramer either by reacting with its own ionized forms or with monomers. At this stage the ring closure is preferred, due to the high amount of involved silanol end groups and low concentration of monomers. Once the cyclic compounds are formed they react with the remaining monomers and dimers to increase the polymeric level. These polymers tend to condense through the silanol groups to form denser network and three-dimensional compounds. Since the particles bear no charge in the low pH range and the concentration of silica is low, the particles already begin in small sizes (2-3 nm) to agglomerate.

#### Polymerization above pH 7

The concentration of ionic compounds increases with increasing pH. Within minutes the monomers connect to form polymers, which are branched to create well linked particles. As opposite to lower pH values, the particles gain in size instead of colliding and aggregating, since they are charged and repel each other.

After a few minutes the average particles size is around 1-2 nm. A further increase of the particles depends on the distribution of particles size in solution, since the smaller particles are dissolved and again deposited on the larger silica particles. This relationship between increasing particle size and decreasing particle number is adapted to “Ostwald ripening”.

#### II.7.2 Water Soluble silica: sodium silicate

The soluble silicates made of alkali metal silicates are of great interest for industrial application.

Commercially the soluble silicates are prepared from the soluble silicate glasses. These are based on glass sand and sodium or potassium carbonate, according to the reaction:



Depending on the ratio between  $\text{SiO}_2$  and  $\text{Na}_2\text{O}$  different compounds like orthosilicate ( $\text{Na}_4\text{SiO}_4$ ), metasilicate ( $\text{Na}_2\text{SiO}_3$ ), disilicate ( $\text{Na}_2\text{Si}_2\text{O}_5$ ) or higher siliceous products of ( $\text{Na}_2\text{O} : 25 \text{SiO}_2$ ) exist. Probably the most commercially available one has a ratio of  $\text{Na}_2\text{O}$

: 3,3 SiO<sub>2</sub> with a solid SiO<sub>2</sub> content of around 27,0 %. Different industrial applications exist depending on the ratio between the silica and the alkali. Three major fields can be listed according to the SiO<sub>2</sub> : Na<sub>2</sub>O ratio:<sup>34</sup>

< 2.5 (particular meta- and orthosilicates): cleaners and detergents

2.5 – 3.8: adhesive, binder and deflocculant

3.3: production of precipitated silicas, sols and gels

### II.7.2.a Aqueous sodium silicate solutions: bonding and particle size

As mentioned previously, silica in solution is present as particles, due to the high affinity to polymerization. In sodium silicate solutions, the particle size is dependent on the ratio between silica and alkali metal. Investigations showed that by keeping the silica to alkali ratio constant, the particle size does not change, even while varying the concentration of the solution. For SiO<sub>2</sub> : Na<sub>2</sub>O ratios from 2:1 to 4:1, Iler et al.<sup>37</sup> observed that about 75% of the silica exists as particles of 1 to 2 nm diameter, increasing in size with increasing ratio. They assumed that a hydrated sodium layer is attached to the ionized surface of the particle. The size as well as the specific surface area depends on the amount of alkali. Furthermore they found an equilibrium between these colloidal particles and monomeric and oligomeric silicate ions (of up to eight silicon atoms). A schematic illustration of the connection of two ionized forms of silicates by hydrated sodium is presented in Figure II.7-3.

Hydroxyl ions transfer negative charge to the water layer that is bonded by hydrogen to silanol groups (A, B). Hydrated sodium ions are adsorbed at the negative charged site forming a neutral complex (C). The collision with an uncharged area of a second particle permits sodium to act as bridging between oxygen of the silanol and surface bonded water (D).

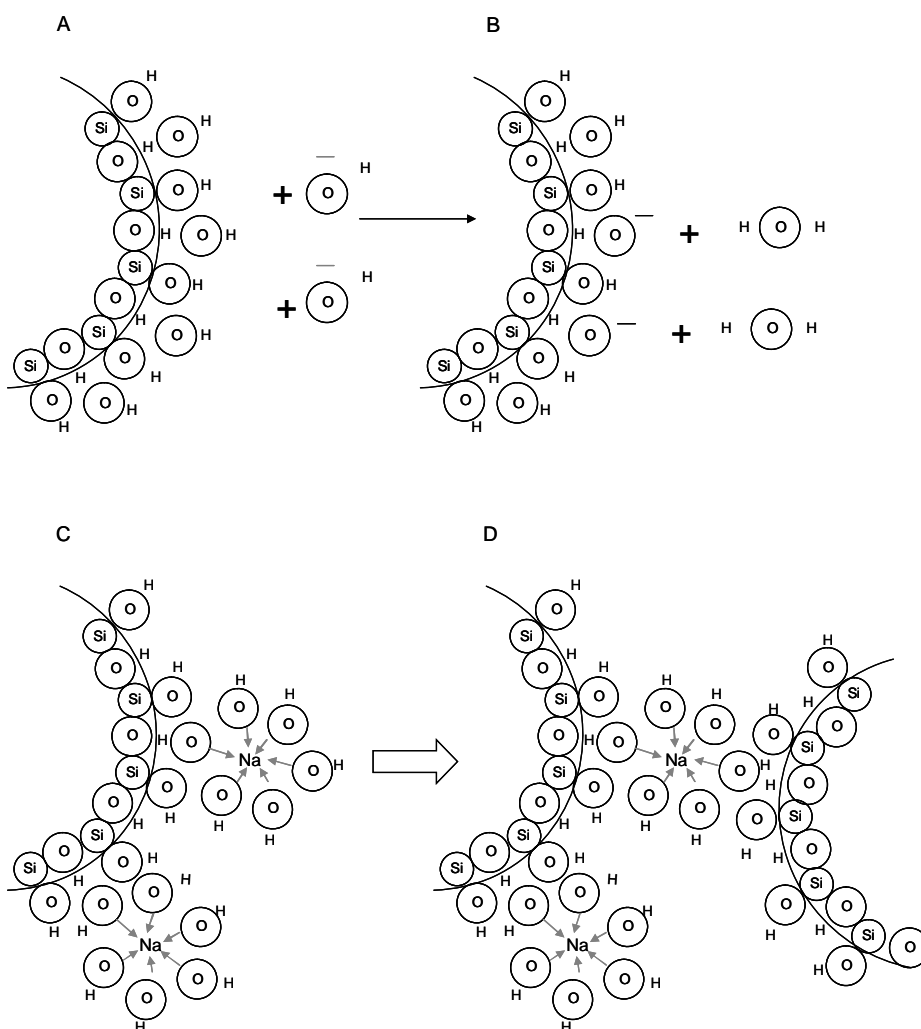


**Figure II.7-3:** Bonding between silica particles through coordination by metal cations.

Different authors published their results in clarifying the siloxane bonds in aqueous silicate solutions. However comparing the information about the assignment of vibrational bands to specific molecular structures, less information was found. Gout et al.<sup>36</sup> published a Raman spectroscopic study on strongly diluted aqueous silica-bearing solutions, suggesting the  $\text{SiO}(\text{OH})_3^-$  monomer as the predominant species in basic solutions. By increasing the concentration they proposed the formation of polymerized species. Bass et al.<sup>41</sup> published their results on  $^{29}\text{Si}$  NMR and IR. By increasing the  $\text{SiO}_2 : \text{Na}_2\text{O}$  ratio the amount of polymeric species in solution increased. However in alkaline and diluted solutions mainly monomer, dimer and cyclic trimer silicate compounds exist.

In the year 2007 Halasz et al.<sup>42</sup> suggested in contradiction to the common belief that the Si-O vibrations are independent of polymer structures but on the dissociation level. By IR and Raman spectroscopy they observed that in 0.2-3.0 molL<sup>-1</sup> aqueous metasilicate solutions the silicates mainly exist as monomers, Na<sub>2</sub>H<sub>2</sub>SiO<sub>3</sub>, dissociated about 30% - 80%. Yang et al. reported in detail about the distribution of silica species in correlation to pH and concentration. Polymers and colloid silica was found at low pH and monomers at higher pH observed by a shift of the vibration band to higher frequency. Besides they observed a dependency of the concentration. Dimers, trimers, oligomers and higher aggregates are formed by condensation reactions of the monomers in higher concentrations.

### II.7.2.b Aqueous sodium silicate solutions: deposition on a solid surface

The mechanism of layer formation from monomeric silica species is entirely different to the layer formation from colloidal particles. The layer formed by monomeric silica looks like an impermeable glassy film, whereas colloidal particles build up a porous, white film.

Monomeric silica can be deposited out of a supersaturated solution in the following ways:<sup>34</sup>

1. As a deposit on a solid surface: if a solid surface such as a metal surface bears OH groups, Si(OH)<sub>4</sub> can react in a condensation step and build M-O-Si bonding connection (M = metal).
2. As colloidal particles: in the absence of a receptive solid surface and a concentration of more than 200-300 ppm of Si(OH)<sub>4</sub> in solution, polymerisation occurs. In the first step cyclic tetramers are created, which condense to connect with each other and build up a three-dimensional colloidal particle.

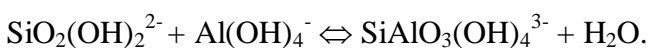
Colloidal silica can be deposited on a solid surface according to different processes. By immersion of a surface in a dilute sol and drying for several times a hard film can be built up. Once the colloidal particles dried on the surface they are irreversible attached to the substrate. When there are similar conditions (pH and salt concentration) in a dilute sol, usually causing coagulation or precipitation, deposition of colloidal silica on a solid surface can occur. Deposition occurs as soon as collision between the colloids and the

solid surface happens. The concentration of colloids should be low, suppressing the coagulation and gelling of the colloids in solution.

Usually for the deposition of colloidal particles a coagulation compound is necessary. This can be a polyvalent as well as a monovalent metal ion. Since in a neutral or alkaline silica solution the silica particles bear a negative charge, they repel each other and the collision rate is very low. To overcome that effect, the metal ions adsorb on the silica surface and therefore increase the collision process.

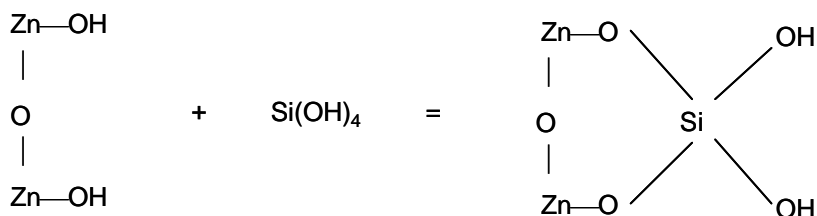
Hingston and Raupach<sup>43</sup> studied the reaction between monosilicic acid  $\text{Si}(\text{OH})_4$  and crystalline aluminiumhydroxide. They found that several layers of silicic acid can be built up on the metal surface. The first layer has a fast reaction time, whereas the additional layers grow slower. In addition, they assumed that the silicate layer is adsorbed via silicic acid rather than via silicate ions.

Gout et al.<sup>36</sup> suggested the formation of a single Al-Si dimer in strongly basic aqueous solutions (pH ~ 14) containing Al and Si. They reported the formation of a complex through:



At lower pH (~ 12.5) they observed a change of band intensities due to the formation of more polymerized Al-Si complexes.

Kumaraguru et al.<sup>44</sup> proposed a deposition of sodium silicate (3.22 weight ratio of  $\text{Na}_2\text{O} : \text{SiO}_2$ ) on galvanized steel in the following way:



They observed the reaction between the monomeric  $\text{Si}(\text{OH})_4$  and  $\text{Zn}(\text{OH})_4^{2-}$  from the substrate to form a thin zinc disilicate layer by an adsorption process.

### II.7.2.c Aqueous sodium silicate solutions: structure of the silica coating

For chemical analysis of different silica compounds, X-ray photoelectron spectroscopy (XPS) has been frequently used. By calculation of the ratios between Si and O it is possible to attribute the silica structure to specific modifications.<sup>45,46,47,48</sup>

Hahn et al.<sup>47</sup> investigated silica coating on galvanized steel. They observed a progressive increase of the Si 2p binding energy as the polymerisation from monomers to polymerised silica increases. Furthermore Kumaraguru<sup>44</sup> investigated the structure of the silicate layer deposited on steel. They supposed a disilicate layer in the interface substrate/coating. The continuation of the layer formation was given by condensation reactions between silanol groups of Si(OH)<sub>4</sub> to form a SiO<sub>2</sub> layer.

However no information about the deposition of silica on aluminium substrates was found.

### II.7.2.d Aqueous sodium silicate solutions: barrier properties of the silica coating

The use of sodium silicate for the protection of iron, steel, zinc, galvanized steel and brass is quite common and has been reported several times in literature.<sup>44,49,50</sup>

Independent on the application of the silica layer, an increase of the corrosion resistance was observed. However no literature was found concerning silicates on aluminium substrates. Furthermore no detailed information about the protection mechanism was found.

---

## CHAPTER THREE

---

# EXPERIMENTAL

**Abstract**

*This chapter gives a brief overview of the used conditions for the experimental approach. It includes the specifications about the performed accelerated corrosion tests (SWAAT and electrochemical techniques) and the conditions for the analysis methods. Besides the standard conditions for the application of the silica coating on the aluminium substrates are presented.*

## III. Experimental

### III.1 Introduction

This chapter presents an overview of the used techniques, materials and products. Since the experiments described in following chapters required various pre-treatments, only the common experimental conditions are described in this chapter. The specific experimental details will be given in the respective section. The (pre)-treatment for both materials (pure aluminium and its alloys) was performed under the same conditions.

### III.2 Substrate

Since the thesis is focused on different applications, different aluminium substrates were used. Part one (Chapter IV) was focused on the characterization of aluminium brazing sheets. For this purpose a commercially used three-layer aluminium system was investigated, consisting of an aluminium-manganese core material (AA3003), clad on both sides with an aluminium-silicon alloy (AA4045).

In part two (Chapter V) the deposition conditions of silica passivation on aluminium substrates were investigated. To overcome the disruptive influence of the silicon containing alloy (AA4045) on structural investigations, pure aluminium was used. Finally, in part three (Chapter VI) the corrosion performance of the passivation layer was tested. During this part, both materials pure aluminium and aluminium brazing sheets (AA4045/3003/4045) have been used, depending on the respective measurement. In order to investigate the effect of the deposition conditions on the barrier properties of the silicate passivation layer, pure aluminium has been used. In addition to that the corrosion performance of the silica passivation layer was studied on aluminium brazing sheets (AA4045/3003/4045).

Compositions of the materials are given in Table III-1.

Table III-1: Alloy composition (in wt%)<sup>51</sup>

Alloy	Al	Si	Mn	Fe	Cu	Zn	Ti	Mg
AA3003	>96	0,6	≤1,5	0,7	≤0,2	0,1	-	-
AA4045	>87	9-11	0,05	0,8	0,3	0,1	0,2	0,05
Al99,99%	>99,99	-	-	-	-	-	-	-

### III.3 Pre-treatment of the samples

The pre-treatment can be divided in three parts: the first part is degreasing, the second step consists of alkaline cleaning and the third is the deposition of the silica coating. The degreasing includes ultrasonic cleaning with acetone and ethanol for 5 minutes each. The alkaline cleaning was performed with Ridoline 34 (7,5 g/l) for 3 minutes at 50°C. The product was diluted with tap water. Since it is a tenside free product, Ridolsol C27 was added in a concentration of 10% in correlation to the mass of Ridoline 34. The etching rate of the cleaner is around 40 g/m<sup>2</sup> h. The surfactant and the alkaline cleaner were provided by Henkel AG & Co KGaA. After the alkaline cleaning the samples were rinsed in tap and distilled water.

### III.4 Mechanical transformation of the aluminium substrates

In order to investigate the effect of mechanical transformations on AA4045/3003/4045 brazing sheets, an Erichsen impression was performed. For this purpose the plane substrates were deep-drawn with a depth of 5 mm. A schematic illustration of the transformation process is given in Figure III.4-1 (A, B).

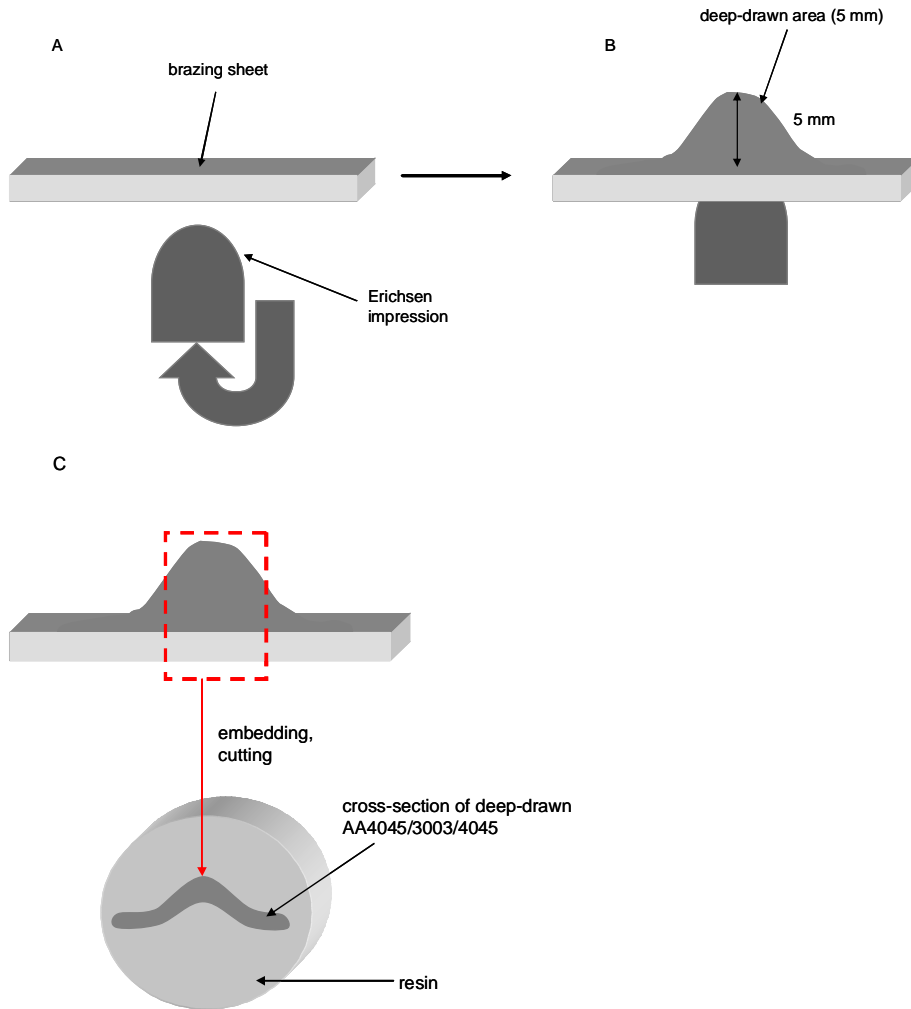


**Figure III.4-1:** Mechanical transformation by deep-drawing (A, B) and embedding in resin (C, D).

For the morphological investigations, cross-sections of the samples were prepared by cold embedding in resin (Figure III.4-1 C). During this procedure special care was taken not to twist the deep-drawn area.

### III.5 Deposition of the passivation layer

#### III.5.1 Sodium silicate solution

The sodium silicate solution (trade name Wasserglas 37/40) was obtained by Cognis GmbH Düsseldorf, Germany. The ratio of sodium oxide to silica is given by  $\text{Na}_2\text{O} : 3.35 \text{ SiO}_2$ . The specifications provided by the supplier are listed in Table III-2.

**Table III-2:** Specifications for sodium water glass 37/40

Wt. Ratio:	SiO <sub>2</sub>	Na <sub>2</sub> O	Density	Viscosity
SiO <sub>2</sub> :Na <sub>2</sub> O	(%)	(%)	(g/cm <sup>3</sup> )	mPa.s
3,35	26,6-27	7,8-8,2	1,345-1,355	50-100

#### III.5.2 Diluting sodium silicate solution

Sodium silicate solution (37/40) was diluted with distilled water to prepare the solutions used for the deposition of the passivation layer on aluminium panels. The concentration of the sodium silicate solution was calculated taking into account the solid content of SiO<sub>2</sub> dissolved in sodium silicate solution.

Different bath concentrations were used in order to investigate their influence on the deposition of the passivation layer. Therefore the commercially water glass solution was diluted to 0.2 m, 1.1 m, 2.0 m and 3.0 m SiO<sub>2</sub>.

#### III.5.3 Silicate film deposition

After diluting the product with distilled water to a concentration of 1.1 m SiO<sub>2</sub>, the solution was heated to 60°C. The degreased and alkaline cleaned aluminium samples were immersed for 60 sec in the aqueous silicate solution. By stirring the solution, an equal contact of the aluminium substrate during immersion was ensured. After removing the excess liquid by dripping samples were. The curing of the coating was performed for 30 min at 150°C in an oven at atmospheric pressure. These conditions were associated to

standard conditions. A schematic illustration of the deposition process is given in Figure III.5-1.

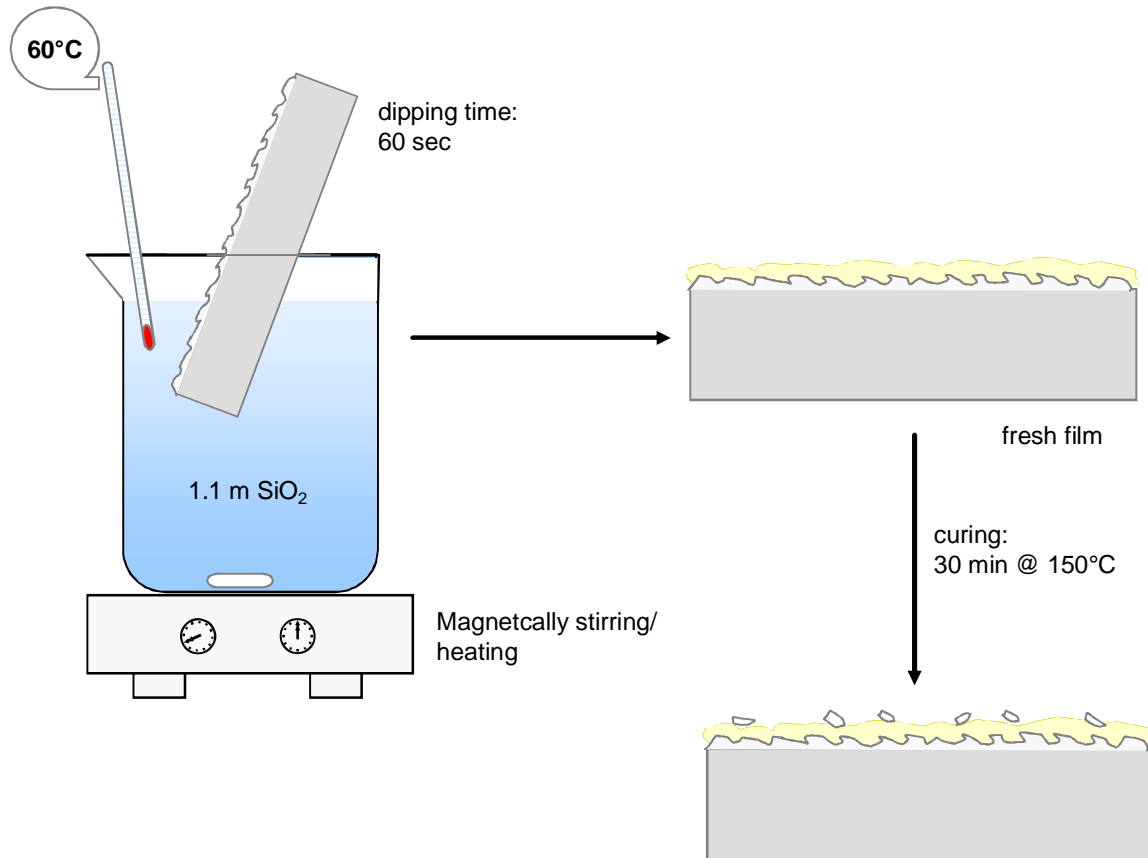


**Figure III.5-1:** Deposition of sodium silicate on an aluminium substrate

As mentioned before, various bath concentrations, curing times, curing temperatures and dipping times were used. The different pre-treatment conditions are presented in Table III-3.

**Table III-3:** Parameters of the used settings for the deposition of the passivation layer.

Deposition conditions	Conditions
Bath concentration (m SiO <sub>2</sub> )	0.2, 1.1, 2.0, 3.0
Dipping time (sec)	10, 60, 600
Curing temperatur (°C)	0, 50, 100, 150, 250
Curing time (min)	0, 1, 5, 30, 60

To simplify the various pre-treatment conditions a standard procedure was set. The experimental conditions are presented in Table III-4.

**Table III-4:** Conditions used for the standard pre-treatment

Bath concentration (m SiO <sub>2</sub> )	Dipping time (sec)	Curing temperature (°C)	Curing time (min)
1.1	60	150	30

Based on this standard, the settings for the various pre-treatment conditions were prepared. For this purpose one parameter was adopted to the respective conditions listed in Table III-3 and the remaining parameters were used in correspondence to the standards.

### III.6 Accelerated corrosion testing

The corrosion performance on aluminium and its alloy was studied by accelerated corrosion testing. For this purpose the samples were exposed to the salt water acetic acid test (SWAAT). Moreover potentiodynamic and potentiostatic polarization was performed. The conditions for the salt spray test and the electrochemical techniques will be described during the following sections.

#### III.6.1 Sea Water Acetic Acid Test (SWAAT)

The SWAAT solution consists of 42 g/l sodium chloride with a pH between 2.8 and 3.0. The pH is adjusted with acetic acid (usually 10 ml/l). Normally the temperature in the test chamber averages 49°C. The test propagates through recurring cycles, lasting 120 minutes each. During this time, the specimens are sprayed for 30 minutes and subsequently evaporated for 90 minutes (above 98% humidity in the chamber) with SWAAT solution. Originally a salt spray test with these criteria is described by ASTM G43 and then changed to ASTM G85<sup>52</sup>.

The samples, with a size of (5x10) cm<sup>2</sup>, are placed in the test chamber and located in a sample holder with an angle of 75°, to ensure reproducible standards. Every 24 hours an

embedded and polished cross-section of a specimen was investigated by SEM to record the corrosion propagation. Since the specimens are differently stressed by the SWAAT solution (the bottom part of the sample has less contact with the acidic solution during the spraying part of the test cycle) the upper part is only considered during the analysis. Due to the very aggressive conditions of the test solution on the samples, one day in the test chamber simulates around one year of service life.

### III.6.2 Electrochemical techniques

For the realisation of the electrochemical tests a three electrode arrangement was used, consisting of a platinum grid as counter electrode, silver/ silver chloride electrode as reference and the aluminium sample as the working electrode. The measurements were done with a PGSTAT 100 from Eco Chemie Netherlands and controlled via the GPES software. During the measurements the electrolyte was stirred to avoid failure in the conductivity due to blisters on the sample surface. All electrochemical measurements were performed in SWAAT solution, containing 4.2 % NaCl and a pH of 2.8, adjusted with acetic acid. A schematic of the set-up is shown in [Figure III.6-1](#).

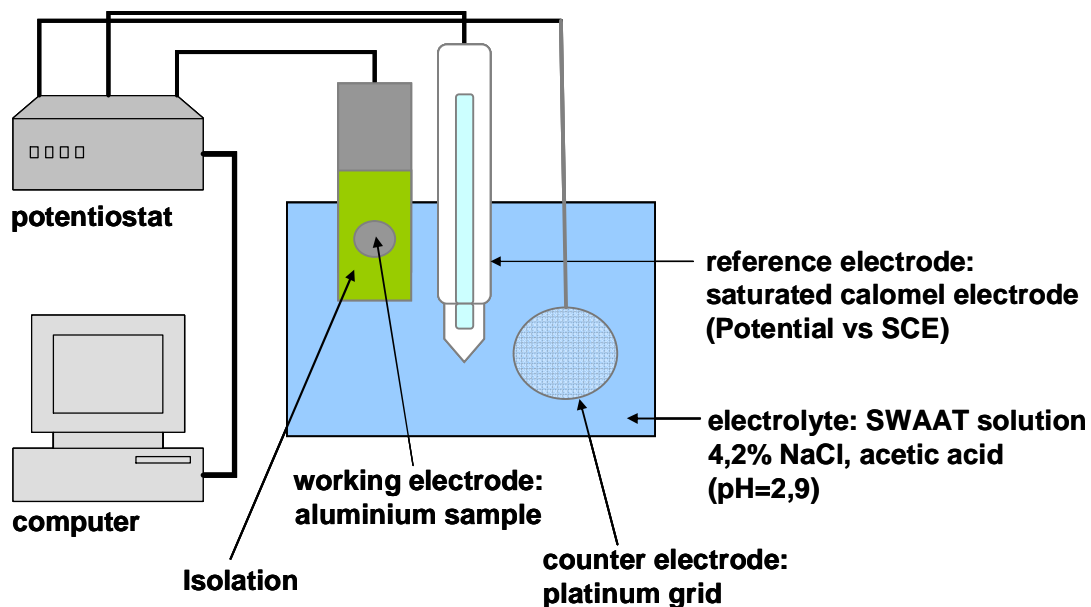


**Figure III.6-1:** Electrochemical set-up used for the OCP as well as for the polarization measurements.

#### Open-Circuit Potential (OCP) measurements:

The potential transient was recorded for 30 minutes with one data point per second. To ensure a defined surface, the samples were isolated with a tape that was not affected by the electrolyte.

#### Potentiodynamic polarization:

The current transient was recorded with a scan rate of 0.2 mV/sec. Prior to the polarization scans the OCP was measured for 30 min to ensure stable conditions. The polarization in the forward scan was performed to 0.40 V vs. OCP and in the negative direction to -0.35 V. To ensure a defined surface, the samples were isolated with a tape that was not affected by the electrolyte. The details of the experimental conditions are given in Chapter IV.

#### Potentiostatic polarization:

The current transient was recorded for one hour at a constant potential with one data point each second. To ensure a defined surface, the samples were isolated with a tape that was not affected by the electrolyte.

### III.7 Analytical methods

The following section describes the analytical techniques used for the investigations of the bare aluminium substrates and for the substrates immersed in aqueous sodium silicate solution. The methods can be divided in analyzing techniques, requiring a special atmosphere or sample preparation (SEM and XPS) and the methods performed under standard conditions (optical microscopy and Raman spectroscopy).

#### III.7.1 Scanning Electron Microscopy (SEM)

For this work a SEM/EDX from JOEL (JSM-6400) was used to characterize the surface morphology of the bare material during corrosion propagation.

To investigate the morphology of the silicate passivation layer a JOEL JSM – 7000 FE-SEM technique with high spatial resolution was used. In order to investigate the

topography of the surface, an accelerating voltage of 15 keV was used. To overcome the charging effects, caused by the non-conductive properties of the silicate passivation layer, the samples have been covered with a 1.5 nm Pt/Pd layer, applied by a Cressington MTM-20 thickness controller. On the FE-SEM images the thickness of the silicate layer was measured using a Joel Smile View software.

EDX (Energy Dispersive X-ray Analysis) was used to identify the elements on the surface and at the cross-sections. The depth of the electron beam is around 1  $\mu\text{m}$ . For cross-sectional imaging purposes, the silicate coated samples were bent over a razor blade after immersion in liquid nitrogen, to ensure a sharp cut of the film.

### III.7.2 X-ray Photoelectron Spectroscopy (XPS)

The XPS measurements were carried out with a PHI 1600 photoelectron spectrometer. The spectrometer is equipped with a dual-anode X-Ray source (Mg  $K\alpha$  and Al  $K\alpha$ ), an X-Ray source with an Al anode combined with a monochromator. The hemispherical electron analyser (HMA) contains a maximal resolution of 0.8 eV.

For performing the depth profiles an Ar ion gun (beam spot: of  $(3\times 3)\text{mm}^2$ ) was used for sputtering the surface and an electron gun (neutraliser) to compensate the charging effects. All the spectra were analysed using the PHI Multipak (version 5.0 and 6.1) software. The measurements were done using a primary accelerating voltage of 5 keV. The analysis area used was  $(30\times 40)\mu\text{m}^2$ . The survey scans were done using a step size of 0.5 eV doing the cycle three times. The depth profiles were performed with 4 kV.

### III.7.3 Raman Spectroscopy

The Raman measurements were performed using a Dilor XY Raman spectrometer. The set-up is equipped with a water cooled Coherent Innova 70/C Argon/Krypton mixed gas laser which emits visible green light at 514.5nm. The laser pointer was set either at 50 and 100mW dependent on the low intensity signal of the amorphous silica layers. Furthermore the technique is connected to an optical microscope from the Olympus BH2 series associated to a manual XYZ stage and a long focal 50x objective.

The measurements range was set between 300 and 1400  $\text{cm}^{-1}$  with an acquisition time of 300 sec.

---

## CHAPTER FOUR

---

# ACCELERATED CORROSION TESTING

**Abstract**

*In this chapter the morphological and the electrochemical characterization of AA4045/3003/4045 brazing sheets, used in the automotive industry, were performed. Furthermore the effect of the brazing temperature and the mechanical transformation on the material properties of the brazing sheets were investigated. For this purpose the following process conditions were studied:*

- standard brazing temperature: 590 C*
- increased brazing temperature: 615°C*
- without brazing (pre-brazed)*
- after mechanical transformation by an Erichsen impression*

*Salt spray testing (SWAAT) and detailed electrochemical tests were performed to gain information of the corrosion behaviour. The focus was on the appearance of localized attack and the initiation and propagation of corrosion within the brazing sheets. Measuring the open circuit potential (OCP) enables conclusions about the composition of the solid solution (aluminium matrix). Besides, potentiodynamic polarization curves were performed to study the susceptibility of the material to localized corrosion and to attribute breakdown potentials to specific forms of localized attack. By applying one potential above the breakdown potential (potentiostatic polarization) it is possible to induce the respective forms of localized attack. In order to correlate the microstructure with the electrochemical behaviour, the morphology and the composition of the samples were investigated before and after the accelerated corrosion testing by scanning electron microscopy equipped with energy dispersive spectroscopy (SEM/EDS).*

*The conventional salt spray test and the electrochemical techniques revealed the same corrosion propagation of the brazing sheets, initiated by potential differences within the multilayer system, caused by diffusion of the alloying elements during the brazing cycle. Increasing the brazing temperature resulted in a decrease of the susceptibility to localized attack. The mechanical transformation showed no significant effect on the corrosion behaviour.*

## IV. Accelerated corrosion testing

### IV.1 Introduction

In this chapter the morphology and the electrochemical behaviour of aluminium brazing sheets used as heater cores in automotive industry are investigated. Besides, the effect of the brazing temperature and mechanical transformation on the corrosion performance is discussed. The aim was to correlate the corrosion behaviour to the microstructure. The following processing conditions of AA4045/3003/4045 brazing sheets were investigated:

- as-received material (standard conditions: brazed at 590°C)
- pre-brazed material (without brazing)
- material brazed at 615 °C (increased brazing temperature)
- deep-drawn as received material (Erichsen impression)

To understand the corrosion behaviour it is necessary to investigate the composition of the material, since the electrochemical properties are determined by the microstructure. During the brazing process, due to the high temperatures, diffusion of the alloying elements occurs, resulting in the formation of potential differences caused by depletion of the alloying elements from solid solution (aluminium matrix) and precipitation in second phase particles.<sup>3,18</sup> This change in the chemical composition of the material is measured by SEM/EDS. The results were used for the discussion of the corrosion behaviour found during accelerated corrosion testing. For this work the salt water acetic acid test (SWAAT) was used, which is a common accelerated corrosion test for aluminium in industry.<sup>1</sup> However the SWAAT shows several drawbacks such as a long duration and low reproducibility and hence it is not a proper method to study the corrosion behaviour in detail. To overcome these drawbacks the corrosion performance was also tested by different electrochemical techniques. Recording the OCP gives information about the composition of intermetallic phases and particularly about the composition in the solid solution (matrix), since this phase is the dominant area in the microstructure of the alloy.<sup>11</sup> Besides, potentiodynamic polarization curves were performed to gain information about the susceptibility to localized corrosion of the alloy and to attribute the breakdown potentials to specific forms of localized attack.<sup>4</sup>

Furthermore the correlation between the propagation during SWAAT and by electrochemical techniques was investigated.

## IV.2 Characterization of the material

In order to investigate the effect of the brazing process, the microstructure of the samples was investigated before and after the heat treatment by SEM analysis in combination with EDS. Furthermore the mechanical transformation was simulated with an Erichsen impression and analysed by SEM imaging.

Figure IV.2-1 shows the top view (A) and the cross-section (B) of the pre-brazed material. The pre-brazed material reveals no significant particles or precipitates and the rolling lines, wavelike cavities in the x-direction due to the roll-bonded cladding, can be clearly seen. In the clad area of the cross-section, dark spots can be observed. In the core area several particles of various shape and size can be observed. The EDS results are presented in Table IV-1. On the surface mainly Al and Si was detected (area 1 and area 2). The high concentration of Si and Al alternate since the Si phases are evenly distributed in the aluminium matrix. This can be seen in the cross-sections in the dark areas in the clad material. The EDX measurements mainly reveal Si in the dark spots (particle 2), due to the high concentration of free Si. In contradiction to that, particle 1 in the core material contains mainly of Al, Fe and Mn. Area 3 reflects the solid solution composition of the core material (AA3003). At that area mainly Al, Si and Mn was detected. The carbon intensity is mainly due to the embedding material and impurities and hence will not be considered here.

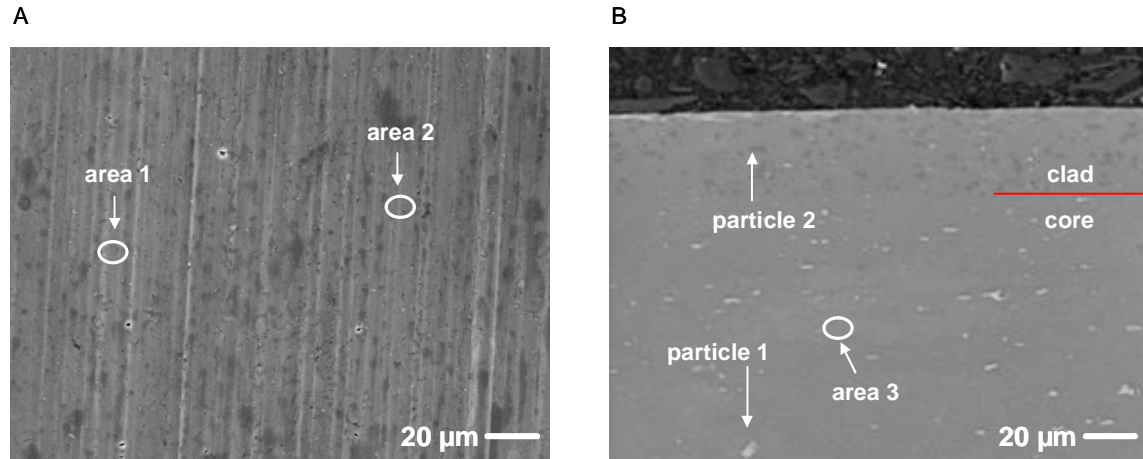


**Figure IV.2-1:** Top view (A) and cross-section (B) of AA4045/3003/4045 before the brazing process

**Table IV-1:** Atomic concentrations measured in AA4045/3003/4045 brazing sheets before brazing.

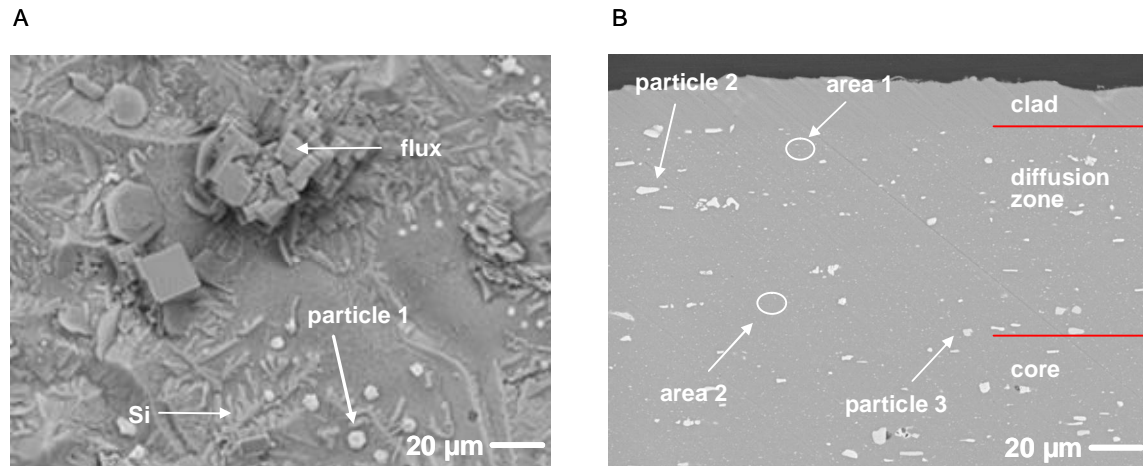
Point/ Particle	Al (at%)	Si (at%)	Fe (at%)	Mn (at%)	O (at%)	Cu (at%)	C (at%)
Area 1	66.7	10.3	-	-	-	-	15.3
Area 2	36.8	50.4	-	-	-	-	12.6
Area 3	89.6	0.1	-	0.4	-	-	9.6
Particle 1	78.9	-	4.1	2.7	2.1	0.2	11.0
Particle 2	19.6	64.3	-	-	-	-	16.0

Figure IV.2-2 shows the surface (A) and the cross-section (B) after the brazing process. The surface is very rough and inhomogeneous and reveals various precipitates and particles. Due to EDX analysis, shown in Table IV-2, the following phases can be attributed:

- Flux: contains mainly Al and K and is used during the brazing process to dissolve the native oxide layer to ensure proper joining.
- Si needles: mainly present in the Al-Si eutectic.
- Al-Fe-Mn-Si blocklike precipitates (particle 1):  $\alpha$ -Al(Fe,Mn)Si

A closer look at the cross-section reveals different areas within the material. In the residual cladding no significant particles can be seen. EDX analysis (area 1) shows mainly Al and Si. In the transition between the clad and the core material a high density of small particles, evenly distributed, can be observed. The EDS results in this area (area

2) mainly show Al, Si and low concentrations of Mn, Fe and Cu. The particles found near the clad material (particle 2) contain mainly Al, Fe, Mn and Si. The particles found further away from the clad material (particle 3) show the same components but less amounts of silicon.



**Figure IV.2-2:** Top view (A) and cross-section (B) of AA4045/3003/4045 brazing sheet after brazing.

**Table IV-2:** Atomic concentrations measured in AA4045/3003/4045 brazing sheets after brazing.

Area/ Particle	Al (at%)	Si (at%)	Fe (at%)	Mn (at%)	O (at%)	Cu (at%)	C (at%)	K (at%)
Area 1	57.0	25.13	0.3	0.2	3.2	0.1	13.5	-
Area 2	93.3	0.5	0.1	0.1	1.5	0.1	4.3	-
Particle 1	46.9	6.9	6.2	7.6	4.6	-	2.2	-
Particle 2	70.0	8.69	4.1	7.4	3.4	0.5	16.0	-
Particle 3	73.9	5.6	2.6	8.2	-	0.2	9.5	-
Flux	39.5						21.6	38.8

Considering the results gained by SEM/EDS of the microstructure before and after the brazing process, a change in size, shape and composition of the particles within the brazing sheets is observed.

Prior to the heat treatment the core and clad material is clearly separated. In the clad material Si is present due to the eutectic solidification of the filler alloy (Figure IV.2-2).

In the core alloy the particles contain Al, Fe and Mn. According to Alexander and Greer, these particles are attributed to  $\text{Al}_6(\text{Mn,Fe})^8$ .

The effect of the brazing process on the different elements is concluded as follows:

### Si

diffuses from the clad to the core material. This is observed in the post-brazed microstructure by three properties:

- 1) Below the clad material an area with a slightly higher intensity of precipitates is observed, revealing high concentrations of Si. This effect is often reported in the literature.<sup>1,2,3</sup> During the heat treatment, Si diffuses from the clad to the core material and initiates the formation of small Si-Mn precipitates which is seen as a band of dense precipitates in the diffusion zone.
- 2) In the post-brazed material the  $\text{Al}_6(\text{Mn,Fe})$  precipitates disappeared in the area below the clad material and a new phase containing Al-Fe-Mn-Si appeared. Alexander and Greer<sup>8</sup> reported about this transformation in AA3003 during homogenisation. They observed a reaction between  $\text{Al}_6(\text{Mn,Fe})$  and dissolved Si from the surrounding matrix resulting in the formation of cubic  $\alpha\text{-Al(Fe,Mn,)}\text{Si}$  precipitates and Al.
- 3) Furthermore the  $[\text{Si}]_{\text{ss}}$  content in the area below the clad increases since not all silicon from the diffusion process precipitates.

### Mn

This element is mainly present in the solid solution in the pre-brazed material. Due to the influence of Si, a depletion of Mn occurs since it is precipitated as Si-Mn. This is observed in the reduction of  $[\text{Mn}]_{\text{ss}}$  in the diffusion zone compared to the core material. Besides, Mn is diffusing from the core to the clad material, since it is detected in that area in the post-brazed material. This phenomenon is an additional reason for the very low content of  $[\text{Mn}]_{\text{ss}}$  in the diffusion zone.

### Cu

The effect of the brazing process on copper is not very strong, since the concentration of copper in the alloys is very low. However it is seen that this element diffuses from the core to the clad material, since it is detected in the diffusion zone and the clad material in the post-brazed material.

Fe

This element shows a similar behaviour as copper. During the heat treatment it diffuses from the core to the clad material. The highest concentrations are found in the different particles.

Figure IV.2-3 presents an illustration of the significant effects on the microstructure during the brazing process.

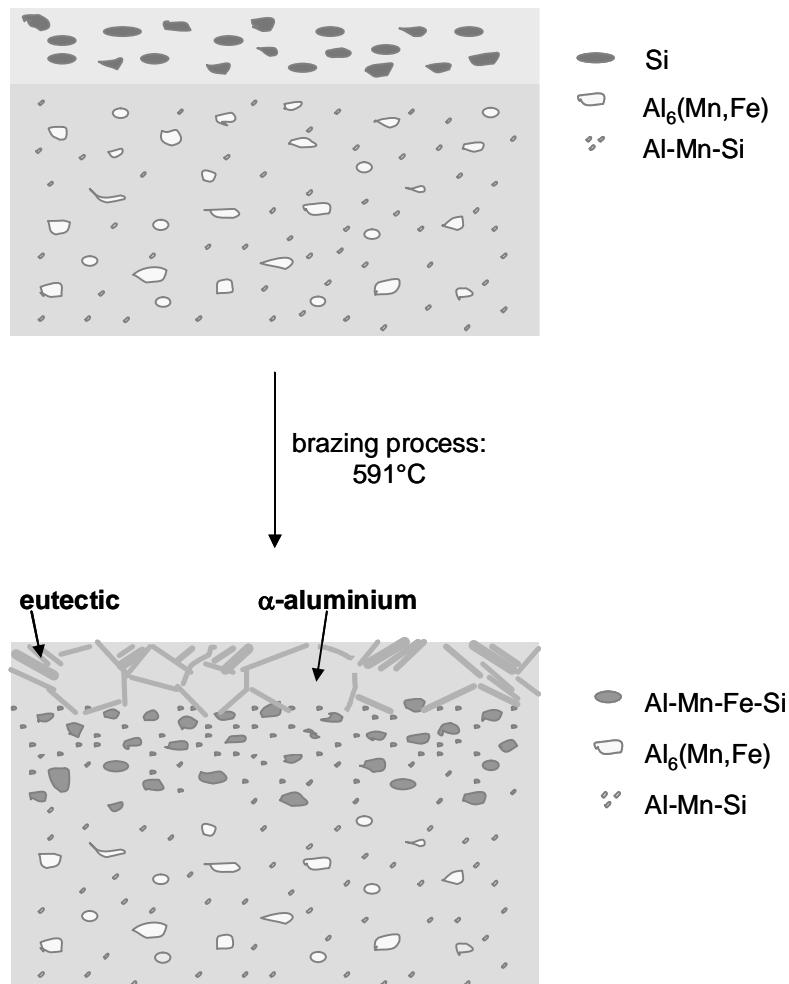


**Figure IV.2-3:** Schematic illustration of the effect of the brazing process on the microstructure.

#### IV.2.1 Microstructure after mechanical transformation

Figure IV.2-4 presents the micrographs of the cross-sections of AA4045/3003/4045 brazing sheets before (A) and after (B) an Erichsen impression.

The morphology after the deep-drawing process showed no significant changes. Except, the grain shape is adapted to the mechanical transformation, since the grains are slightly elongated. The composition of the particles and in solid solution measured by means of EDX (not shown here) is not changing during the transformation process.

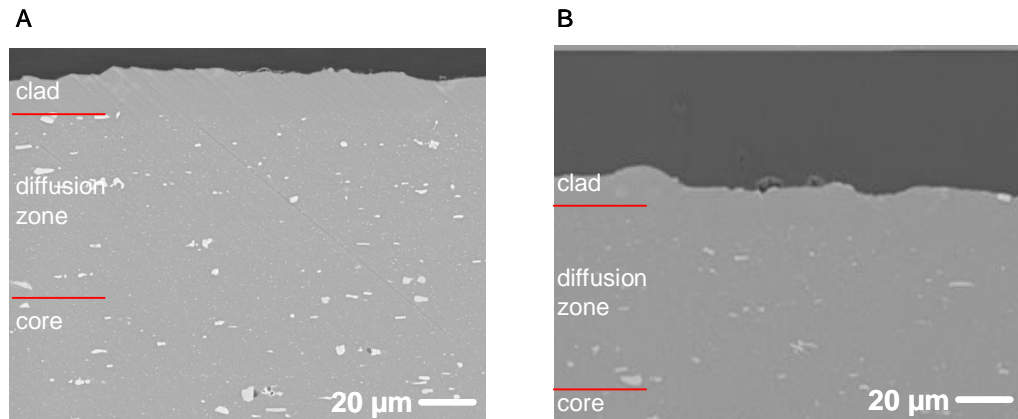


**Figure IV.2-4:** Micrographs of the cross-sections for AA4045/3003/4045 before (A) and after (B) the Erichsen impression.

### IV.3 Morphological results of AA4045/3003/4045 during SWAAT exposure

In order to investigate the electrochemical conditions in AA4045/3003/4045 brazing sheets, accelerated corrosion testing is performed. Prior to the salt spray testing, the samples have been degreased in an ultrasonic bath with acetone and ethanol for 5 min, each. Figure IV.3-1 presents the micrographs of the exposed cross-sections during SWAAT exposure.

After less than two days, the initiation of corrosion is seen in the outer layer (A). Considering this, the weakest point of the material is found in the eutectic of the re-solidified clad, since the aluminium matrix next to the more noble silicon is dissolved. The corrosion propagates as intergranular attack through the clad material (B). Finally, after 16 days of SWAAT exposure (C) it is observed that perforation of the core material occurs.

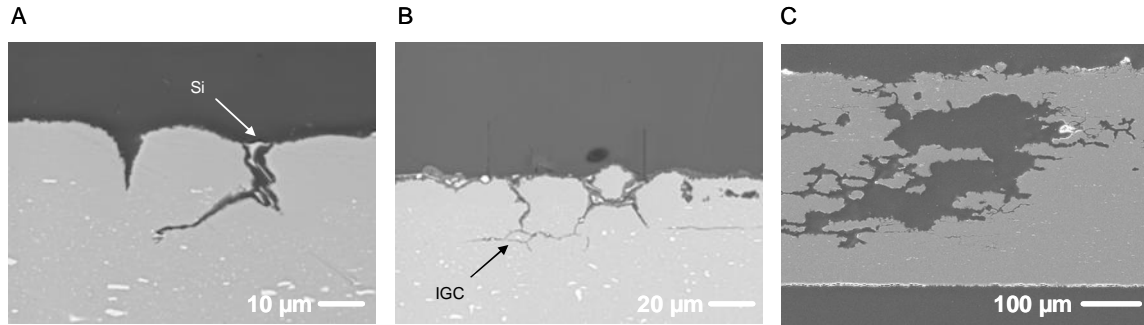


**Figure IV.3-1:** cross-sections of AA4045/3003/4045 after 2(A), 7(B), 16(C) days of SWAAT exposure.

The initiation of corrosion is located in the eutectic of the re-solidified clad material. Due to the high amount of silicon (12.6% in balance with aluminium), the eutectic is the last part to solidify after the brazing process. The aluminium adjacent to the more noble silicon is dissolved anodically (pitting). The more noble  $\alpha$ -aluminium grains are not attacked by the silicon. The corrosion propagates as inter-granular attack through the diffusion zone. This is explained by the high participation of alloying elements e. g. iron, silicon and manganese in the grain boundaries, dissolving the less noble aluminium matrix in the vicinity (B). This high concentration of alloying elements compared to the aluminium matrix is shown in the EDS analysis listed in [Table IV-3](#). The direction of the corrosion to the core material (C) is explained with the amount of Si and Mn in solid solution. During the heat treatment Si diffuses into the core and reduces the amount of  $[Mn]_{ss}$  in the diffusion zone, which is seen in the increased amount of Si-Mn precipitates. Lowering the  $[Mn]_{ss}$  decreases the corrosion resistance in the diffusion zone in comparison with the core material, since  $[Mn]_{ss}$  reduces the potential difference between the particles and the aluminium matrix. However this effect is balanced by the higher amount of  $[Si]_{ss}$  in the diffusion zone, due to the fact that not all Si is precipitated. Furthermore it is observed that the diffusion zone is not very thick and well developed, indicating that the decrease of  $[Mn]_{ss}$  is only in a small area in the diffusion zone compared to the more significant diffusion depth of silicon. Considering these results, the corrosion propagation found during SWAAT exposure is explained, since the attack of the core material is galvanically driven by the diffusion zone. The corrosion propagation is illustrated [Figure IV.3-2](#).

**Table IV-3:** Atomic concentration of elements found in the aluminium matrix and after IGC

Area	Al (at%)	Si (at%)	Fe (at%)	Mn (at%)	O (at%)	Cu (at%)	C (at%)
Al-matrix	93.3	0.5	0.1	0.1	1.5	0.1	4.3
Grain boundary	70.8	12.6	6.5	10.1	-	-	-

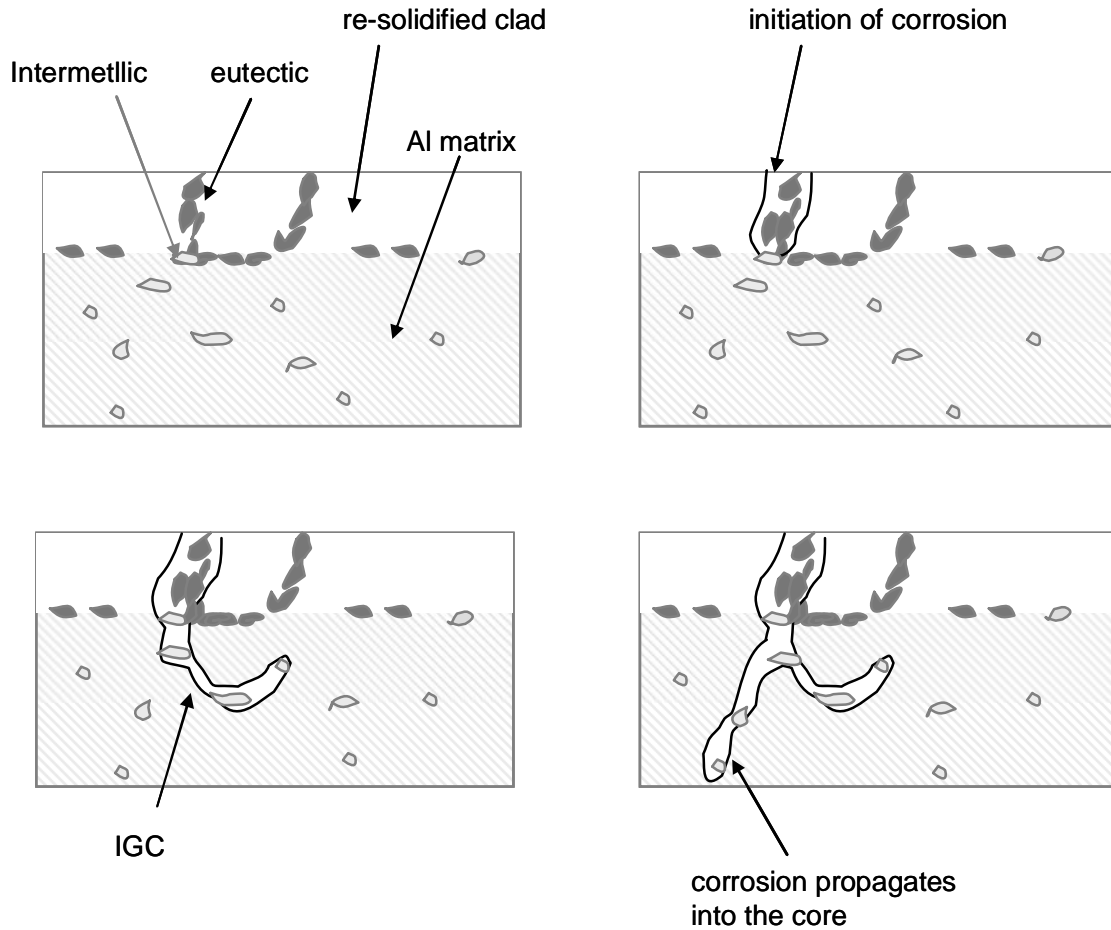


**Figure IV.3-2:** Schematic illustration of the corrosion propagation in the brazing sheets.

#### IV.4 Electrochemical analysis

In order to study the electrochemical behaviour of aluminium brazing sheets, open-circuit potential (OCP) measurements, potentiodynamic and potentiostatic polarization measurements were performed in combination with an investigation of the morphology

of attack. The aim is to gain information about the corrosion initiation and propagation and to correlate the corrosion performance with the microstructure.

#### IV.4.1 Recording the Open-Circuit-Potential (OCP) of aluminium brazing sheets

At the OCP the cathodic reaction rate:



is in equilibrium with the anodic reaction rate:



This correlation is given by<sup>53</sup>:

$$i_c \cdot A_c = i_a \cdot A_a \quad (3)$$

with

$i_c$ : cathodic current density

$A_c$ : area of the cathode

$i_a$ : anodic current density

$A_a$ : area of the anode.

Considering this equation (3), the OCP can be affected either by changes of the area of the cathode and the anode or by changes in the anodic or cathodic current densities. Afseth et al.<sup>11</sup> used this theory to explain the decrease of the OCP due to annealing at different temperatures of AA3005. They concluded that the decrease of the OCP was due to an increase of the anodic reaction rate, caused by an influence of the heat treatment on the passivity of the oxide layer. They excluded the possibility that the OCP decrease was due to an increase of the cathodic reaction rate, since they showed with other techniques that the OCP transient was not affected by the cathodic reaction rate.

However the equation is only valid for constant areas of cathode and anode during the measurements. Usually this is guaranteed by the cathodic areas, since the intermetallic phases are not attacked in the AA4045/3003/4045 brazing sheets. However the anodic area (aluminium matrix) next to the intermetallic phases is dissolved and hence the anodic area will increase due to this local attack. This results in an increase of the anodic reaction rate and is observed in a decrease of the transient. This behaviour is in accordance with the mixed potential theory, since a potential decrease is attributed to a

(possible) breakdown of the oxide passivation layer due to the attack of chloride ions. This dissolves the aluminium matrix (anodic reaction) and increases the anodic reaction rate. These results are consistent with the observations made by Afseth et al.<sup>11</sup>. On the other hand it is possible to associate an increase of the potential transient to a re-passivation of the surface by forming an oxide protection layer. A passive behaviour of the metal is reflected by a decrease of the anodic reaction rate and hence an increase of the potential transient. If the transient is passive, it means that the surface protects the underlying material from attack in the respective electrolyte.

Figure IV.4-1 shows the reproducibility of OCP transients of AA4045/3003/4045 during OCP measurements.

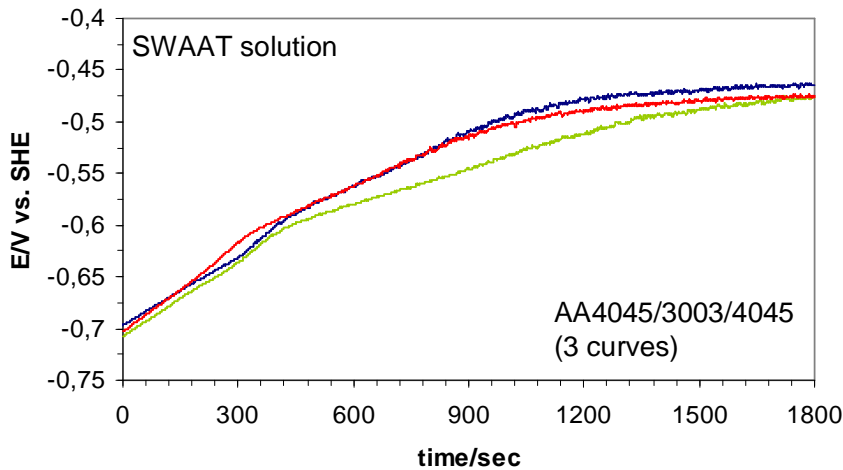


**Figure IV.4-1:** OCP transients within the multilayer aluminium system.

The curves reveal an increase during the first 20 min till the transient becomes stable. The stable behaviour of the transient after 30 min of recording is an indication that the surface protects the alloy against (local) attack. Since the OCP reflects the conditions in solid solution (aluminium matrix) the measuring conditions after 30 min will be used for the investigation of the brazing temperature and mechanical transformation. The initial increase indicates that the system requires some time in the electrolyte to receive stable conditions. This is due to the rough and inhomogeneous surface conditions and hence will not be considered in the discussion of the transients.

In order to investigate the potential differences between AA3003, which is used as core alloy in the multilayer system, and the entire brazing sheet (AA4045/3003/4045) the transients were recorded and are presented in [Figure IV.4-2](#). After 30 min. the OCP for AA3003 is -0.48 V and -0.46 V for AA4045/3003/4045.

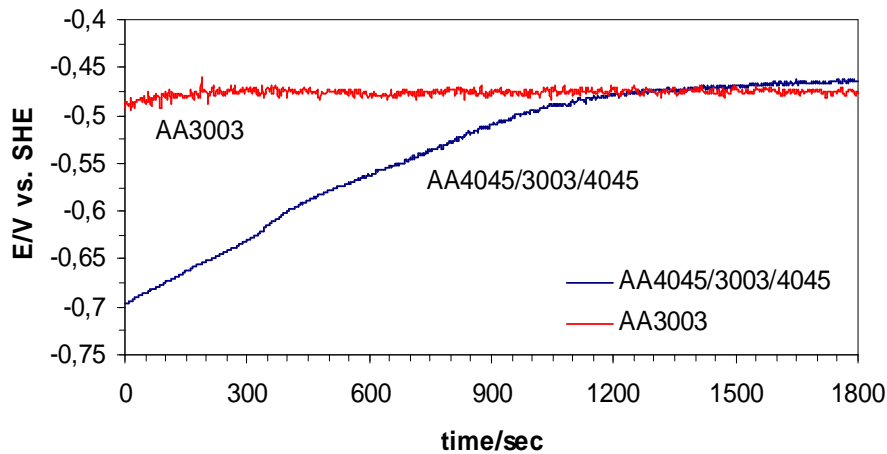


**Figure IV.4-2:** Potential transient of AA4045/3003/4045 and AA3003 measured for 30 min in SWAAT solution.

Although the processing of aluminium brazing sheets, particularly the brazing process has a strong influence on the composition of the solid solution, the microstructure of the core material is hardly affected. Hence, the changes in the potential values is caused by the clad and the diffusion zone. Although in that area the  $[Mn]_{ss}$  content is reduced, indicating a potential decrease of the system,  $[Si]_{ss}$  and  $[Cu]_{ss}$  in the aluminium matrix increased to balance the low manganese level and cause a more positive matrix of the brazing sheet in comparison to AA3003. This result is in accordance with the observations made during SWAAT, since the core material is galvanically attacked by the diffusion zone.

## IV.4.2 Potentiodynamic polarization curves of aluminium brazing sheets

Figure IV.4-3 shows the reproducibility of the potentiodynamic polarization curves of AA4045/3003/4045 and provides an introduction in the used technique. Prior to the polarization scans the OCP is measured for 30 min. The sample is polarized in the positive direction starting from -0.05 V vs. OCP (point A) to 0.40 V vs. OCP (point C). After the curve reveals the OCP in the forward direction (point B) the current density increases and shows two breakdown potentials, which are indicated in Figure IV.4-3. The current density corresponding to point C is referred as limit anodic current density. After that, the sample is polarized in the negative direction to -0.35 V vs. OCP (point F). The current density corresponding to point F is attributed to the limit cathodic current density. During the polarization in the backwards scan the current density decreases, indicating a re-passivating behaviour (point D) till the OCP in the backwards scan occurs (point E). After point F the sample is again polarized in the positive direction until the cycle is closed (point G).

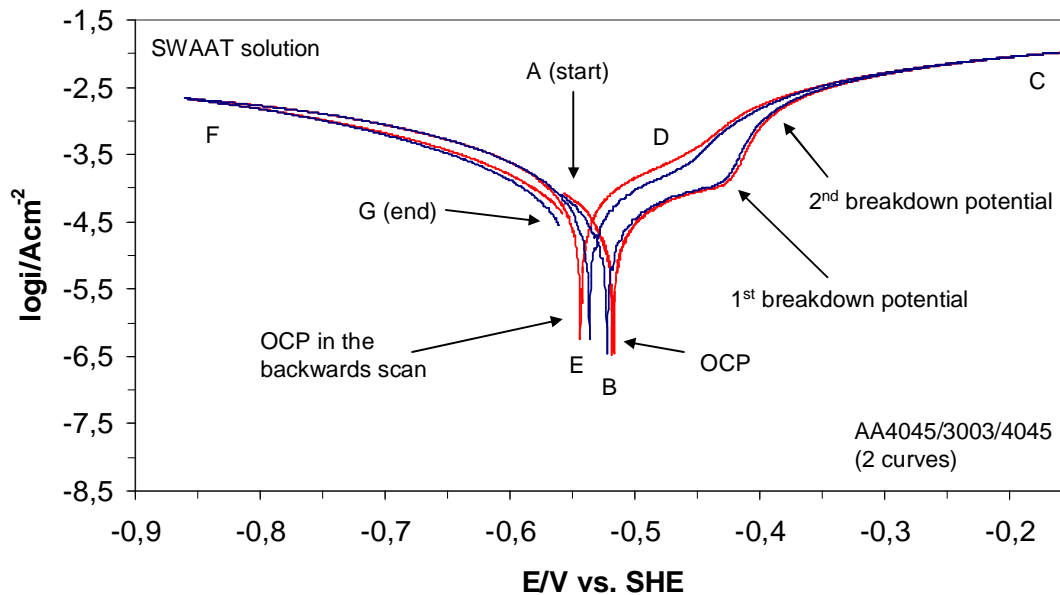


**Figure IV.4-3:** Reproducibility of potentiodynamic polarization measurements after measuring the OCP for 30 min in SWAAT solution for AA4045/3003/4045 brazing sheets.

In [Figure IV.4-4](#) the potentiodynamic polarization scans of AA4045/3003/4045 and AA3003 are shown.

The OCP (point A) for AA4045/3003/4045 (-0.52 V) is more negative than for AA3003 (-0.49 V). Besides, the former alloy reveals two breakdown potentials, the first breakdown potential occurs at -0.43 V and the second at -0.39 V, while there is only one in AA3003 (-0.48 V). The limiting anodic density (point B) is slightly higher for AA3003 than the other alloy and the opposite conditions are observed for the cathodic current density (point D). The re-passivation (point C) of the brazing sheet is more significant than for AA3003. Moreover the OCP in the backwards scan is shifted for both alloys in the negative reaction and occurs at the same potential (-0.54 V).

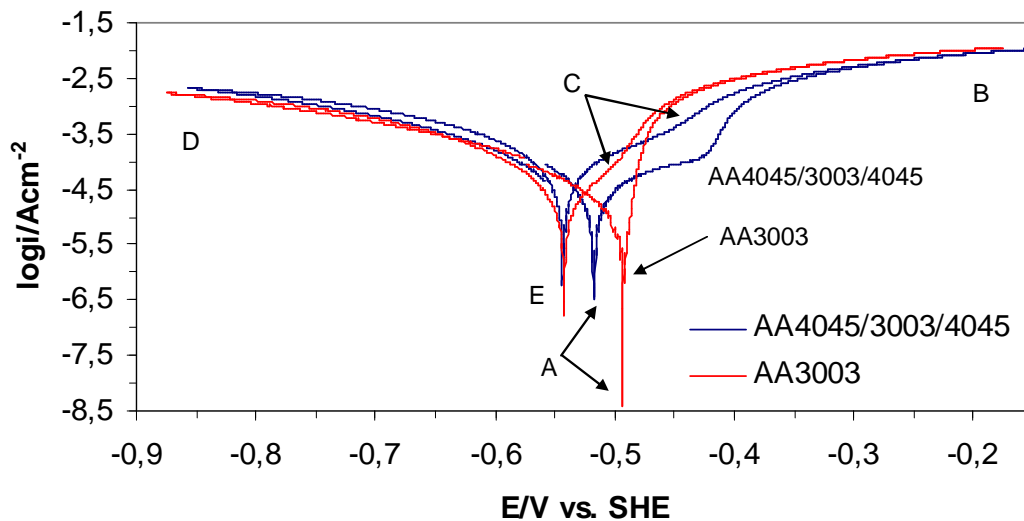


**Figure IV.4-4:** Potentiodynamic polarization scans of AA4045/3003/4045 and AA3003 in SWAAT solution.

The existence of a more negative OCP and two breakdown potentials for AA4045/3003/4045 is an indication of higher susceptibility to localized corrosion such as pitting and IGC compared to AA3003. This behaviour is also shown in the higher cathodic current density of AA4045/3003/4045, indicating higher localized corrosion around the intermetallics. This is in correlation with the SEM/ EDS measurements shown in [Figure IV.2-2](#). During the brazing process several intermetallic phases are formed, increasing the anodic current density. However, the re-passivation of AA4045/3003/4045

is more significant and the shift of the OCP in the backwards scan is less negative, indicating that the oxide layer is formed after the local attack to protect the alloy surface of further attack.

#### IV.4.3 Morphology of attack after OCP measurements

Figure IV.4-5 shows the exposed surface of AA3303 (A) and AA4045/3003/4045 (B). The samples are immersed for 30 min in SWAAT solution to measure the OCP. The surface of AA3003 (Figure IV.4-5 (A)) shows crystallographic pitting on the surface whereas no attack is observed on the surface of AA4045/3003/4045.

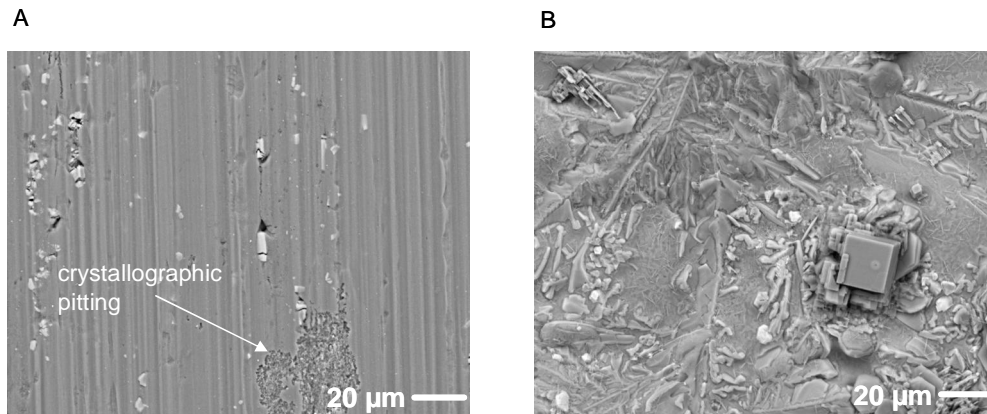


**Figure IV.4-5:** Micrographs of the exposed surface for AA3003 (A) and for AA4045/3003/4045 (B) after measuring the OCP for 30 min in SWAAT solution.

The appearance of crystallographic pitting at AA3003, but not at AA4045/3003/4045 is in correlation with the higher limit anodic current density for AA3003 compared to the brazing sheet. This indicates a higher susceptibility to general corrosion (crystallographic pitting) whether AA4045/3003/4045 is more susceptible to localized attack at the periphery of the intermetallic phases (higher limit cathodic current density).

#### IV.4.4 Morphology of attack after potentiodynamic polarization scans

Figure IV.4-6 shows the exposed surface and the cross-sections for AA3003 (A, B) and AA4045/3003/4045 (C, D) after potentiodynamic polarization in SWAAT solution (Figure IV.4-4). The surface of AA3003 shows several localized attack. At some areas

the attack is due to intermetallics however there are also areas where the attack seems to be randomly, since no intermetallics are present. The same situation can be observed in the cross-section. Mainly pitting occurred next to intermetallics and also in areas without any particles. The surface of AA4045/3003/4045 reveals large grains, since the aluminium matrix next to the grain boundaries is dissolved during intergranular corrosion. Moreover some pits are visible. In the cross-section the intergranular corrosion is clearly seen along the grain boundaries.

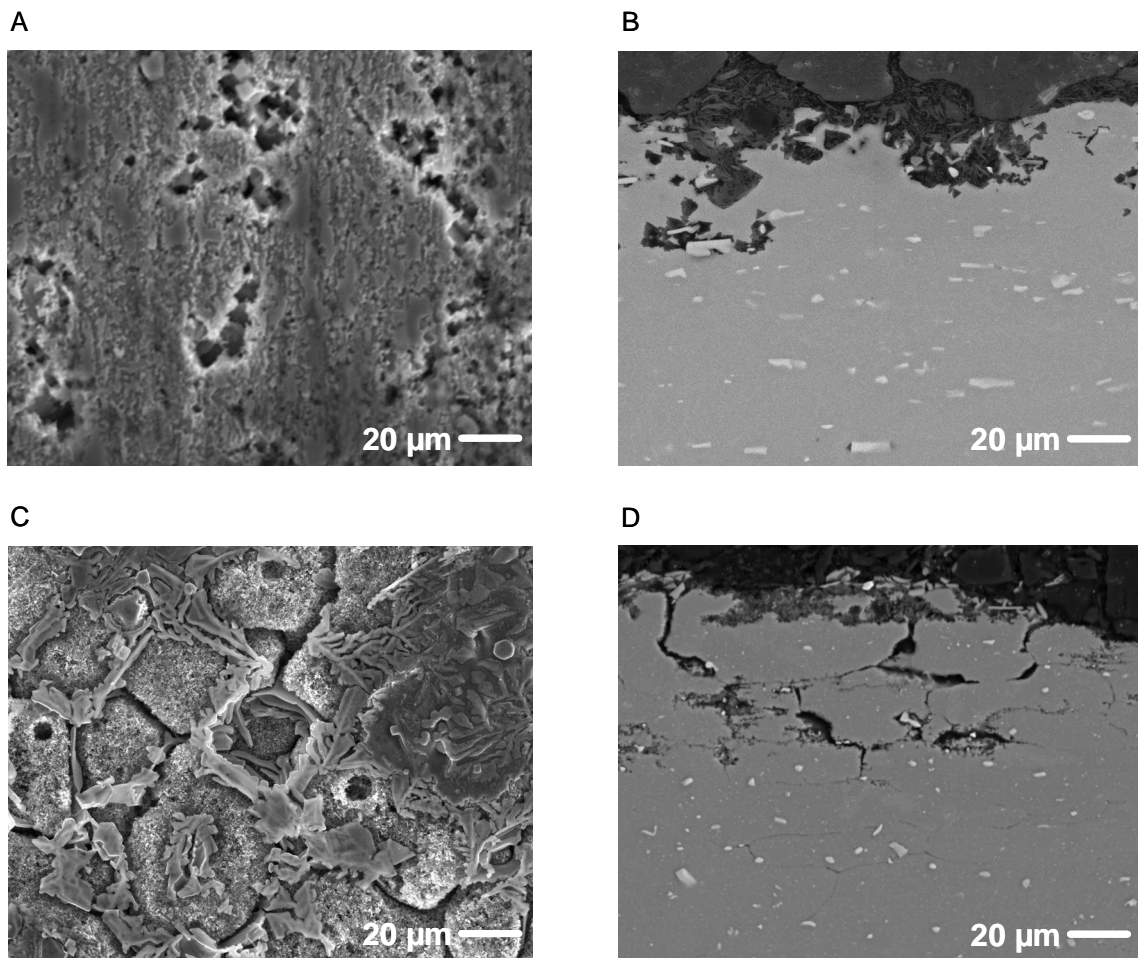


**Figure IV.4-6:** Micrographs of the exposed surface (A, C) and of the cross-section (B, D) for

The more severe localized attack at the intermetallics is explained by the more negative OCP in the potentiodynamic polarization curve of AA4045/3003/4045 than for AA3003. Furthermore the higher susceptibility of AA4045/3003/4045 to intergranular corrosion is

a consequence of the higher amount of precipitates formed during the brazing process located in the grain boundaries. As discussed previously the higher current density of AA4045/3003/4045 compared to AA3003 during the polarization scan in the negative direction can also be related to severe localized attack.

#### IV.4.5 Morphology of attack after potentiodynamic polarization at the 1st and 2nd breakdown potential

In order to investigate the appearance of two breakdown potentials for AA4045/3003/4045 during the potentiodynamic polarization in SWAAT solution, the morphology after the first and the second breakdown potential was investigated.

Figure IV.4-7 shows the exposed surface (A) and the cross-sections (B) after the first breakdown potential. On the surface localized attack (pitting) of the aluminium matrix around the more noble silicon particles can be observed. This attack on the surface is confirmed by the cross-sectional image. Around the intermetallics (silicon particles) the aluminium matrix shows an anodic behaviour and is dissolved. This is observed as pitting. The surface after the second breakdown potential (C) shows pits and intergranular corrosion. This local attack along the grain boundaries can be clearly seen in the cross-section (D).

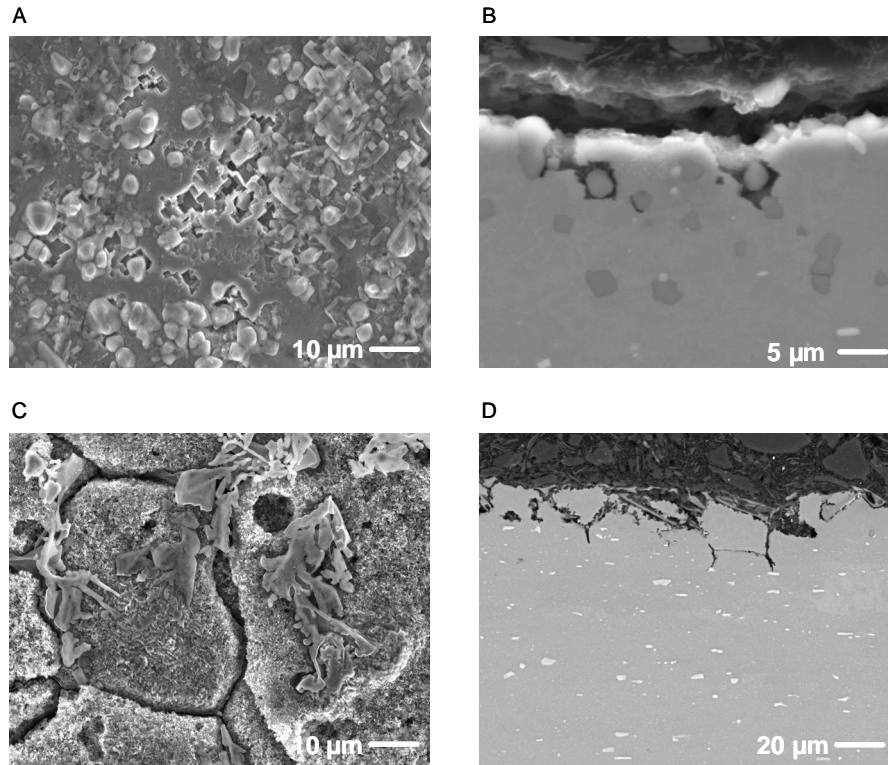


**Figure IV.4-7:** Micrographs of the exposed surface (A, C) and of the cross-section (B, D) of AA4045/3003/4045 after potentiodynamic polarization to the first and second breakdown potential in SWAAT solution.

The correlation between the breakdown potentials and the morphology of local attack was also observed by Zhang et al.<sup>4</sup> They investigated the local attack of AA2xxx alloys and attributed the first breakdown potential to pitting and the second breakdown potential to intergranular corrosion.

#### IV.4.6 Potentiostatic polarization at the breakdown potentials

By means of potentiodynamic polarization curves the initiation of pitting was attributed to the first breakdown potential and the transition to IGC to the second breakdown potential. However it should be considered that a two-breakdown polarization curve is the summation of currents from two different localized dissolution processes, which means that the lower current density found for IGC can be masked by the larger current density associated to the dissolution of the aluminium matrix next to the intermetallics.<sup>4</sup> To overcome this, each sample was polarized for one hour at one potential (potentiostatic

polarization measurements) to receive information of the localized dissolution at the respective potential. The aim was to define the potential area where IGC starts and to gain deeper insight in the initiation of IGC.

Figure IV.4-8 shows the cross-sections of AA4045/3003/4045 brazing sheets after potentiostatic polarization at  $-0.4$  V (A),  $-0.39$  V (B) and  $-0.37$  V (C).

Applying a potential at the first breakdown potential (A) initiation of corrosion was found at the intermetallic particles. Applying a potential below the second breakdown potential ( $-0.39$  V (B)) reveals the beginning of intergranular corrosion along the grain boundaries. It can be seen that the IGC takes place at the intermetallics and also at locations without the intermetallics. The potentiostatic polarization at a potential above the second breakdown potential (C) reveals a severe dissolution along the grain boundaries where intermetallic phases are located and also in the areas without intermetallics.

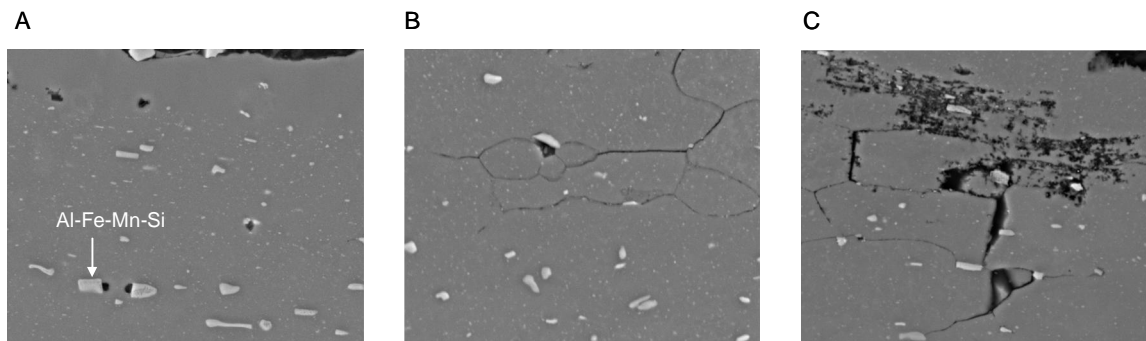


**Figure IV.4-8:** Cross-sections of AA4045/3003/4045 after potentiostatic polarization. Picture A shows the initiation of pitting next to the intermetallic phase. The pictures B and C show the beginning and propagation of IGC.

The initiation of pitting is forced by a galvanic attack of the more noble second phase particles. This effect is seen by the dissolution of the aluminium matrix in the vicinity. Increasing the applied potential, the propagation of the corrosion is mainly driven by pitting along the grain boundaries. These pits develop into IGC, independent of the intermetallic phases. This is observed in the morphology of the sample, since the initiation of IGC can be seen as fine threads along the grain boundaries, independent of the intermetallics. An explanation of this behaviour is found in the differences of breakdown potentials between the aluminium matrix, the intermetallic phases and the

grain boundaries. Pitting corrosion found at the first breakdown potential is initiated by the difference in breakdown potentials of the more noble intermetallics among the aluminium matrix. By increasing the applied potential close to the second breakdown potential, the breakdown potential difference between the aluminium matrix and the grain boundaries is the driving force for the initiation and propagation of IGC. However the large pits formed next to the intermetallics are an initiation point for IGC. These observations are similar to the report of Buchheit et al.<sup>5</sup>. They found this corrosion propagation in AA2090 alloy. As observed, the transformation of pitting to IGC occurs below the attributed second breakdown potential. This is explained by the locally varying concentrations of intermetallics in the grain boundaries, causing a potential range where IGC initiates instead of one single potential.

#### IV.4.7 Comparison of corrosion propagation by potentiostatic polarization and SWAAT

As observed by morphological investigations, the combination of potentiodynamic and potentiostatic polarization measurements is a powerful tool to investigate the corrosion behaviour of an aluminium alloy. Potentiodynamic polarization curves enable the attribution of breakdown potentials to the respective forms of localized attack. By means of potentiostatic polarization of the defined breakdown potentials these forms of localized attack can be induced. In order to investigate the correlation of the corrosion propagation during SWAAT and potentiostatic polarization measurements, morphological investigations of samples exposed to the salt spray test and after the polarization scans were performed. The aim is to find a correlation of corrosion propagation during SWAAT and with the electrochemical techniques.

Figure IV.4-9 (A-C) presents the cross-sections of AA4045/3003/4045 brazing sheets exposed for 2 (A), 7 (B) and 12 (C) days to SWAAT and after potentiostatic polarization measurements for one hour at the first breakdown potential (-0.43 V (D)), the second breakdown potential (-0.39 V(E)) and above the second breakdown potential (-0.35 V(F)).

Comparing the exposed cross-sections of both accelerated corrosion techniques the same corrosion propagation is observed. The corrosion initiates in the eutectic in the re-solidified clad, by a galvanically forced dissolution of the aluminium matrix next to the more noble silicon (A, D), propagates as IGC through the diffusion zone (B, E) and continues to the core material (C, F).

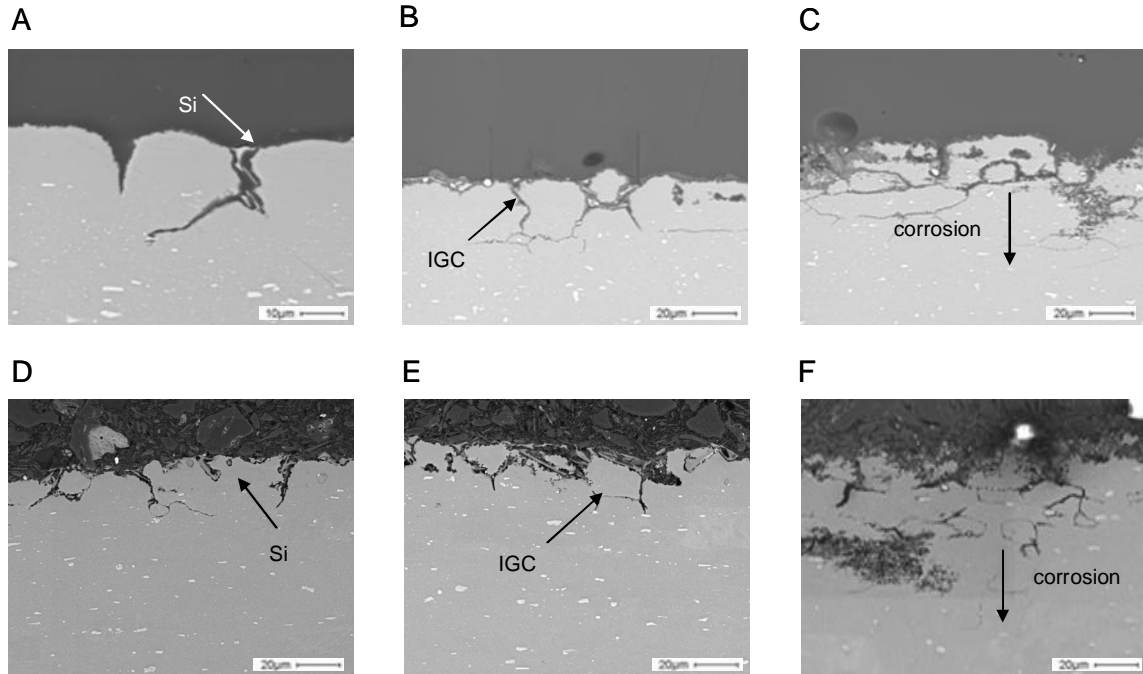


**Figure IV.4-9:** Comparison of accelerated corrosion testing on AA4045/3003/4045 during SWAAT exposure (A-C) and potentiostatic polarization (D-F).

Considering the results, it is possible to simulate the initiation and propagation of corrosion on aluminium brazing sheets by electrochemical techniques in the same way as during SWAAT exposure. Although it was not possible to receive a complete perforation of the brazing sheet within one hour of polarization, this technique is a proper method to evaluate the corrosion performance of a material, since the crucial properties such as corrosion initiation and propagation within the material can be investigated.

## IV.4.8 Effect of brazing temperature on the open circuit potential

Figure IV.4-10 presents the OCP curves of samples brazed under standard conditions (590°C), brazed under enhanced temperatures (615°C) and without brazing.

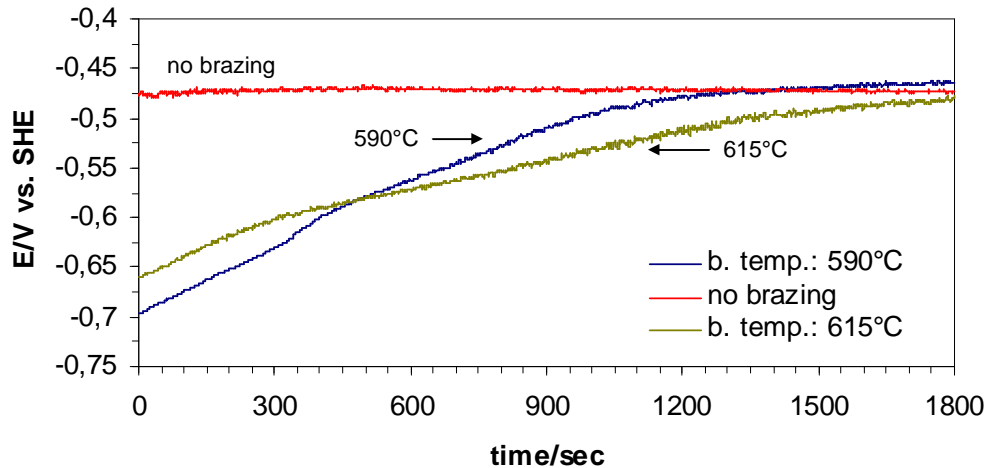


**Figure IV.4-10:** OCP of AA4045/3003/4045 after various brazing temperatures measured for 30 min in SWAAT solution.

After 30 min the OCP is -0.48 V for the sample brazed at 615°C, -0.47 V for the pre-brazed material and -0.46 V for the material brazed under standard conditions (590°C). Therefore the sample brazed under standard conditions showed a shift of the OCP from the un-brazed material in the positive direction, however increasing the temperature showed a shift of the OCP in negative direction in comparison to the un-brazed material. The positive effect of the brazing process can be explained by the increase of  $[Si]_{ss}$  and  $[Cu]_{ss}$  in the re-solidified clad material and the diffusion zone compared to the un-brazed material. This was discussed previously. Increasing the brazing temperature shifts the OCP in the negative direction. This is explained by an increase of the diffusion rate by increasing the brazing temperature. Due to that, the precipitation of silicon, manganese and copper in the aluminium matrix is increased, reducing the OCP.

#### IV.4.9 Effect of brazing temperature on the potentiodynamic polarization

Figure IV.4-11 presents the potentiodynamic polarization curve of AA4045/3003/4045 brazed under standard conditions (590 °C), brazed under enhanced temperatures (615 °C) and without brazing.

The pre-brazed sample and the sample brazed under high temperatures reveal less distinctive breakdown potentials than the sample brazed under standard temperature. The OCP in the forward scan (point A) for the un-brazed sample occurs at - 0.5 V, for the sample brazed with high temperatures at - 0.48 V and for the standard process at - 0.52 V. The first breakdown potentials for the samples under standard conditions and at high temperatures are very similar. The pre-brazed sample is shifted in negative direction. These conditions differ in the OCP in the backwards direction. At that point the pre-brazed material and the sample under standard conditions are similar. The sample with high brazing temperatures is shifted in positive direction. In correlation to that, the decrease of the current density due to re-passivation (point C) is more significant of the sample brazed under high conditions compared to the other materials. Moreover, the values of the limit anodic density (B) are comparable for all samples however the limit cathodic density (D) is slightly higher for the standard conditions.

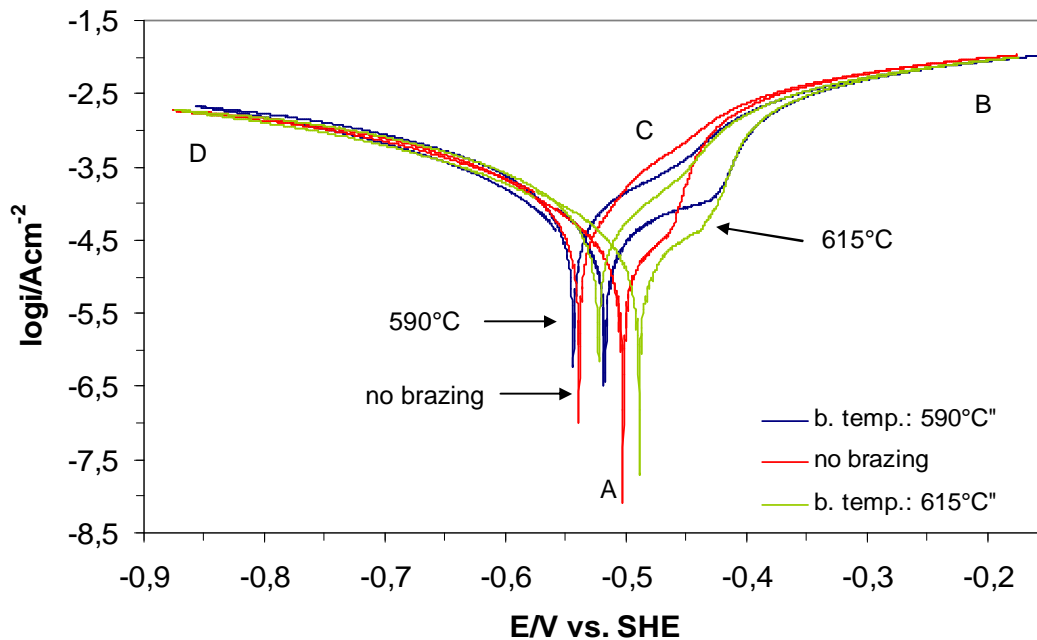


**Figure IV.4-11:** Potentiodynamic polarization curve for AA4045/3003/4045 with various brazing temperatures measured in SWAAT solution.

The more positive value of the OCP by increasing the brazing temperature indicates lower susceptibility to localized corrosion (intergranular corrosion). This is also confirmed by the lower current density during polarization in the negative direction. Increasing the brazing temperature increased the Si diffusion rate. This leads to a progressive precipitation of Al-Mn-Si around the grain boundaries and hence to a reduction of the corrosion potential difference between the matrix and the grain boundaries. Furthermore, the significant re-passivation behaviour and the more positive OCP in the backwards scan indicate good protection properties of the surface after localized corrosion, avoiding further attack of the material.

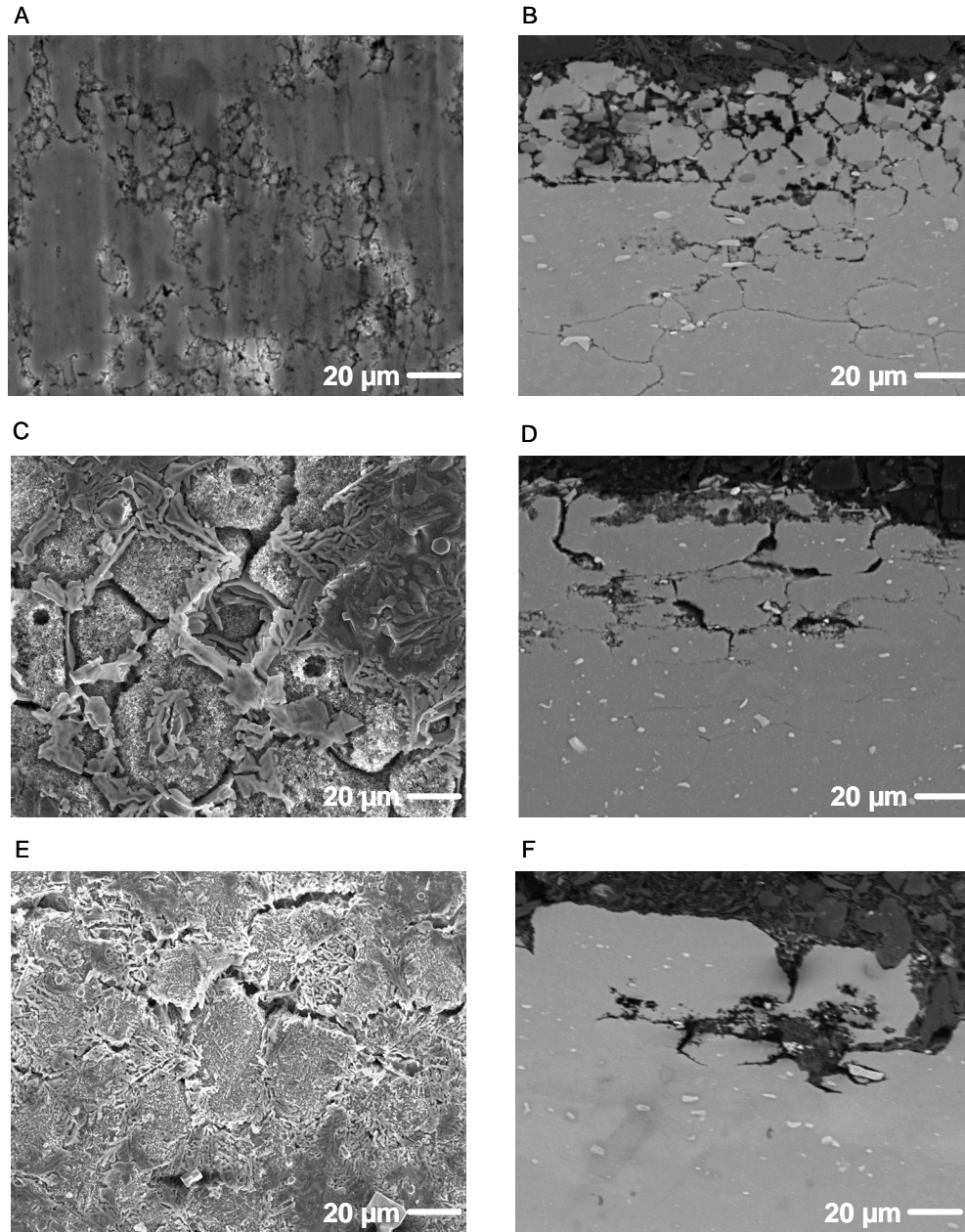
#### IV.4.10 Effect of the brazing temperature on the morphology of attack

Figure IV.4-12 shows the exposed surface (A, C, E) and the cross-sections (B, D, F) of AA4045/3003/4045 after various brazing temperatures.

The exposed surface of un-brazed AA4045/3003/4045 exhibits a strong localized dissolution of the aluminium matrix, due to the high concentration of silicon in the clad

alloy. Besides the cross-section (B) reveals intergranular attack, since the dissolution of the aluminium matrix follows the grain boundaries. Moreover the IGC shows a progress into the core material. The depth of the corrosion is around 100  $\mu\text{m}$ . The attack of the surface of the sample produced under standard brazing conditions reveals pitting and IGC attack. This behaviour is also observed in the cross-section. The depth of the corrosion path is around 70  $\mu\text{m}$ . Although the corrosion attack is less severe on the surface of the material brazed under high temperatures (E), IGC can be observed. This form of localized attack is also observed in the cross-section (F). The depth of the corrosion (around 40  $\mu\text{m}$ ) is less than for the other brazing temperatures.

In the pre-brazed material the clad alloy contains around 11 wt% of silicon. These silicon particles can be observed in the SEM images (Figure IV.2-1) as dark precipitates. Since silicon is more noble than the aluminium matrix, dissolution of the matrix next to the particles occurs. Usually AA3xxx alloys are not susceptible to intergranular corrosion (Figure V.13 (A, B)), hence it is concluded that the cladding process is responsible for the severe intergranular corrosion attack. The less strong corrosion attack in the samples brazed under high temperatures can be explained by a higher density of precipitates in the diffusion zone and the clad material. By increasing the brazing temperature, the diffusion rate of the alloying elements increases. The clad material will be higher in copper and manganese and lower in silicon. Hence the diffusion zone is higher in silicon and less in copper and manganese. Particularly copper can be very harmful to the corrosion resistance of a material. In lower concentrations it can form a favourable potential distribution. However if the concentration exceeds a certain level it accelerates the galvanically driven corrosion of the aluminium matrix. A higher copper content in the clad material of the sample brazed under high temperature can also be an explanation for the preferred corrosion attack in the clad material, acting as a sacrificial anode for the remaining part of the brazing sheet. Furthermore the beneficial effect of high temperatures on the diffusion rate of manganese to the clad material is less significant, since the diffusion of manganese is much lower than that of silicon and copper.



**Figure IV.4-12:** Micrographs of the exposed surface (A, C, E) and cross-sections (B, D, F) for AA4045/3003/4045 with various brazing temperatures after potentiodynamic polarization in SWAAT solution.

## IV.4.11 Effect of mechanical transformation on the open circuit potential

Figure IV.4-13 presents the OCP curves for AA4045/3003/4045 brazing sheets under standard conditions (plane material) and after mechanical transformation (deep-drawn material).

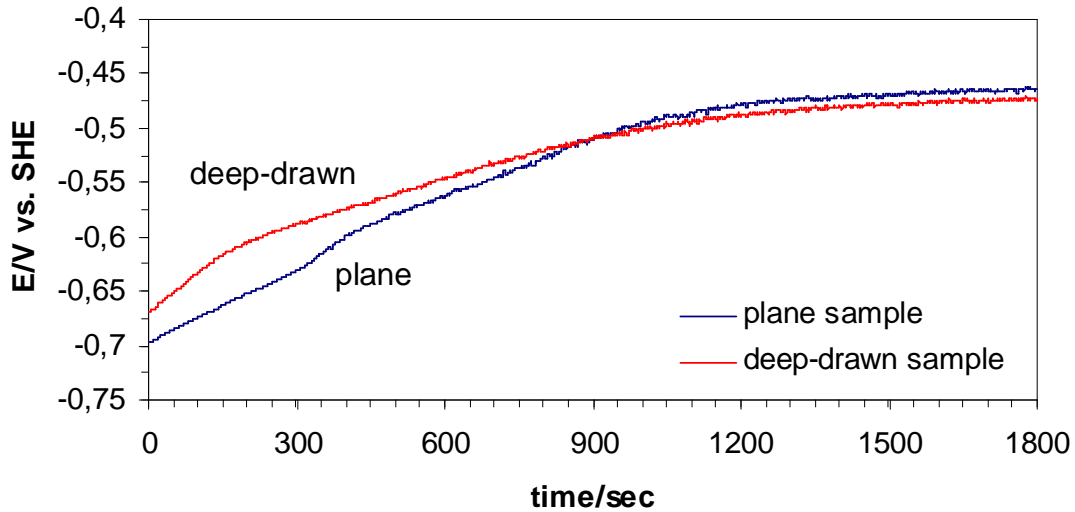


**Figure IV.4-13:** OCP of AA4045/3003/4045 before and after mechanical transformation measured for 30 min in SWAAT solution.

The OCP after 30 min is  $-0.46$  V for the plane sample and  $-0.48$  V for the deep-drawn sample. Therefore mechanical transformation causes a shift of the OCP in the negative direction. This is explained by an increase of the anodic reaction rate by a failure of the native oxide layer caused by the mechanical transformation and resulting in preferred areas for localized attack. The correlation between the decrease in the OCP and local breakdown of the oxide passivation layer was given by Afseth et al.<sup>11</sup>

#### IV.4.12 Effect of mechanical transformation on the potentiodynamic polarization

Figure IV.4-14 presents the potentiodynamic polarization curves of AA4045/3003/4045 brazing sheets under standard conditions (plane samples) and after mechanical transformation (deep-drawn samples) in SWAAT solution.

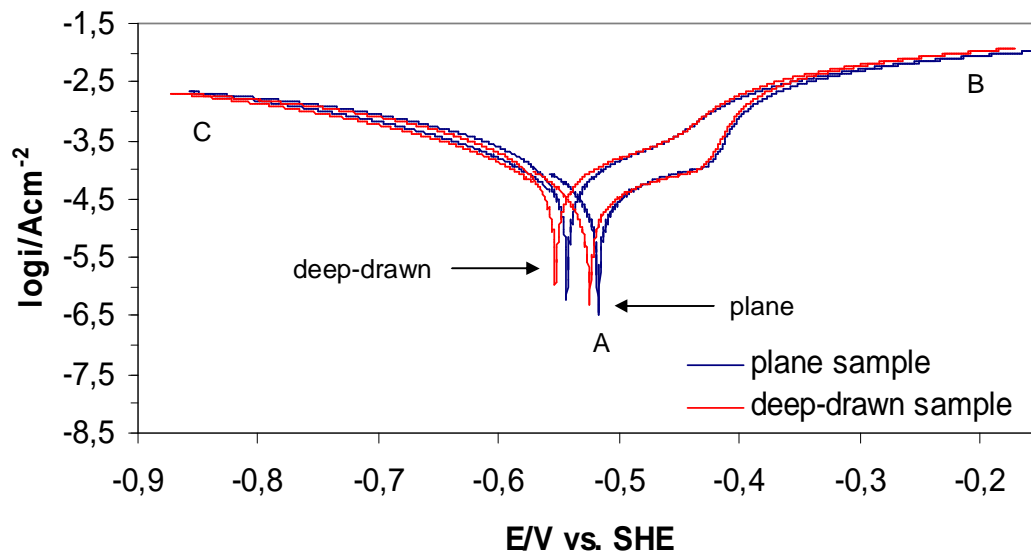


**Figure IV.4-14:** Cyclic Voltammetry scans for plane and deep-drawn samples (AA4045/3003/4045).

Hardly any differences can be observed for the plane and the deep-drawn sample. The OCP both in the forward and in the backward scan is shifted in the negative direction for the deep-drawn material in comparison to the plane material. Moreover the limit anodic density is slightly higher for the deep-drawn sample.

The existence of a less noble potential for both OCP values and the current densities for the deep-drawn sample demonstrates an increase of the susceptibility to localized attack. This behaviour is probably caused by the fracture of the native oxide layer, causing weaker areas for the initiation of localized attack.

IV.4.13 Effect of mechanical transformation on the morphology of attack

Figure IV.4-15 shows the exposed cross-section for AA4045/3003/4045 under standard conditions (plane sample (A)) and after mechanical transformation (deep-drawn sample (B)) after potentiodynamic polarization in SWAAT solution.

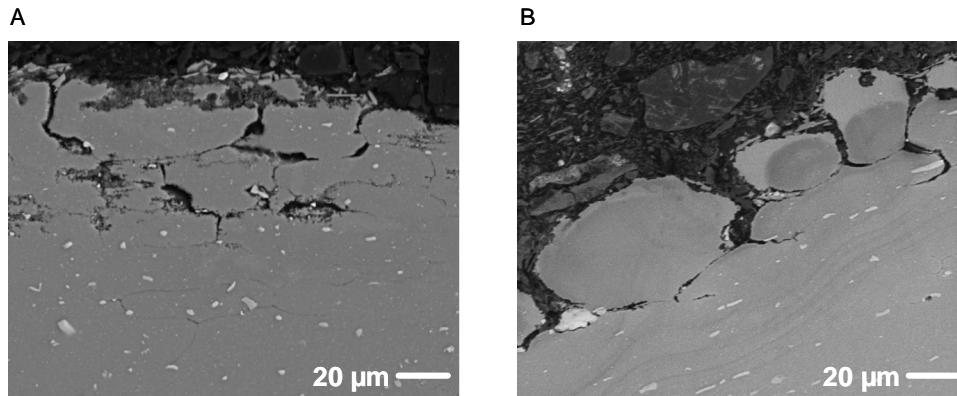


**Figure IV.4-15:** Micrographs of the exposed cross-section AA4045/3003/4045 before (A) and after (B) mechanical transformation after potentiodynamic polarization in SWAAT solution.

After the deep-drawing process, the intermetallic particles show an elongated shape due to the mechanical transformation. Moreover the grains seem to be more separated revealing a gap between each other. Anyway causing the mechanical stress on the material shows no influence on the corrosion progress. The deep-drawn sample shows intergranular attack in the grain boundaries as observed for the plane material.

## IV.5 Conclusion

In this chapter, the relation between the microstructure and the electrochemical behaviour of AA4045/3003/4045 brazing sheets is discussed. For this reason accelerated corrosion tests by means of salt spray testing (SWAAT) and electrochemical techniques were performed. Furthermore the effect of the brazing temperature and mechanical transformation on the corrosion behaviour was investigated under the following material conditions:

- as-received material (standard conditions: brazed at 590°C, not mechanically transformed)

- pre-brazed material (not mechanically transformed)
- material brazed at 615°C (not mechanically transformed)
- deep-drawn as received material (Erichsen impression).

During SWAAT exposure and electrochemical measurements the following corrosion propagation for the brazing sheets was found:

- 1) start in the eutectic of the re-solidified clad. The aluminium matrix next to the more noble silicon was galvanically dissolved (pitting)
- 2) in the diffusion zone, pitting transforms to IGC and continues along the grain boundaries
- 3) corrosion of the core material, galvanically driven by the diffusion zone.

This corrosion propagation is given by the potential differences between the clad, the diffusion zone and the core material caused by the diffusion of the alloying elements. The effect of the various elements on the corrosion behaviour is presented in Figure IV.5-1.

The investigation of the brazing temperature by electrochemical techniques showed an increase of the corrosion resistance by increasing the brazing temperature, caused by a sacrificial behaviour of the clad material and the diffusion zone due to increased precipitation.

Furthermore comparable corrosion initiation and propagation during SWAAT exposure and electrochemical techniques was found. This correlation provides the substitution of the conventional salt spray test by potentiodynamic and potentiostatic polarization measurements reducing the measuring time from several weeks to less than one day.

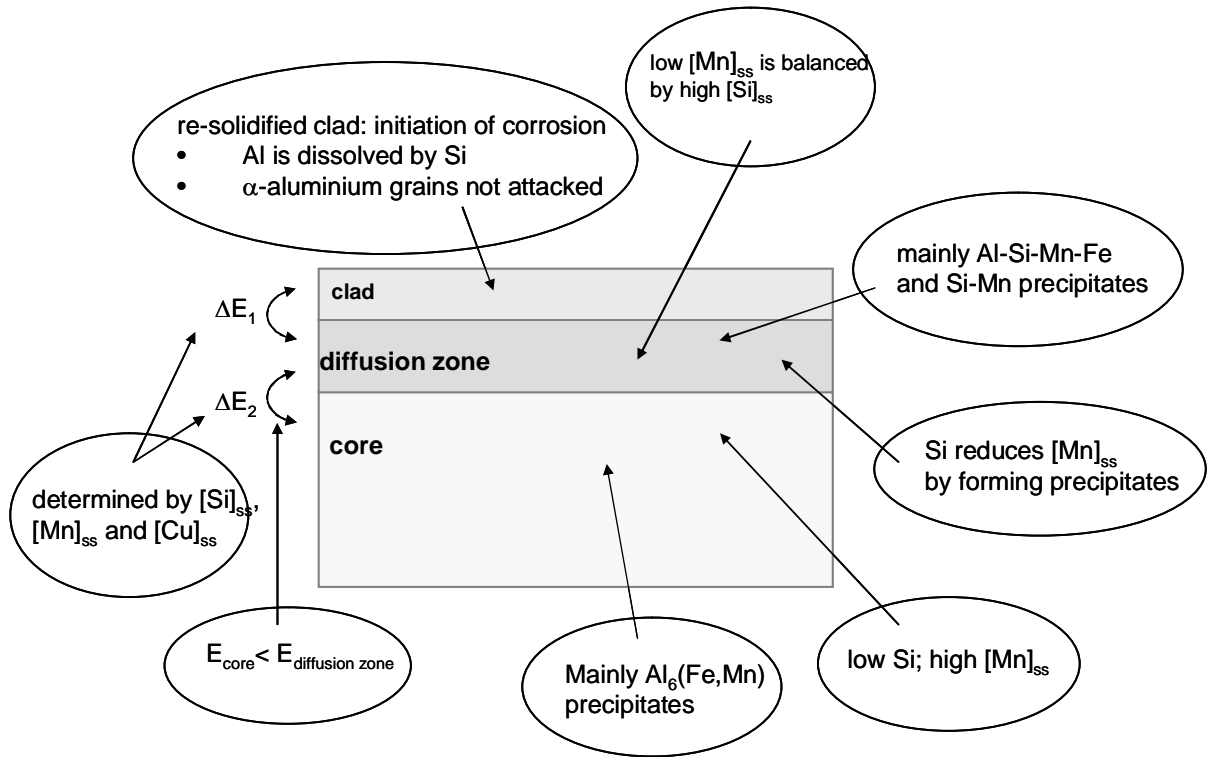


**Figure IV.5-1:** Effect of the alloying elements on the corrosion behaviour of post-brazed AA4045/3003/4045.

---

## CHAPTER FIVE

---

# THE SILICA PASSIVATION LAYER

## **Abstract**

*In this chapter the characterization of the silica passivation layer is discussed by means of Raman spectroscopy, field emission scanning electron microscopy in combination with energy dispersive spectroscopy (FE-SEM/EDS), X-ray photoelectron spectroscopy (XPS) and open circuit potential measurements (OCP).*

*Raman spectroscopy: since this technique can be used for solutions and for solids, it enables a correlation between the silicate components being present in solution and after deposition on the substrate.*

*In-situ OCP: by monitoring the OCP in solution during the deposition of sodium silicate on aluminium, the electrochemical reactions going on at the surface are recorded continuously as a function of time. Hence this technique enables information about the deposition conditions in-situ.*

*FE-SEM/EDS: detailed information about the morphology, the thickness and elemental composition of the layer. Particularly the effect of various deposition conditions on the ratios between Si, O and Na were in the focus to receive information about the uniformity of the layer. However since the penetration depth of the electron beam is around 1  $\mu\text{m}$  it is difficult to receive quantitative information about elemental composition in the outer layer.*

*XPS: this technique enables the elemental composition and chemical state of the atoms present in the outer layer of the coating. Moreover it is possible to gain chemical information within the silicate layer by performing depth profiling. With this method the coating is removed layer by layer by Ar sputtering. Between the sputtering intervals the remaining surface is analysed, resulting in chemical information as a function of the layer depth.*

*After the deposition of silica on a substrate, three significant transitions within the silica layer are proposed:*

- on the surface mainly  $\text{Na}_2\text{CO}_3$  was found, which is present in the sodium silicate solutions*
- in the bulk of the layer mainly  $\text{SiO}_2$  is present in polymeric form*
- in the interface between substrate and layer various components were found, containing silicates (as disilicates and polymers) and different compounds consisting of Al, Si and O.*

*The layer thickness is dependent on the bath concentration and independent of the dipping time. The potential transients showed that the deposition of the silicates takes place within the first 10 to 20 sec by a physical adsorption.*

*Furthermore, the various deposition conditions showed hardly any effect on the O/Si ratio, but a high variation in the Si/Na and O/Na ratios.*

## V. Investigation of the sodium silicate passivation layer

### V.1 Introduction

In order to gain chemical information about the silicate passivation layer, various methods including Raman spectroscopy, field emission scanning electron microscopy (FE-SEM) equipped with energy dispersive spectrometry (EDS) and X-ray photoelectron spectroscopy (XPS) have been used. Since no investigations about sodium silicates deposited on an aluminium substrate have been performed, there is a huge gap to fill about the background of the mechanism of the deposition and the chemistry of the deposited layer. For this purpose parameters such as bath concentration and temperature concerning the conditions in aqueous sodium silicate solutions as well as the drying conditions of the deposited silicates are of essential importance, since particularly the heat treatment ensures a stable and water-insoluble layer by curing the silicates. For gaining an insight in the cohesion between deposition parameters and layer properties, coatings with various bath concentrations, curing times, curing temperatures and dipping times have been investigated.

Since the deposition of the silica layer was applied in aqueous solution, Raman spectroscopy is performed to gain information about the components present in solution and after the deposition on a metal substrate. Particularly the level of polymerisation before and after the deposition is in the focus. The nature of the deposition process itself is investigated by electrochemical measurements. For this purpose the OCP is measured in aqueous silicate solution to gain an answer on the question if the deposition of the silicates is electrochemically driven or if the components are physically adsorbed.

The effect of the various deposition conditions (bath concentration, curing time, curing temperature and dipping time) on the morphology and the layer thickness are investigated by FE-SEM analysis of the surface and the cross-section. Moreover the effect of various deposition conditions on the Si, O and Na ratios is measured with EDS as an indication of the uniformity of the layer. To complete the EDS results a XPS survey scan is performed, to receive additional chemical information on the outer layer of the coating. Furthermore

an elemental analysis as well as a chemical state analysis as a function of depth is performed by depth profiling.

## V.2 Raman analysis

### V.2.1 Sodium silicate in aqueous solution:

In order to study the conditions of aqueous sodium silicates with different concentrations, Raman spectroscopy is performed. For this purpose a commercial product is used to adjust different bath concentrations (0.2 m, 1.1 m, 2.0 m and 3.0 m SiO<sub>2</sub>) by diluting with distilled water. The pH of the solution is around 10.8. Figure V.2-1 shows the spectrum of sodium silicate in aqueous solution with different concentrations, ranging from 0.2 m to 3.0 m SiO<sub>2</sub>. The spectrum range is shown between 1200 cm<sup>-1</sup> and 500 cm<sup>-1</sup>. The graphs according to 1.1 m, 2.0 m and 3.0 m SiO<sub>2</sub> show two absorption bands, at 779 cm<sup>-1</sup> and 1039 cm<sup>-1</sup>. The intensity of the band at 1039 cm<sup>-1</sup> decreased by decreasing the SiO<sub>2</sub> bath concentration. The band at 779 cm<sup>-1</sup> showed a slightly higher intensity at a bath concentration of 2.0 m SiO<sub>2</sub> compared to 3.0 m and 1.1 m SiO<sub>2</sub>. However, due to the low intensity of the peaks, it is difficult to receive clear conclusions. It turned out that the absorption band at 842 cm<sup>-1</sup> is due to a defect of the instrument, since this peak is also found in a reference measurement with pure water.

Based on the literature data<sup>42</sup> the attribution of the intensities to vibrations are listed in Table V-1.

**Table V-1:** Assignments of Raman vibrations of sodium silicate solutions

Frequencies (cm-1)	Assignment
1039	vas (Na)O-Si-O(H)
779	δas (H)O-Si-O(H)

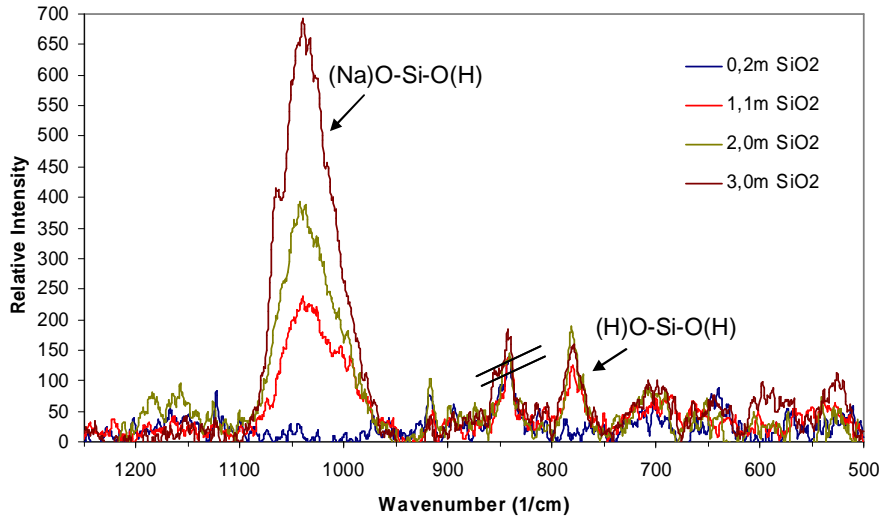


**Figure V.2-1:** Raman spectroscopy of sodium silicate solutions with various concentrations.

### V.2.2 Deposition of sodium silicate on aluminium:

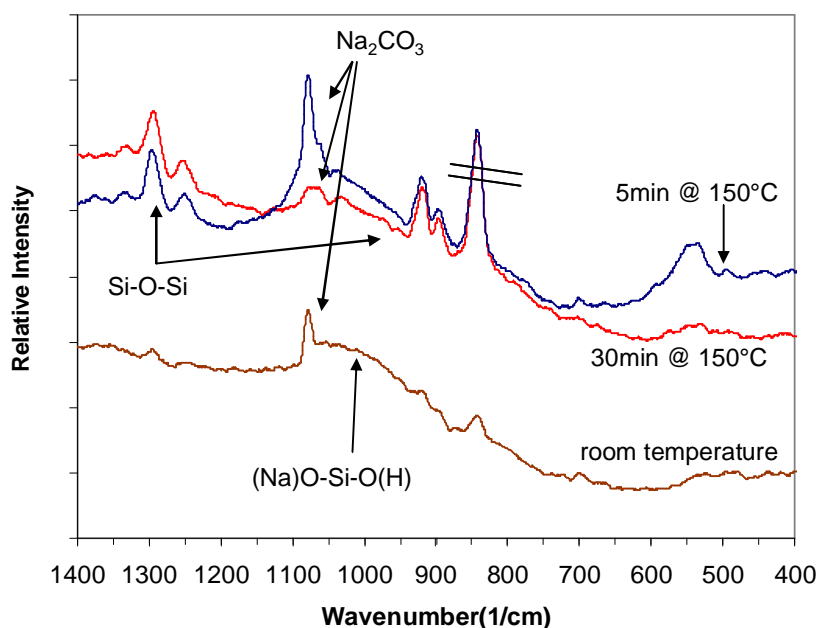
In addition to the measurements in solution, Raman scans were also performed on coated aluminium substrates. For this purpose Al99.99% samples are immersed in a 1.1 m SiO<sub>2</sub> solution to deposit the silicate layer on the surface and cured at various curing times to follow the effect of the curing time on the polymerisation level of the coating. The deposition conditions are described in Chapter III.

Figure V.2-2 shows the measurements made on the aluminium substrate after curing at room temperature for 24 hours (A), for 5 min at 150°C (B) and for 30 min at 150°C (C). After curing at room temperature (A) very weak bands at 1287 cm<sup>-1</sup> and 913 cm<sup>-1</sup> and a strong band at 1075 cm<sup>-1</sup> are observed. The spectra of the samples cured for 5 min and 30 min at 150°C reveal additional stronger intensities at 914 cm<sup>-1</sup> and 1289cm<sup>-1</sup>. Besides, the band at 1075 cm<sup>-1</sup> sample decreased after curing for 30 min.

Due to literature reference values,<sup>54</sup> the attribution to Raman vibrations is shown in Table V-2.

**Table V-2:** Assignments of Raman intensities of sodium silicate deposited on aluminium

Frequencies ( $\text{cm}^{-1}$ )	Assignment
1289	? Si-O
1075	$\text{Na}_2\text{CO}_3$
914	? Si-O

**Figure V.2-2:** Raman spectroscopy of sodium silicate in solution and deposited on Al99.99%. Data are presented as recorded.

### V.2.3 Discussion

Raman measurements are performed in aqueous sodium silicate solutions and after the deposition on aluminium substrates. Comparing the measured spectra with data found in literature it was possible to attribute the intensities to certain siloxane bondings. The assignments are listed in [Table V-1](#) and V-2.

Halasz et al.<sup>42</sup> suggested a dependency of the vibrational spectra on the sodium ion dissociation. They suggested that in 2-3mol/L aqueous solutions of  $\text{Na}_2\text{SiO}_3$  mainly  $\text{Na}_2\text{H}_2\text{SiO}_4$  monomers are present, dissociated about 30-80%. Due to the increasing

intensity of the band at  $1039\text{ cm}^{-1}$  (Figure V.2-1) with increasing bath concentrations, this band is associated to sodium related vibrations. Since the intensity of the band at  $779\text{ cm}^{-1}$  showed no significant influence on the changing bath concentrations (vibration is not related to sodium) and only appeared in aqueous solution, it was attributed to Si-OH vibrations. The strongest Raman bands appearing around  $1075\text{ cm}^{-1}$  recorded on an aluminium substrate (Figure V.2-2) are attributed to  $\text{Na}_2\text{CO}_3$ , since this compound is present as contamination in silicate solutions. This observation was also made by Halasz.<sup>42</sup> The sodium related band found in solution is also observed as a broad shoulder in the spectrum measured on the sample cured at room temperature. After increasing the curing temperatures the shoulder disappeared. Since the sodium related band decreased with increasing curing temperature it is an indication that new bondings between silica species are formed (polymerisation process) since the sodium content incorporated in the silica layer decreased. Furthermore, additional bands at high wavenumbers ( $1289\text{ cm}^{-1}$ ) appeared in the spectra on the aluminium substrate but not in solution. An increase of this intensity with increasing curing time is observed, revealing an increase of the cross-linking due to the heat-treatment. Unfortunately the Raman vibration at  $1289\text{ cm}^{-1}$  could not be attributed to specific silica bondings due to missing references in the literature.

### V.3 Morphology of the aluminium surface after deposition of sodium silicate

A closer look at the components being present in the silicate passivation layer deposited on a metal surface is done by FE-SEM/EDS. For this purpose the standard pre-treatment conditions given in Chapter III were modified in accordance to the conditions listed in Table III-3. Every sample is displayed in low magnification (2000x) and high magnification (20000x).

Figure V.3-1 (A and B) shows the top view of the aluminium substrates after alkaline cleaning without a silica coating. The surface looks very rough and reveals pitting, due to the attack of the alkaline cleaner (pH = 12.5). Figure V.3-1 (C and D) shows the conditions after the deposition of the silica layer. The application is performed by immersing the substrate in a 1.1 M  $\text{SiO}_2$  solution and curing at room temperature for

24 hours. On the low magnification (C) a thin, not transparent silica deposit can be observed. Furthermore, higher magnifications reveal some precipitates on the surface.

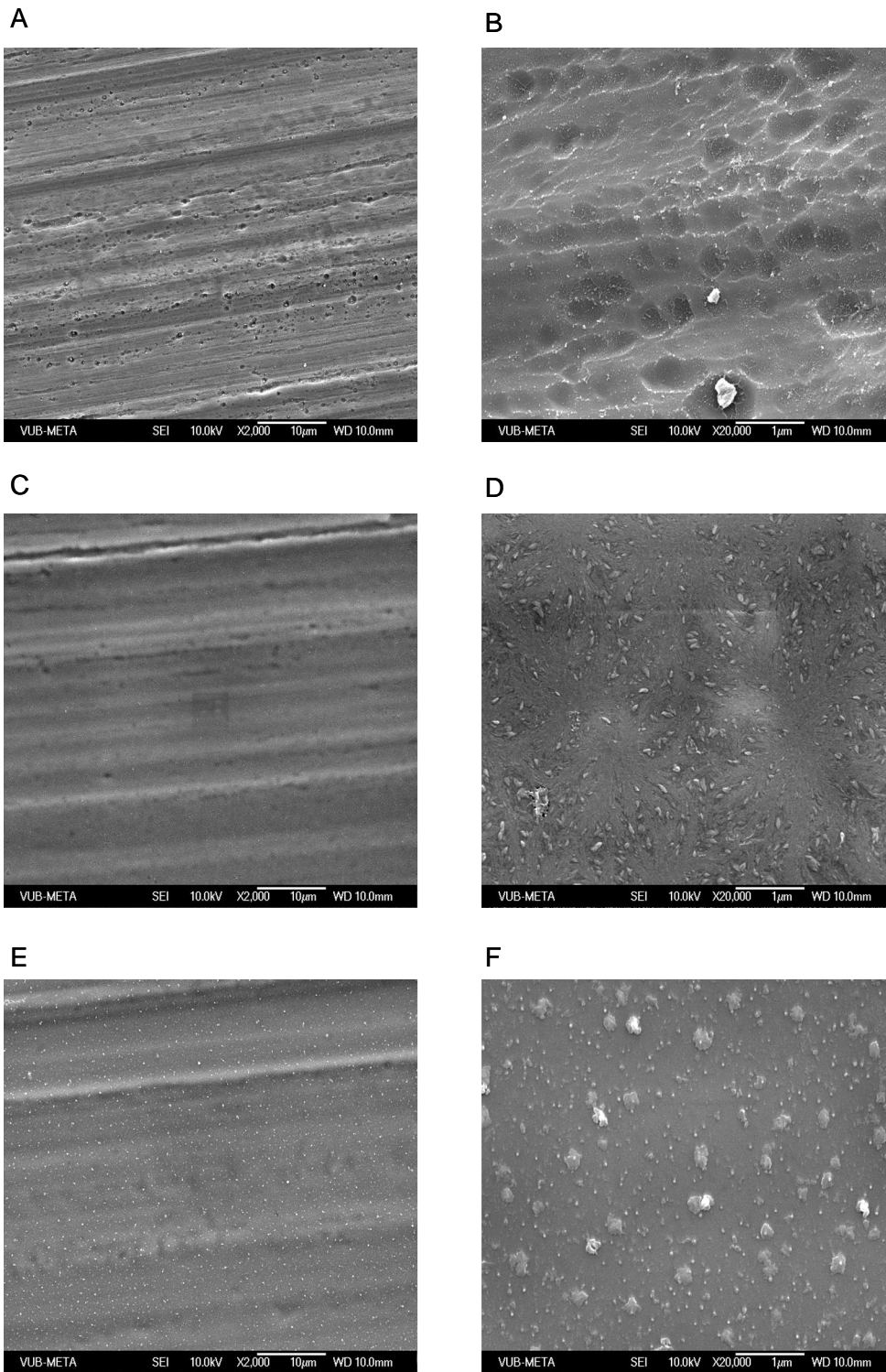


**Figure V.3-1:** Top view of aluminium substrates after alkaline cleaning (A, B) and additional deposition of a silica layer, cured at room temperature (C, D) and at 150°C (E, F).

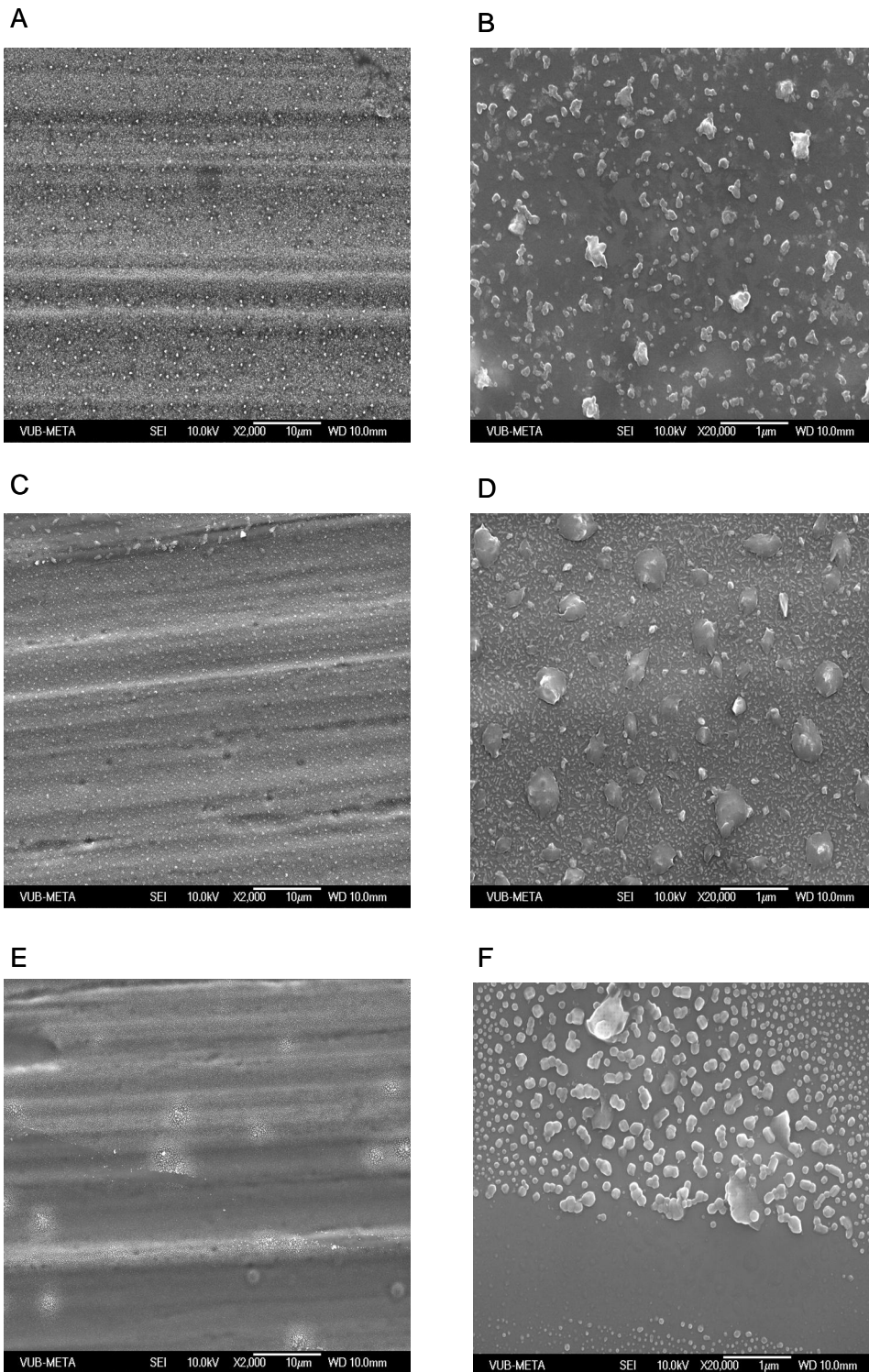
Figure V.3-1 (E and F) shows the morphology of the silica layer after curing for 30 min at 150°C. At low magnification (E) some white spots can be observed on the surface. At high magnification (F) different precipitates can be distinguished in shape and size. In Table V-3 the significant details are summarized. Figure V.3-2 shows the layer after different curing temperatures. Figure V.3-2 (A and B) images the layer after curing for 30 min at 50°C. At low magnification (A) precipitates can be seen on the surface, which are different in shape and size as seen at high magnification (B). After curing for 30 min at 100°C (Figure V.3-2 (C and D)) similar conditions can be observed at low magnification (C). However, considering the precipitates at higher magnification (D) the size of the particles increased in comparison to the lower curing temperatures. At curing temperatures of 250°C (Figure V.3-2 (E and F)) the lower magnification (E) shows a different morphology. There are areas without particles and areas with a higher concentration of particles, which is shown in detail in the higher magnification (F). The significant properties of the morphology after various curing temperatures are summarized in Table V-3.

**Table V-3:** Morphology of the surface after various curing temperatures.

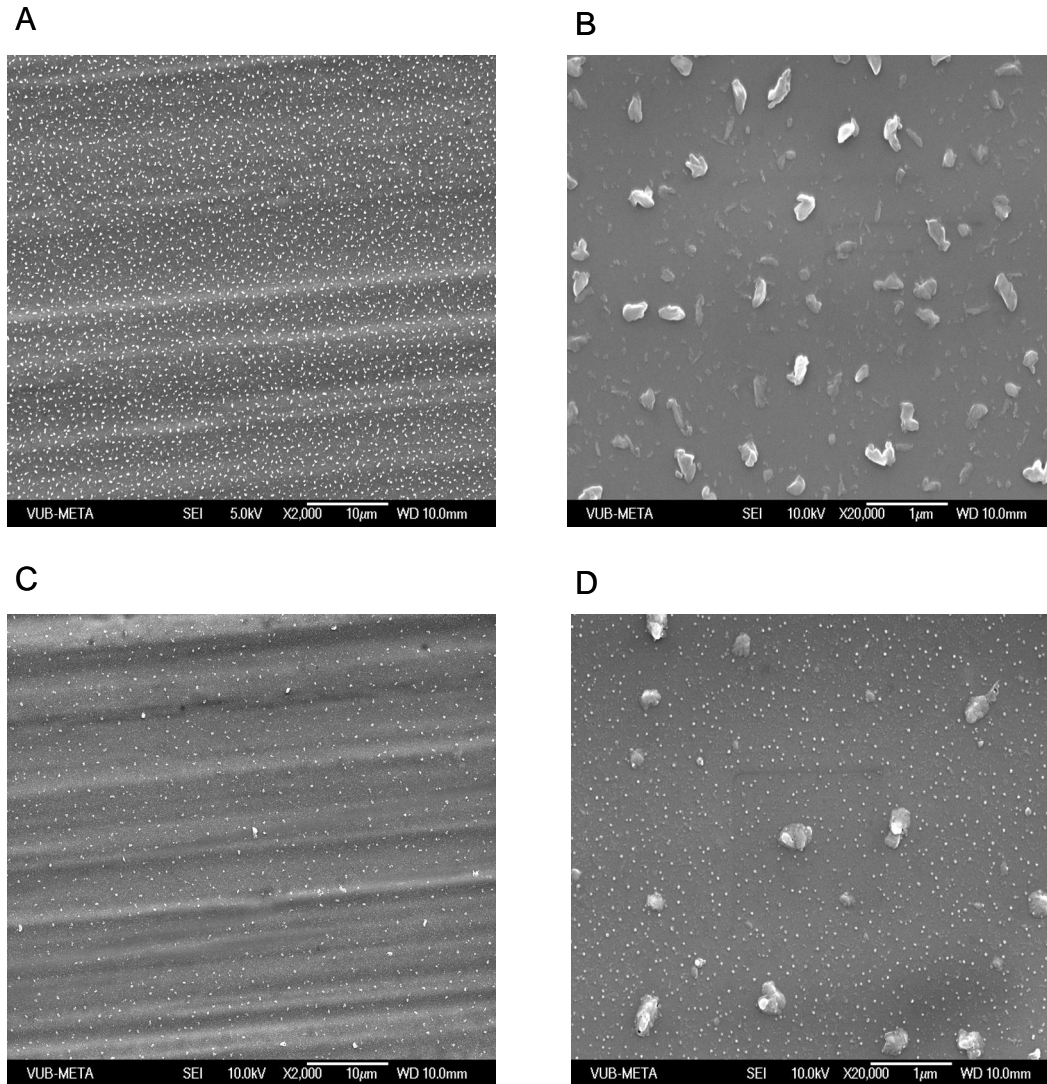
Curing temperature	morphology of the surface
Alkaline cleaned ( <u>Figure V.3-1</u> A,B)	pits
Room temperature ( <u>Figure V.3-1</u> C, D)	Rough, small precipitates
50°C ( <u>Figure V.3-2</u> A, B)	smooth, size of precipitates: up to 400 nm
100°C ( <u>Figure V.3-2</u> , C, D)	smooth, size of precipitates: up to 500 nm
150°C ( <u>Figure V.3-1</u> E, F)	smooth, size of precipitates: up to 300 nm
250°C ( <u>Figure V.3-2</u> E, F)	smooth, size of precipitates: up to 600 nm

Figure V.3-3 (A-D) shows the silicate layer after different curing times (between 5 min and 60 min). Figure V.3-3 (A and B) shows the conditions after a curing time of 5 min at 150°C. The low magnification (A) shows a high density of particles equally distributed on the surface which can be seen more in detail at higher magnification (B). In

contradiction to that the sample cured for 60 min at 150°C shows in low magnification (C) less density of particles on the surface.



**Figure V.3-2:** Top view of an aluminium substrate after deposition of a silicate layer, cured for 30 min at 50°C (A, B), 100°C (C, D) and 250°C (E, F).



**Figure V.3-3:** Top view of a silicate passivation layer, deposited on an aluminium substrate after various curing times; 5 min at 150°C (A, B) and 60 min at 150°C (C, D).

Finally at higher magnification (D) it is shown that the average size of the particles decreased in comparison to the curing time of 5 min. The significant properties of the morphology after various curing times are summarized in Table V-4.

**Table V-4:** Morphology of the surface after various curing times.

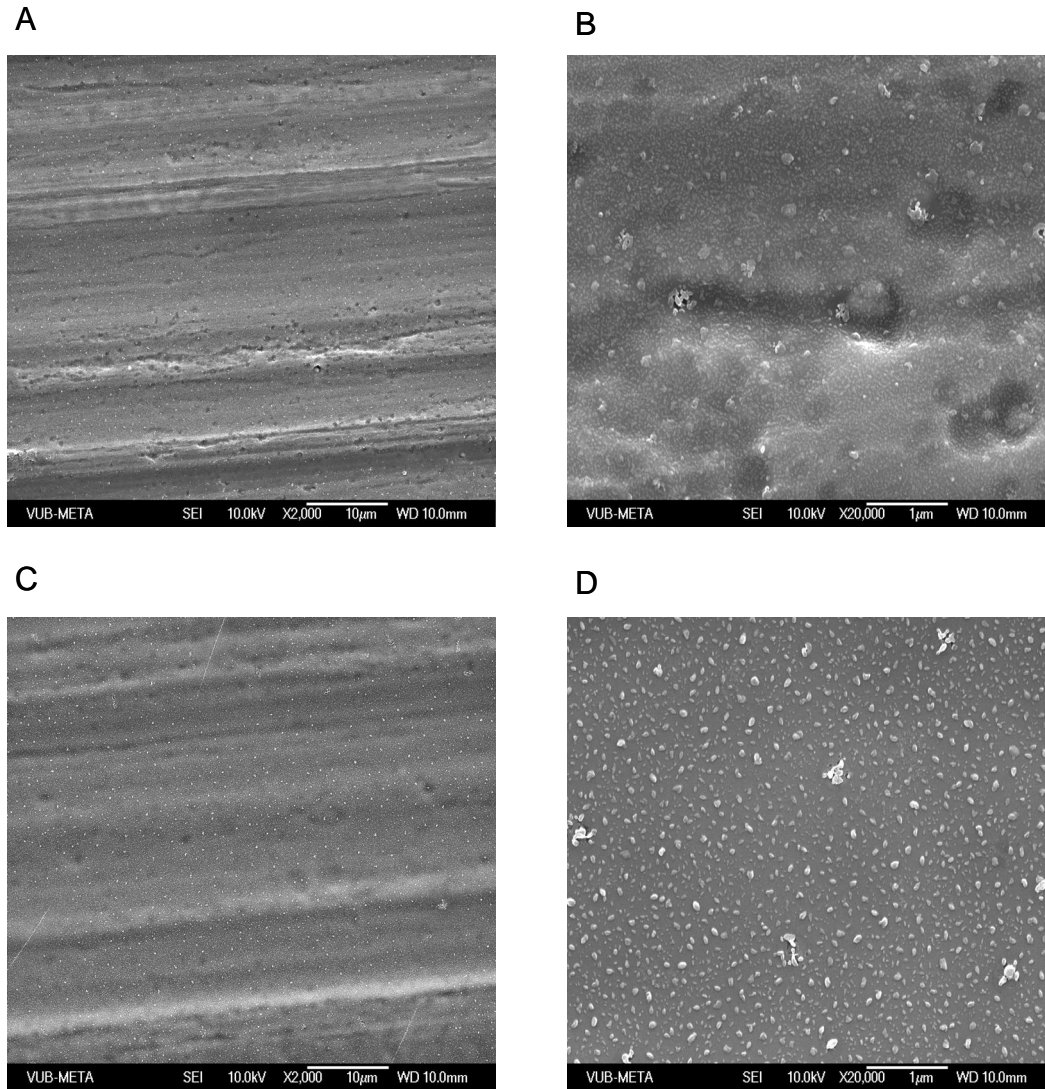
Curing time	morphology of the surface
5 min ( <u>Figure V.3-3 A, B</u> )	smooth, size of precipitates: up to 300 nm
30 min ( <u>Figure V.3-1 E, F</u> )	smooth, size of precipitates: up to 300 nm
60 min ( <u>Figure V.3-3, C, D</u> )	smooth, size of precipitates: up to 400 nm

Figure V.3-4 shows the silicate layer deposited with various bath concentrations. On the surface, coated with a 0.2 m SiO<sub>2</sub> solution the pits, caused during the alkaline cleaning, are still visible in the low magnification (A). With high magnification (B) a very thin layer can be observed. In comparison to that, the morphology of the surface deposited with a 2.0 m SiO<sub>2</sub> bath concentration is very smooth, since the pits from the alkaline cleaning are completely covered by the silicate layer. The significant properties of the morphology after various bath concentrations are summarized in Table V-5.

**Table V-5:** Morphology of the surface after various bath concentrations.

Bath concentration	morphology of the surface
0.2 m ( <u>Figure V.3-4 A, B</u> )	rough, size of precipitates: up to 200 nm
1.1 m ( <u>Figure V.3-1 E, F</u> )	smooth, size of precipitates: up to 300 nm
2.0 m ( <u>Figure V.3-3, C, D</u> )	smooth, size of precipitates: up to 200 nm

In Figure V.3-5 the influence of the dipping time is shown. For this purpose the aluminium samples are dipped for 10 sec (A and B) and 600 sec (C and D) in a 1.1 m SiO<sub>2</sub> solution. In the low magnification (A and C) the morphology of both conditions looks very similar. Only in higher magnifications (B and D) the difference is seen in a slightly higher average size of the particles with the samples immersed for 600 sec in the silicate solution. The significant properties of the morphology after various dipping times are summarized in Table V-6.



**Figure V.3-4:** Top view of an aluminium substrate after immersion in a 0.2 m  $\text{SiO}_2$  (A, B) and 2.0 m (C and D)  $\text{SiO}_2$  bath concentration.

**Table V-6:** Morphology of the surface after various dipping times.

Dipping time	morphology of the surface
10 sec (Figure V.3-3 A, B)	smooth, size of precipitates: up to 800 nm
60 sec (Figure V.3-1 E, F)	smooth, size of precipitates: up to 300 nm
600 sec (Figure V.3-3, C, D)	smooth, size of precipitates: up to 1 $\mu\text{m}$

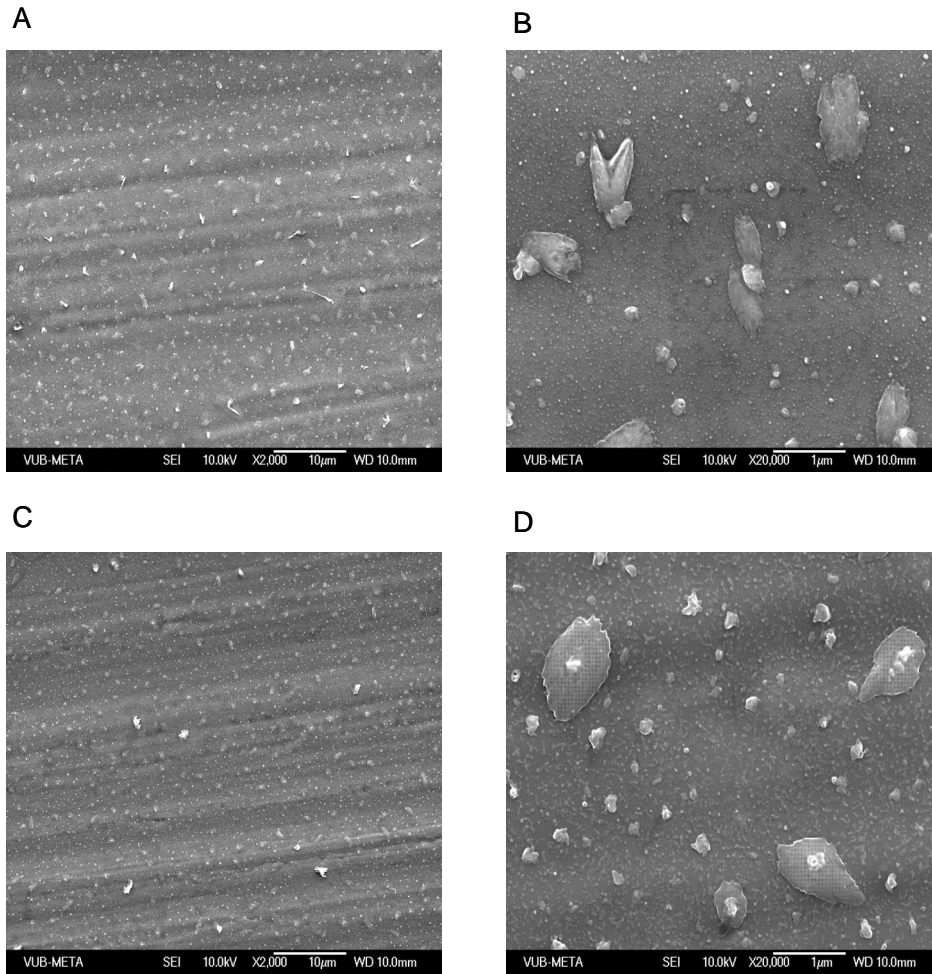


**Figure V.3-5:** Top view of an aluminium substrate after 10 sec and 600 sec immersion in a 1.1 M SiO<sub>2</sub> bath concentration.

—  
Figure V.3-6 presents a schematic illustration of the deposition process of the silica passivation layer on aluminium.

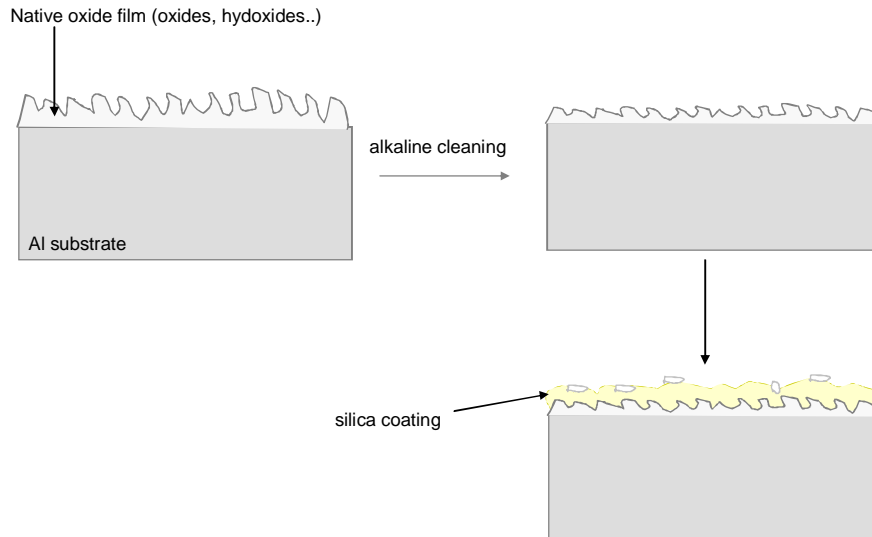


**Figure V.3-6:** Schematic illustration of the deposition process.

#### V.4 Thickness of the passivation layer

In order to investigate the effect of the deposition conditions (bath concentrations and dipping times) on the thickness of the layer, cross-sections were analysed with FE-SEM. Prior to the FE-SEM analysis the samples are immersed in liquid nitrogen for 30 min and bent over a razor blade to ensure a sharp cut.

##### Influence of the bath concentration:

Figure V.4-1 (A-C) shows FE-SEM images of the cross-sections of aluminium substrates after immersion in various bath concentrations. A uniform and homogeneous layer with a thickness around 160 nm was deposited after immersion in a 0.2 m SiO<sub>2</sub> bath concentration (A). After immersion in a 1.1 m SiO<sub>2</sub> bath concentration (B), the thickness of the layer is around 700 nm. Due to the increasing thickness of the layer a sharp cut was possible. Never the less the FE-SEM image showed that there is still a remaining part of the layer stuck to the surface, what is seen in the smooth structure of the surface. Considering this, the layer thickness is assumed to be higher than the results received by FE-SEM analysis. Furthermore there is a deviation in the layer thickness depending on the area the measurement has been performed, due to the rough surface conditions.

Finally the layer thickness measured on the substrate coated with the 3.0 m SiO<sub>2</sub> concentration (C) is around 2.1 μm. Besides, the adhesion is very strong, since after bending there is still a remaining part of the layer stuck to the surface.

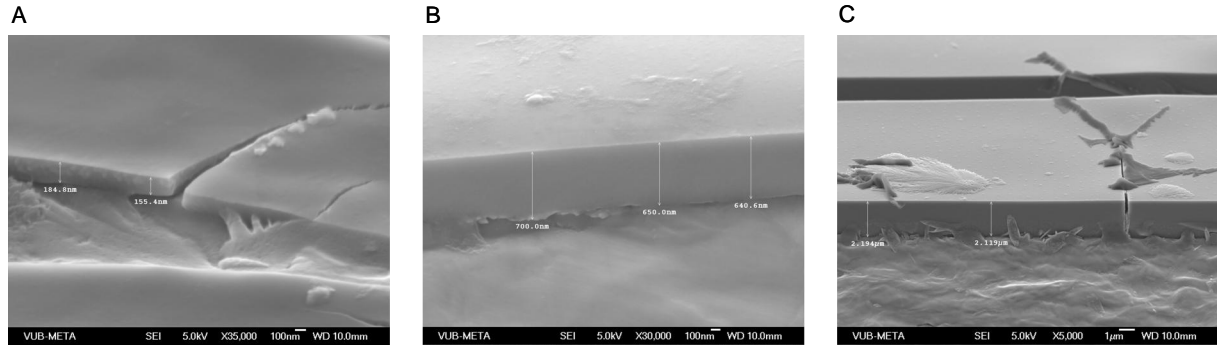


**Figure V.4-1:** Cross-sections of aluminium substrates immersed in 0.2 m (A), 1.1 m (B) and 3.0 m SiO<sub>2</sub> solution.

#### Influence of the dipping time:

Figure V.4-2 shows the cross-sections of aluminium substrates immersed for 10 sec (A) and 600 sec (B) in a 1.1 m silica solution. Increasing the dipping time showed no significant influence on the layer thickness. The thickness measured by FE-SEM analysis is around 520 nm for a dipping time of 10 sec (B) in comparison to the thickness of around 400 nm found on the sample with a dipping time of 600 sec (B). The deviation of the thickness between both samples is probably caused by the rough sample conditions and not due to the deposition conditions.

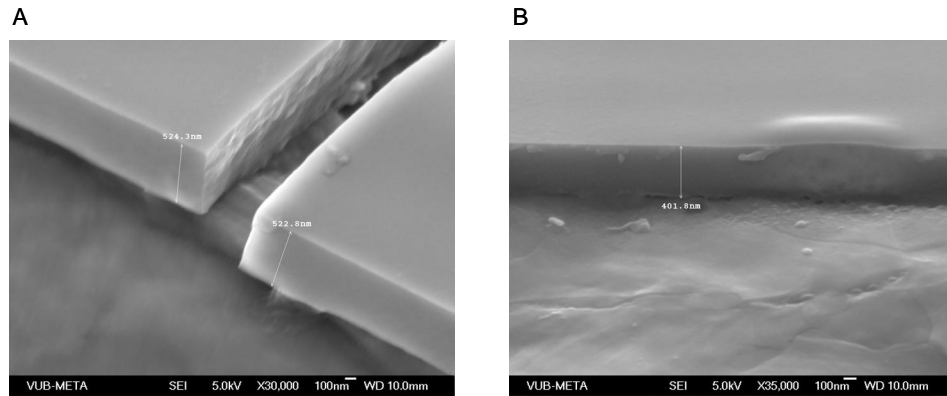


**Figure V.4-2:** Cross-sections of aluminium substrate immersed for 10 sec and 600 sec in a 1.1 m SiO<sub>2</sub> solution.

A schematic illustration of the effect of the deposition conditions on the layer thickness is given in

**Figure V.4-3.**

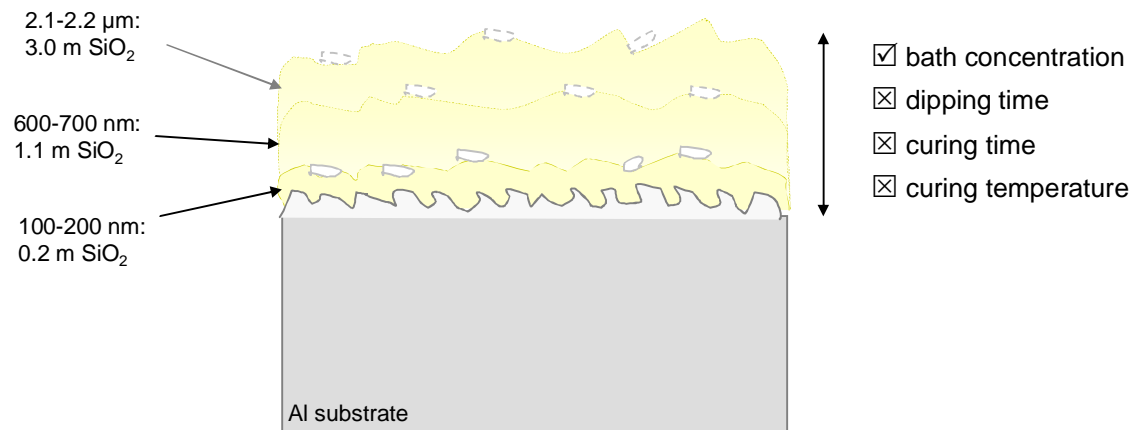


**Figure V.4-3:** Schematic illustration of the effect of the deposition conditions on the layer thickness.

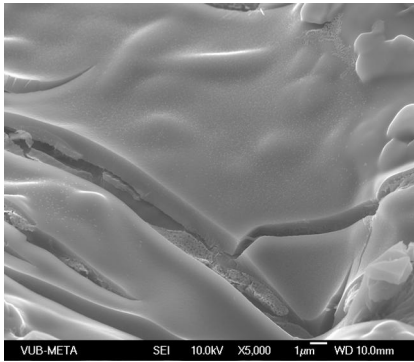
## V.5 Mechanism of the deposition

In order to follow the evolution of the potential transient during the deposition process the OCP is measured during immersion in the aqueous silicate solution. Furthermore the deposition is performed on pure aluminium substrates and on aluminium brazing sheets (AA4045/3003/4045) to study the influence of intermetallic phases.

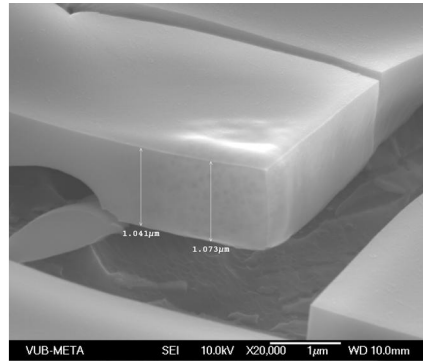
Influence of the substrates on the deposition process:

Figure V.5-1 shows FE-SEM images of aluminium brazing sheets coated with a silicate layer (A and B) and pure aluminium (C and D) coated under the same conditions. To gain insight in the morphology of the layer, cross-sections are prepared. For this purpose the samples are immersed in liquid nitrogen for 30 min to ensure a sharp cut of the layer during bending over a razor blade. The optical observation of the coating, deposited on the brazing sheet, reveals a dense and homogeneous deposit. In low magnification (A) the silica layer reproduces the surface morphology of the underlying aluminium substrate, indicating the uniformity of the coating. In high magnification (B) the layer thickness is calculated to approximately 1  $\mu\text{m}$ . Similar conditions are observed on the aluminium substrate. A Low magnification (C) of the cross-section reveals the dense and homogeneous structure of the deposit and high magnification (D) shows a layer thickness around 940 nm.

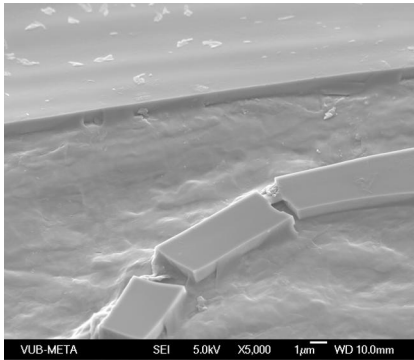
A



B



C



D

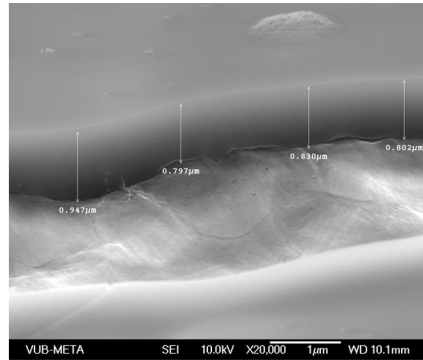


**Figure V.5-1:** Different magnifications of a silica coating deposited on AA4045/3003/4045 (A and B) and on pure aluminium (C and D).

## V.6 In-situ OCP measurements

Figure V.6-1 shows the potential transients recorded on aluminium brazing sheets and pure aluminium in various bath concentrations. After immersion of AA4045/3003/4045 in the aqueous silicate solution the potential transients decreased within the first five seconds to  $-0.86$  V for the  $2.0$  m  $\text{SiO}_2$  bath concentration and to  $-0.9$  V for  $0.2$  m  $\text{SiO}_2$  bath concentration. After that, the potential transients increased to about  $-0.73$  V for the  $2.0$  m  $\text{SiO}_2$  bath concentration (10 sec immersion time) and to  $-0.80$  V for  $0.2$  m  $\text{SiO}_2$  bath concentration (20 sec immersion time). The potential transients of Al 99,99% decreased during the first 10 sec of immersion time to  $-0.83$  V ( $2.0$  n  $\text{SiO}_2$  bath concentration) and to  $-0.97$  V ( $0.2$  m  $\text{SiO}_2$  bath concentration). After that, the OCP slightly increased before it reached stable values.

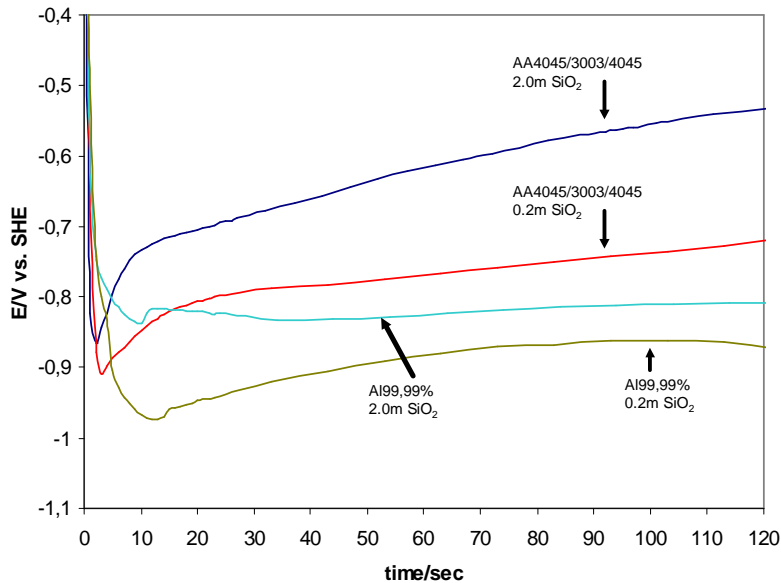


**Figure V.6-1:** In-situ OCP measurements in aqueous sodium silicate solutions.

The initial decrease of the OCP can be attributed to the dissolution of the native oxide layer on the surface due to the alkaline environment of the aqueous sodium silicate solution. The following relative stable behaviour of the OCP of Al99,99% substrates immersed in 0.2 and 2.0 m SiO<sub>2</sub> bath concentration indicates a physical adsorption of the silica species without any electrochemical reactions. Although the aluminium brazing sheets show an increase of the OCP after the initial decrease, this behaviour can not be attributed to an electrochemical reaction of the silica species during the deposition on the substrate. The increase can be explained by the redox behaviour of the aluminium surface in the alkaline environment. As reported by Tada et al.<sup>49</sup> the electrolyte penetrates in the silica layer, resulting in a contact between substrate and electrolyte. Due to that, the OCP measurements are influence by the electrochemical reactions occurring during the re-passivation of the native oxide layer in the alkaline silica solution. This behaviour is confirm with the strong increase of the OCP during the first 10 to 20 sec since during these conditions the silica layer is still growing and a significant lesser increase of the potential is seen after the layer reached the final thickness (20 sec.).

## V.7 Discussion

In order to gain information about the deposition conditions of the silica layer, morphological investigations and electrochemical measurements have been performed. Visual observations of the surface after the deposition of the silica layer by various deposition conditions (different bath concentrations, curing times, curing temperatures and dipping times) showed no significant changes. Though FE-SEM images (20000x) of the coated surface revealed particles of different size and shape due to different deposition conditions, no particular correlation between the surface conditions and the deposition conditions was found. In cross-sections the layer thickness was determined, increasing with increasing SiO<sub>2</sub> bath concentration. In contradiction, the dipping time had no influence on the layer thickness comparable to the curing time and temperature (not shown here). The mechanism of the deposition was studied by using different aluminium substrates. As shown in Chapter IV the brazing sheets reveal different intermetallic phases (containing iron, silicon, manganese and aluminium) on the surface and flux

particles used during the brazing process. Since these intermetallic phases act as cathodes or anodes (depending on their counterpart) an influence on the deposition conditions is expected, if the deposition process is electrochemically driven. For this purpose the morphology of the deposit was investigated by FE-SEM with focus on the influence of intermetallic phases as well as electrochemical measurements were performed. The intermetallic phases showed no significant influence on the structure of the deposit, indicating that the deposition occurs due to physical adsorption of the silicate ions. The in-situ OCP measurements confirmed these assumptions. The initial decrease of the OCP can be attributed to removal of the native oxide layer on the alloy surface due to the alkaline environment in the silicate solution. This initial increase is also described for Zr/Ti based systems<sup>55</sup>. However this electrochemically driven system reveals after the initial decrease an increase indicating the deposition of Zr and Ti containing oxide components. Although the aluminium brazing sheets reveal a similar behaviour in the potential transients compared to the Zr/Ti systems, a physical adsorption of the silica layer is proposed. The increase of the OCP is explained by the penetration of the electrolyte in the coating, resulting in an influence of the aluminium re-passivation reaction on the OCP.

### V.8 Constitution of the silicate passivation layer

In order to gain chemical information on the silica passivation layer, XPS and EDS analysis have been performed. In addition to that, depth profiling measurements by erosion of the surface layer by layer by ion sputtering, is applied to gain an elemental analysis as well as a chemical states analysis from to surface to the bulk material.

The main components expected are silicon, oxygen and sodium. Hence, the focus is on the evolution of the Si/Na, O/Si and O/Na ratios found in the different layers of the depth profiling, revealing information about the constitution of the layer. Furthermore the influence of changing the deposition conditions on the ratios between Si, O, and Na were investigated by EDS measurements.

### V.8.1 XPS analysis

The XPS survey scan of an aluminium surface, after immersion in a silicate solution, containing 1.1 m SiO<sub>2</sub>, is displayed in [Figure V.8-1](#). The presence of the silica layer at the surface of the sample has been confirmed by the detection of Si 2s, Si 2p, and Na 1s peaks in the XPS spectra. The atomic concentrations found on the surface are listed in [Table V-7](#).

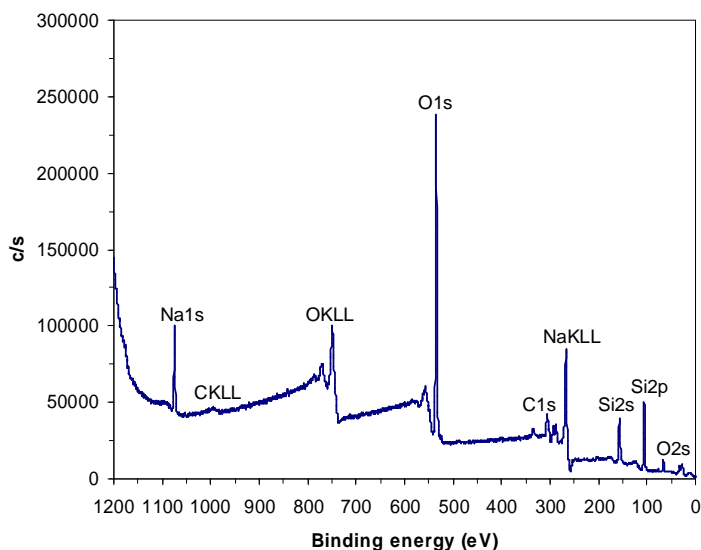


**Figure V.8-1:** XPS survey spectra of an aluminium surface coated with 1.1 m SiO<sub>2</sub>.

**Table V-7:** Atomic concentrations of the elements found on the surface of the silica layer.

C1s	O1s	Na1s	Al2p	Si2p
14.61	55.36	8.63	0.00	21.39

[Figure V.8-2](#) presents the spectrum of a XPS depth profiling within a silica coating, deposited on an aluminium substrate. The atomic concentrations after various depths of the XPS profiling are shown in [Table V-8](#). Within the first 20 min of sputtering C and Na decreased to a minimum, whereas Si and O increased to their maximum atomic concentrations. After a sputtering time of around 135 min, Si and O decreased and at the same time Na and Al increased. Finally after a sputtering time of 178 min Na decreased

again, indicating that the interface region between the layer and the bulk material is reached.

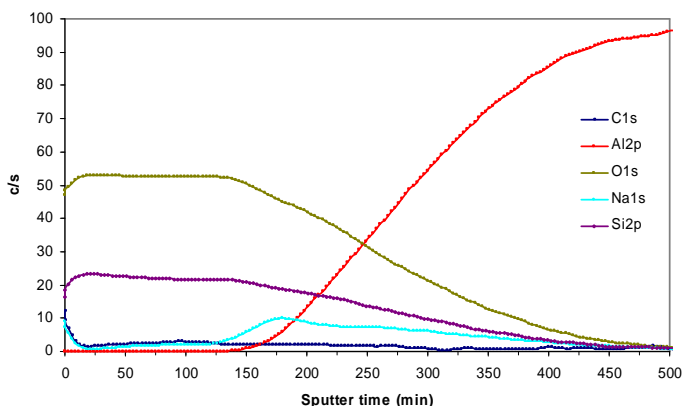


**Figure V.8-2:** XPS depth profiles performed on aluminium substrates coated with a silicate layer.

**Table V-8:** Atomic concentrations of the elements detected at various depths of the XPS profile.

Sputter time (min)	C (at%)	O (at%)	Si (at%)	Na (at%)	Al (at%)
1	13.6	55.7	21.5	9.26	0.0
20	1.9	64.7	32.7	0.6	0.1
178	1.1	54.0	25.2	12.7	7.0
240	0.4	40.8	21.0	8.8	29.0

The spectra in [Figure V.8-3](#) reflect the evolution of the different elements from the surface to the bulk material. Si 2p and O 1s reveal have the highest concentrations in the outer parts of the surface layer (within the first 30 min of sputtering time). They start decreasing as soon as the interface region is reached, shown with increasing intensity of the Al 2p peak. A different behaviour is found with Na 1s. On the surface and in the area close to the surface this element is found in high concentrations (within a sputtering time of 20 min). Afterwards it drops to a minimum and increases again to its highest concentrations in the interface, before it drops again to a minimum.

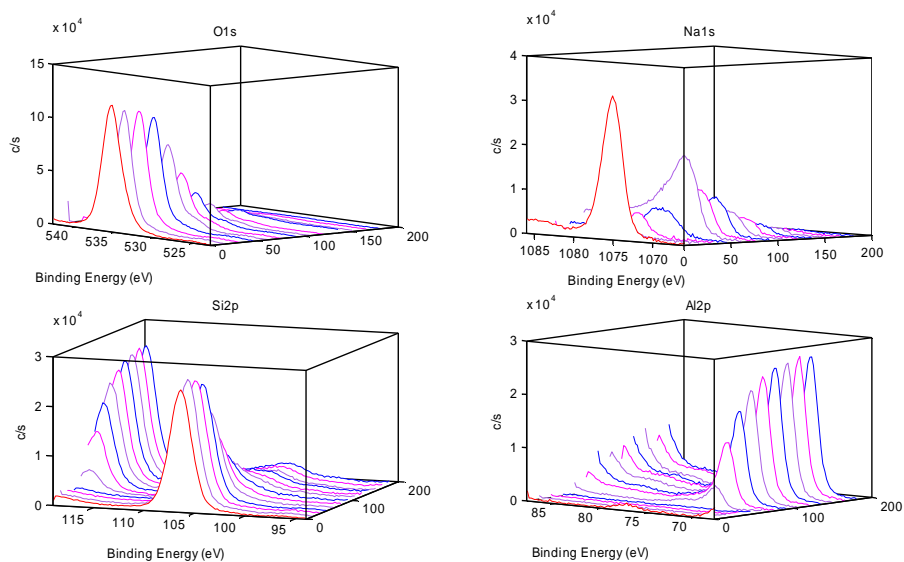


**Figure V.8-3:** Evolution of O 1s, Na 1s, Si 2p and Al 2p during XPS profiling.

Considering the elemental analysis performed at various depths of the XPS profiling, it is seen that the change of the atomic concentrations of Si, O and Na are not linear in the various depths, indication a non-uniform layer from the surface to the bulk material. The ratios between the different components (Na, Si and O) for various depths are calculated and listed in [Table V-8](#). The chosen depths are due to the significant changes of the atomic concentrations, revealed by the XPS profiling. The ratio between O and Si is, among slightly deviations ( $O/Si = 1.9 - 2.6$ ), during the entire depth profiling constant. In contradiction to that, the ratios of O/Na and Si/Na showed a high deviation. Within the first 20 min of sputtering, the Si/Na and O/Na ratios showed a strong increase, since the sodium concentration dropped to a minimum. By continuation of the depth profiling, the Si/Na and O/Na ratios decreased again and finally showed ratios as the one found at the beginning. The progress of the ratios is displayed in [Figure V.8-4](#).

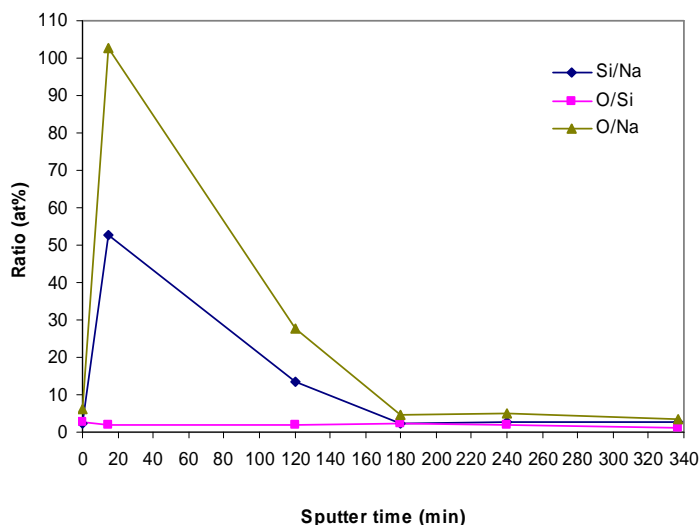


**Figure V.8-4:** Evolution of the ratios between O/Si, Si/Na and O/Na during the XPS depth profile

## V.8.2 Structure of the silica layer

In order to investigate the structure of the layer, the binding energies of Si 2p, Na 1s and O 1s are studied concerning the chemical shift and the shape of the peaks during the depth profiling.

In [Figure V.8-5](#) the evolution of Al 2p (A), Si 2p (B), Na 1s (C) and O 1s intensities are displayed. The binding energies show a shift due to a charging problem, which was not corrected since the aim was to show the evolution of the peak in the different depths of the profile independent of the absolute value of the binding energy. By reaching the interface, the aluminium peak (A) appeared and the intensity increased till the bulk material of the substrate is reached (after around 300 min of sputtering time). The binding energies of Al 2p are not strongly shifting within the layer. However, since the peak is very broad, an overlap of different types of bonding is expected. The Si 2p peak (B) decreased in intensity during the depth profiling till it disappears as soon as the bulk material is reached. From the surface to the bulk material the binding energies of silicon shifted to lower values. The broad shape of the peak indicates an overlay of at least two different kinds of bondings. The spectra of the Na 1s peak (C) reveal high intensities at the beginning, before they drop to a minimum and increase again in the interface. At the same time the binding energies shifted to lower values between the surface and the bulk

material. The shape of the peak is very broad, indicating an overlay of different types of bondings. The intensity of the spectra of O1s (D) showed a decrease in the various depths as well as a slight shift to higher binding energies after a sputtering time of 20 min. After 178 min and 240 min the peaks shift again to lower binding energies. The shape of the O1s peak is very broad, indicating different types of bondings.

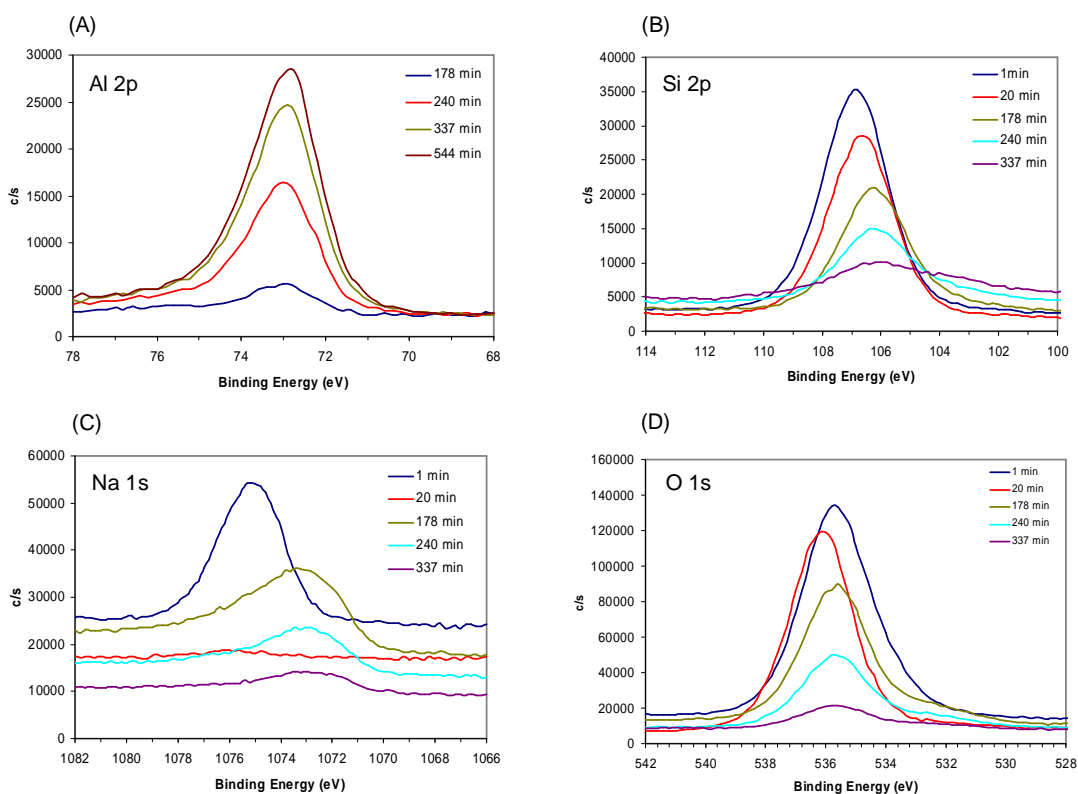


**Figure V.8-5:** Al 2p (A), Si 2p (B), Na 1s (C) and O 1s spectra at various depths of the XPS profile.

Considering the results gained by the XPS depth profiling, the layer can be divided in three areas, revealing changes in the structure:

- interface between layer and the aluminium substrate
- the bulk of the layer
- the surface of the layer

The interface between the layer and the aluminium substrate:

In order to receive chemical information on the interface between the layer and the substrate, the binding energies of Si, O, Na and Al are evaluated and compared to literature values. In

Figure V.8-6 the high resolution spectra of the different elements present in the interface are displayed. Due to the absence of carbon in this area of the layer, the chemical shift of the peaks is corrected to  $\text{Al}_2\text{O}_3$  (74.4 eV). The simulation of the Al 2p region (A) has been performed using two components: the oxide (Al 2p-2) and the hydroxide (Al 2p-1) form. The Si 2p peak has been fitted according to silica bonding occurring in polymeric form (Si 2p-1) and in monomeric form (Si 2p-2). The Na 1s peak (C) is fitted to possible combinations with O, Si and/or Al found at the NIST database<sup>56</sup>, since it is not clear in which form sodium is present in the layer. Possible compounds are for instance  $\text{Na}[\text{AlSi}_3\text{O}_8]$  (Na 1s-1),  $\text{Na}[\text{AlSi}_2\text{O}_6]$  (Na 1s-1) and  $\text{Na}_2\text{O}$  (Na 1s-2). Finally the O 1s peak (D) is fitted to silica bonding (O 1s-1) and aluminium oxide/hydroxide (O 1s-2).

According to literature data<sup>56</sup> different compounds are found in the interface:

Aluminium oxide and hydroxide due to the (Al 2p-1), (Al 2p-2) and (O 1s-2) peaks. The (Si 2p-2) binding energy at 102 eV is attributed to disilicate, since a common aluminium disilicate mineral, the kaolinite, has a binding energy of 102.45 eV, which is in good accordance with the energy found for the silica layer. Furthermore the shift to higher energies in (Si 2p-1) as well as in (O 1s-1) is related to polymerized silicates. Comparing the O/Si ratio of 2.2 (Figure V.8-4) with representative literature data<sup>47</sup>, the silica structure is attributed to the framework (2.0) and to the sheet modification (2.5), indicating that the real structure is a combination between sheet and framework. More difficult is the attribution of the sodium peaks to possible compounds. In accordance to NIST database<sup>56</sup> different compounds (including Al, Si, O and Na) are possible in the area of the binding energy for (Na 1s-1) and (Na 1s-2): molecular sieve,  $\text{Na}[\text{AlSi}_3\text{O}_8]$ ,  $\text{Na}[\text{AlSi}_2\text{O}_6]$  and  $\text{Na}_2\text{O}$

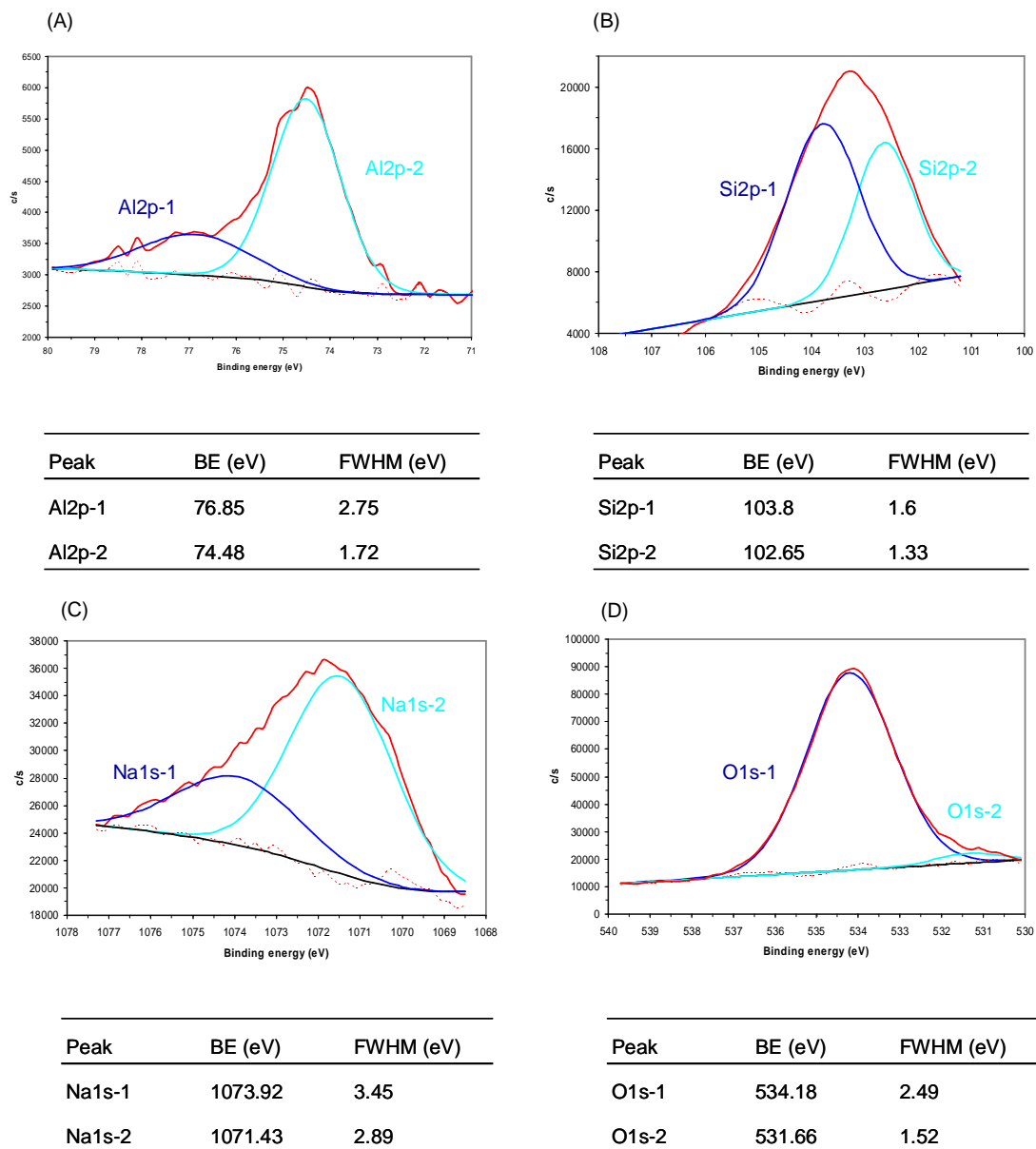


**Figure V.8-6:** High resolution spectra of the elements found in the silicate layer after 178 min of sputtering time: Al 2p (A), Si 2p (B), Na 1s (C), O 1s (D).

Figure V.8-7 presents a schematic illustration of the interface silica coating/aluminium substrate.

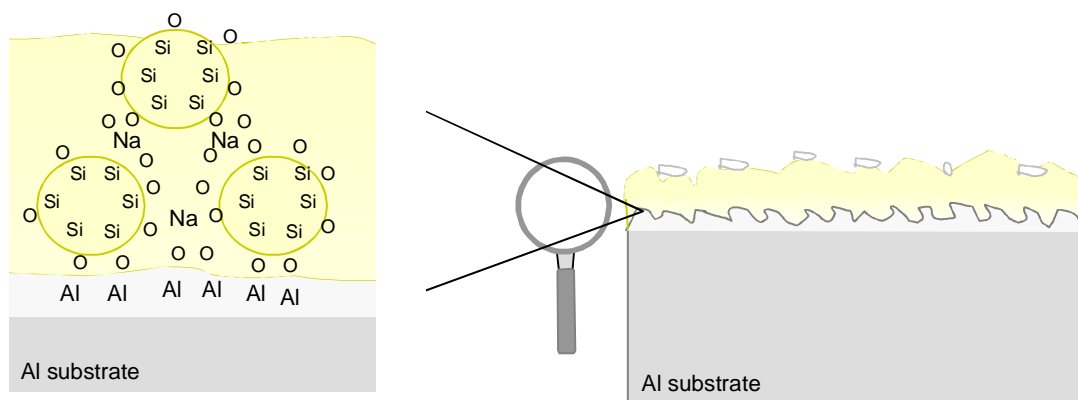


**Figure V.8-7:** Schematic illustration of the interface silica coating/aluminium substrate.

The bulk of the layer:

This area is characterized by a minimum of sodium and (almost) constant concentrations of Si and O. Considering the XPS depth profiling ([Figure V.8-2](#)) these conditions are found between 20 and 120 min of sputtering time. Due to the absence of aluminium and carbon in this area, the chemical shift of the Si 2p peak is corrected to the value found in literature<sup>56</sup> for SiO<sub>2</sub> (103.3 eV). [Figure V.8-8](#) shows the Si 2p peak after different sputtering times. The sputtering time of 20 min reflects the bulk conditions of the layer in comparison to the sputtering time of 178 min that are correlated to the interface. The Si 2p peak (found in the interface) shifted to higher intensities in the bulk of the layer. This is an indication for the transition of monomeric to polymeric species, since the covalency in the Si-O bonding decreases and thus an increase in the binding energies occurs. An explanation is given by the charge balance in the silicate lattice. Usually the Si-O bonding in silica is around 50/50 in its distribution of covalency/ionicity<sup>47</sup>. Substituting some silica with harder ions such as Na<sup>+</sup> increases the covalency of the Si-O bond, because the charge balance around oxygen has to be assured. Since the cation/Si ratio has its maximum in monomeric forms, the binding energy decreases as polymerization occurs. In the bulk of the layer the calculated O/Si ratio is around 2.0. Due to literature data<sup>45</sup>, the layer is correlated to a silica framework structure. [Figure V.8-9](#) presents a schematic illustration of the bulk of the silica layer.

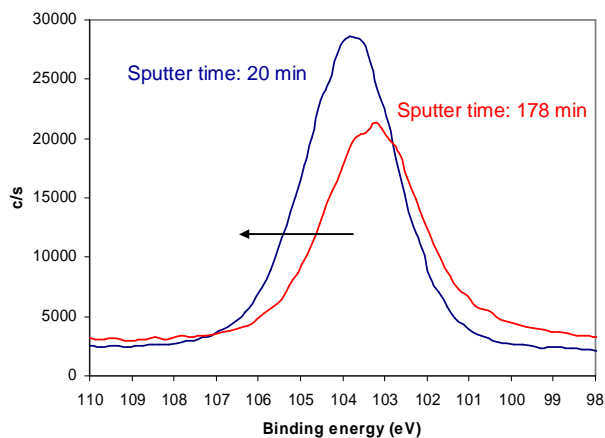


**Figure V.8-8:** Si2s peak after 20 min and 178 min of sputtering time.

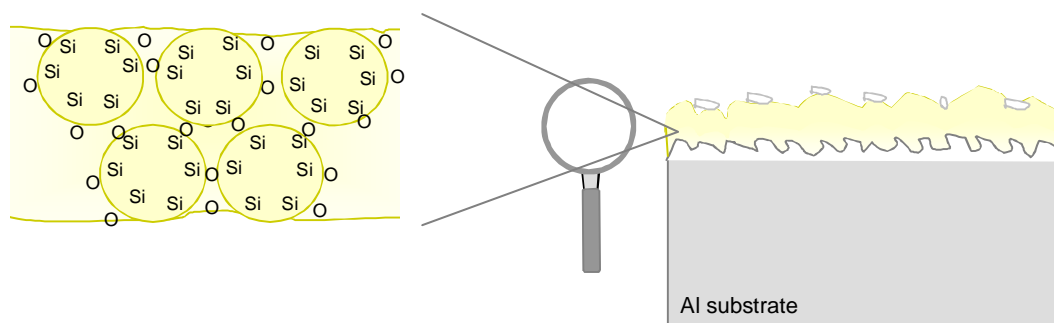


**Figure V.8-9:** Schematic illustration of the structure in the bulk of the layer.

### The surface area:

In order to determine the chemical state of the outer layer of the silica coating, the binding energy of the elements found in the survey scan (C, Si, Na and O) are analysed and compared to literature values. The measured peaks of these elements (charge corrected to C-C at 284.5 eV) are displayed in [Figure V.8-10](#). Since the samples are stored under laboratory atmosphere, also carbon was found in the sensitive XPS measurements, due to impurities. This impurity of the surface with carbon can be observed in the high resolution spectra of C 1s (A). The peak at a binding energy of

284.5 eV is attributed to carbon. However an additional peak at higher binding energies (289.0 eV) is detected, indicating a carboxyl bonding. The high resolution peak of O 1s (B) showed intensity at 532.0 eV, attributed to Si-O bondings. Furthermore the high resolution spectra of Na 1s showed a peak at 1071.5 eV. In accordance with possible compounds (including sodium, oxygen and carbon) found in the XPS database, the Na 1s peak can be attributed to  $\text{Na}_2\text{CO}_3$ . Finally the spectra of Si 2p revealed a peak with a binding energy of 103.0 eV, which is the typical area, where silicate bondings are observed.

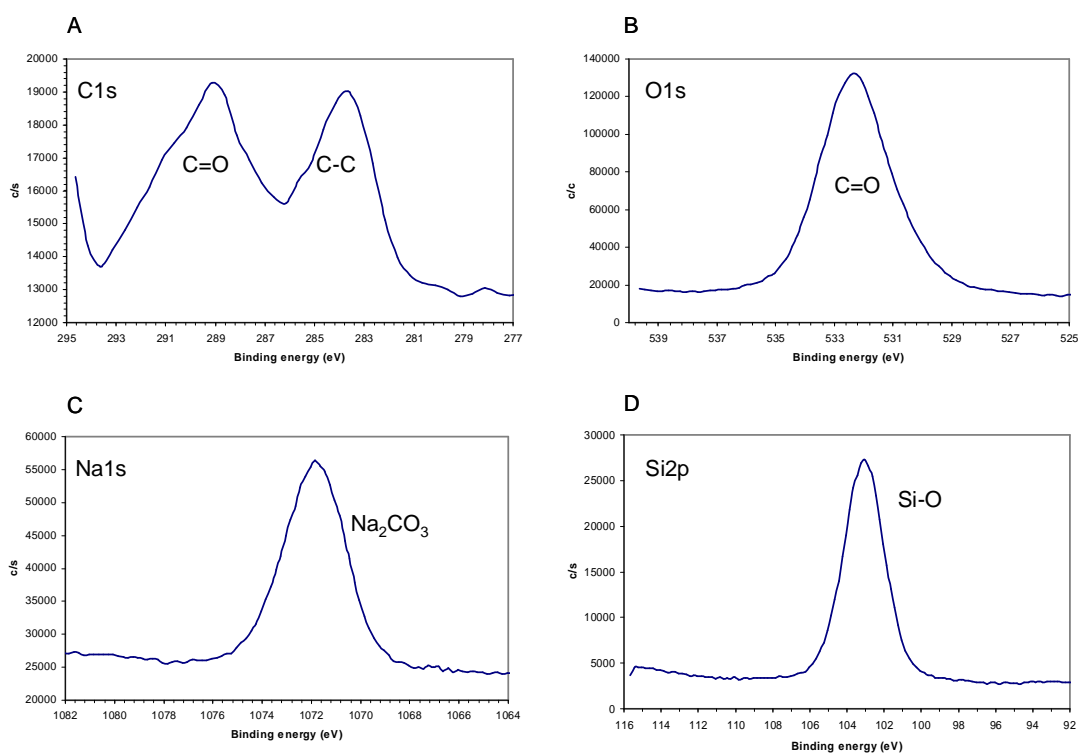


**Figure V.8-10:** XPS high resolution peaks of C 1s (A), O 1s (B), Na 1s (C) and Si 2p (D) on the surface of an aluminium substrate coated with a silicate layer (charge corrected to C-C at 284.5 eV).

Figure V.8-11 presents a schematic illustration of the surface conditions of the silica layer.

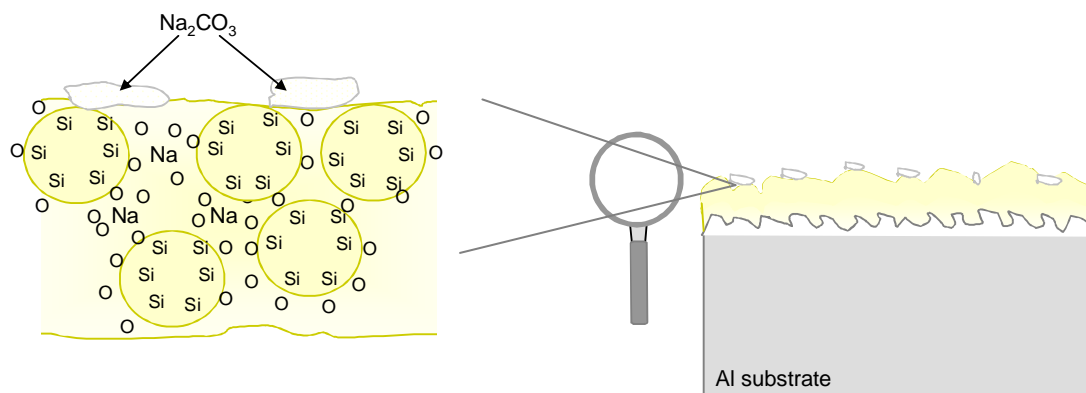


**Figure V.8-11:** Schematic illustration of the conditions at the surface of the layer.

## V.9 Uniformity of the silica passivation layer after deposition on aluminium substrates

To study the effect of the deposition conditions on the uniformity of the silica passivation layer, various bath concentrations, curing times, curing temperatures and dipping times have been analysed by means of EDS. The details of the deposition conditions are described in Chapter III. The FE-SEM images, showing the top view of the different deposition conditions are presented in [Figure V.3-1](#) to [Figure V.3-5](#).

To have reproducible conditions, the EDS analysis is performed on six different areas on each sample. Due to these six measurements, an average value is calculated, representative for the respective deposition condition. An example of this approach on one sample is given in [Figure V.9-1](#). The three plots show the different ratios between Si, Na and O. The dotted line represents the calculated average of the data points. In accordance to the calculated ratios by the XPS measurements, the ratio between oxygen and silicon is stable and shows hardly any deviation between the different data points. Slightly more deviation can be observed in the O/Na and O/Si ratios.

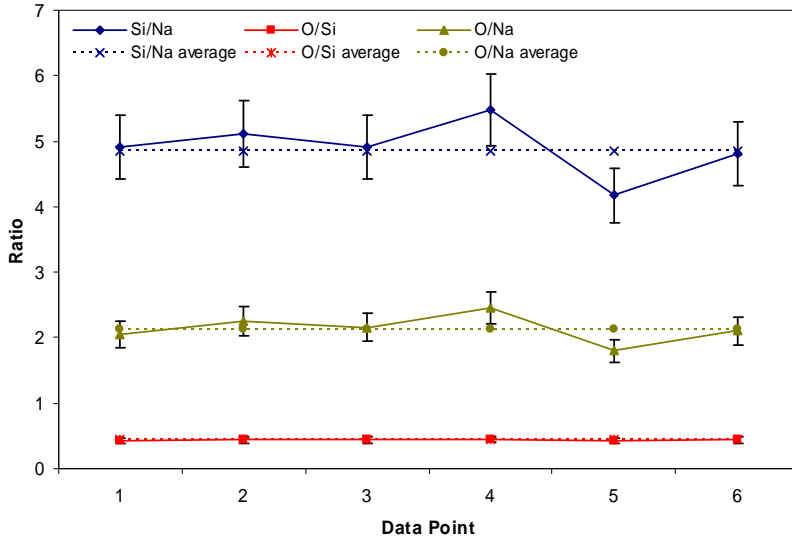


**Figure V.9-1:** Ratios between Si, O and Na found on one sample. The dotted lines show the average value of the six measurements.

In Figure V.9-2 the different deposition conditions are displayed. Figure V.9-2 (A) shows the evolution of the ratios between Si, Na and O by changing the bath concentrations (0.2 m, 1.1 m and 2.0 m  $\text{SiO}_2$ ) of the aqueous silicate solution. The ratios between O/Si and O/Na reveal no significant change by changing the bath concentrations. The Si/Na ratio shows a slight increase by increasing the bath concentration from 0.2 m to 1.1 m  $\text{SiO}_2$ . By a further increase to 2.0 m  $\text{SiO}_2$  the plot decreased again to the same values found for 0.2 m  $\text{SiO}_2$ .

The influence of the dipping time is shown in Figure V.9-2 (B). The Si/Na ratio decreased linear with increasing the dipping time from 10 sec to 60 sec and 600 sec. A similar behaviour shows the O/Na ratio, although the decrease of this ratio by increasing the dipping time is less significant. The ratio between O and Si is not affected by changing the dipping time.

The correlation between the curing time and the element ratios is displayed in Figure V.9-2 (C). By increasing the curing time from 0 min to 30 min, the Si/Na ratio increased and finally decreased again as the curing time is increased to 60 min. The O/Na ratio increased within the first 5 min of curing time and decreased again with a constant slope

by increasing the curing time to 60 min. The O/Si ratio shows no dependency on the curing time (Figure V.9-2 (C)).

Finally the effect of the curing time is displayed in Figure V.9-2 (D). The Si/Na ratio is increasing by increasing the curing temperature reached its maximum at 150°C and decreased again increasing the temperature to 250°C. Less significant is the change in the ratio of O/Na. Again an increase of the ratio is observed, having its maximum at around 150°C and decreased again by increasing the temperature to 250°C. The O/Si ratio shows no significant dependency on the curing temperature.

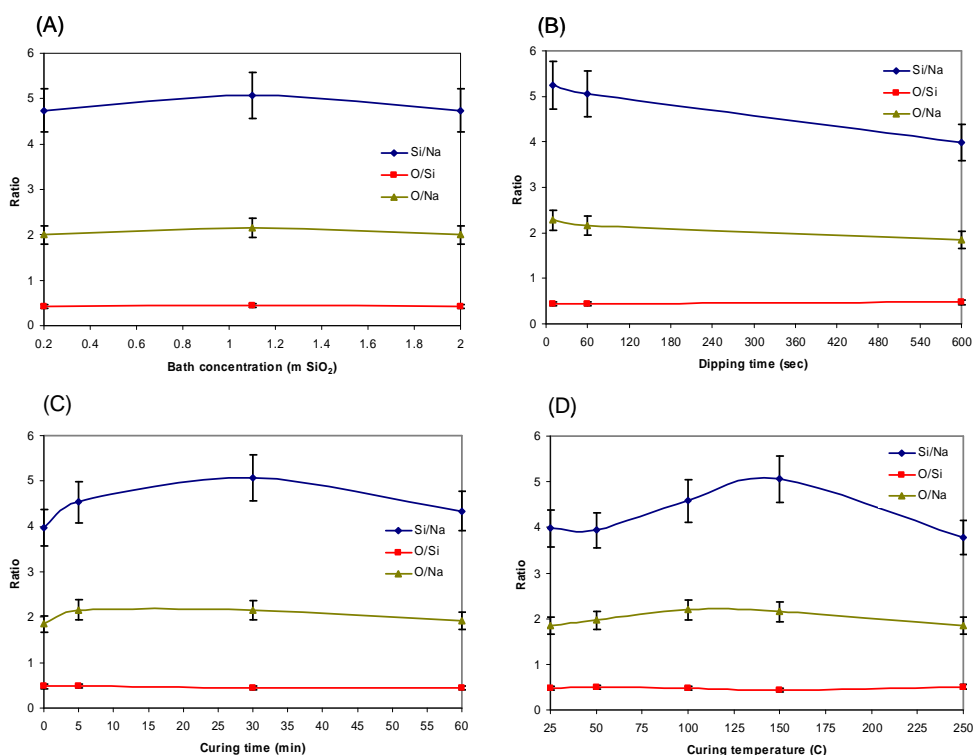


**Figure V.9-2:** Change of the ratios between Si, Na and O by changing the deposition conditions (bath concentrations, dipping time, curing time and curing temperature).

## V.9.1 Discussion

In order to investigate the chemical structure of the silica coating, X-ray photoelectron spectroscopy (XPS) and energy dispersive spectrometry (EDS) were performed. To get a relative estimate of the silica deposit on the aluminium substrate, a survey of the surface

is performed by XPS. Due to the atomic concentrations of 55% of oxygen and 21% of silicon on the surface, an O/Si ratio of 2.5 is calculated. Comparing this ratio with natural occurring minerals, O/Si ratios of 2.5 are found e.g. in kaolinite, which has a silicate sheet structure. Furthermore sodium and carbon was found on the surface. Due to the chemical shifts of the binding energies,  $\text{Na}_2\text{CO}_3$  could be identified.

In order to study the structure within the coating XPS depth profiling is performed. Due to differing ratios between Si, O and Na in various depths, the bulk of the layer as well as the interface coating/aluminium substrate are identified. The bulk of the layer is characterized by a minimum of sodium and a maximum of silicon and oxygen. The O/Si ratio is around 2, which is found in silica ( $\text{SiO}_2$ ) that occurs in a framework structure. In the interface coating/aluminium substrate, aluminium, silicon, oxygen and sodium is detected. The O/Si ratio changed to 2.2 which is between the sheet and the framework structure, indicating a combination of both modifications. Comparing the chemical shift of Si 2p in the interface and in the bulk of the layer, a shift to higher binding energies in the bulk is observed, indicating an increase in the level of polymerisation. Comparing the binding energies of Na 1s, with standards found in natural minerals (including Na, Si, O and Al) different compounds such as zeolite, molecular sieve and aluminosilicates are found. However the role of sodium in the interface is not completely clear yet. A schematic illustration of the coating deposited on an aluminium substrate is given in Figure V.9-3.

To study the uniformity of the layer in correlation with the deposition conditions, EDS analysis is performed. For this purpose, silicate coatings are applied under various bath concentrations, curing temperatures, curing times and dipping times. The focus is on the ratios between Si, O and Na as an indication of changes in correlation with the deposition conditions. The O/Si ratio showed no significant dependency on the deposition conditions, in contradiction to the O/Na and particularly on the Si/Na ratio. The latter one showed a maximum ratio at a curing time of 30 min and at a curing temperature of 150°C. Besides, the minimum is observed after a dipping time of 600 sec. The O/Na ratio showed a similar behaviour, however with less distinct slope of the plots.

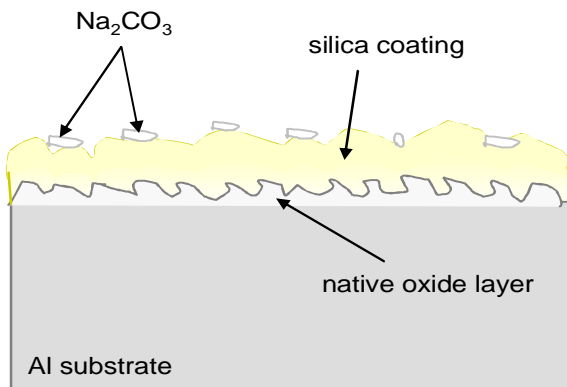


**Figure V.9-3:** Schematic illustration of an aluminium substrate after the deposition of a silica coating.

## V.10 Conclusion

In order to gain chemical information about the silica deposit on aluminium substrates, a range of physical methods such as Raman, FE-SEM/EDX and XPS have been applied. To gain information about the components present in aqueous solutions of various SiO<sub>2</sub> concentrations, Raman spectroscopy has been performed. Due to literature standards of Raman spectroscopy performed in aqueous metasilicate (Na<sub>2</sub>SiO<sub>3</sub>) solutions as well as on their crystalline form, the absorption bands could be attributed. In solution (Na)O-Si-O(H) and (H)O-Si-O(H) bonding and in the coating Na<sub>2</sub>CO<sub>3</sub> and Si-O bondings are associated to the measured vibrations. In aqueous solutions the intensity of the sodium related vibration (1039 cm<sup>-1</sup>) showed a clear dependency on the dissociation level, adjusted by diluting the solution as observed by Halasz et al.<sup>42</sup>. The second peak found in solution was attributed to (H)O-Si-O(H) bonding, since the peak was only observed in aqueous solution and showed no dependency on the bath concentration. Raman spectroscopy was also performed on aluminium substrate after the deposition of a silica layer. The vibration found at 1075 cm<sup>-1</sup> was associated to Na<sub>2</sub>CO<sub>3</sub> in accordance to the XPS results found in this work and to the observations made by Halasz et al.<sup>42</sup>. Furthermore additional intensities appeared at higher wavenumbers, indicating the formation of the silica network by polymerisation. The surface morphology of the silica deposit was investigated by FE-SEM imaging. The observation showed a smooth and dense silica deposit with precipitates on the surface. By varying the deposition conditions the precipitates changed in size, shape and distribution without showing a clear

correlation to the various deposition conditions. In addition to FE-SEM, in-situ OCP measurements are used to investigate the deposition mechanism. After an increase of potential transients within the first 10 to 20 sec, a stable behaviour was observed. These conditions were similar for different substrates (pure aluminium and aluminium alloys), indicating an adsorption process of the deposit, independent of redox systems. Also the thickness was found to be independent of the dipping time and the substrate but showed an increase with increasing bath concentration. In order to study the chemical structure, XPS spectroscopy is performed. By performing depth profiling the evolution of the ratios between Si, O and Na is observed, indicating the different modifications within the layer. Three different areas are found, characterized by changes in the ratios. In the interface the calculated O/Si ratio indicated a combination of silica in framework and in sheet structure. In the bulk of the layer an increase of the degree of the polymerisation of the silica network is observed due to an O/Si ratio of 2 and a shift in the binding energy of the Si 2p peak to higher energies. Finally at the surface, due to a ratio of 2.5 between O and Si and a Si 2p binding energy of approximately 102.5 eV, the modification of silica is attributed to a sheet structure. Furthermore the precipitates observed by FE-SEM imaging are related to  $\text{Na}_2\text{CO}_3$ . In order to study the correlation between uniformity of the layer and deposition conditions, EDS measurements are performed with various bath concentrations, curing times, curing temperatures and dipping times to calculate the ratios between Si, O and Na. The O/Si ratio is not influenced significantly, indicating an independency on the deposition conditions. In contradiction to that the Si/Na ratios showed a maximum increase at a curing time of 30 min and at a curing temperature of 150°C. The minimum occurred after a dipping time of 600 sec. The O/Na ratio showed a similar behaviour, although with a lesser influence on the slope of the plots.

---

## CHAPTER SIX

---

# BARRIER PROPERTIES OF THE SILICA COATING

## **Abstract**

*In this chapter the barrier properties of the silica passivation layer are discussed. The effect of the passivation layer on the corrosion performance on AA4045/3003/4045 brazing sheets is shown during SWAAT exposure. Moreover, the effect of the passivation layer on the susceptibility to localized attack is investigated by potentiodynamic polarization measurement. By potentiostatic polarization scans, the effect of various deposition conditions (bath concentration and dipping time) and curing conditions (curing temperature and curing time) on the barrier properties of the silica layer is investigated. Furthermore, a conclusion about the failure of the passivation layer is given by morphological investigations by means of SEM/EDS within an area of local attack.*

*The results show that the passivation layer acts as a physical barrier layer, which means that no effect on the corrosion behaviour is found, but on the corrosion rate. By increasing the bath concentration of the aqueous sodium silicate solution an increase on the barrier properties is observed. Besides, increasing the curing temperature, curing time and dipping time showed a beneficial effect, too. The breakdown of the layer is found as local defects (pits), revealing the aluminium substrate to the aggressive environment.*

## VI. Barrier properties of the silica coating

### VI.1 Introduction

This chapter deals with the investigation of the barrier properties of the silica passivation layer by accelerated corrosion testing. As reported on steel substrates, silica passivation layers are acting as barrier layers to protect the underlying surface against corrosion.<sup>44,49,50</sup> However no literature about silica coatings on aluminium substrates is found, since the focus is on steel up to now.

In order to investigate the effect of the passivation layer on the corrosion behaviour of AA4045/3003/4045 brazing sheets, the coated samples are exposed to SWAAT. To follow the corrosion propagation SEM characterization is performed.

By means of potentiodynamic polarization measurements the susceptibility to localized corrosion of bare and coated substrates are compared. By potentiostatic polarization the effect of various deposition conditions on the barrier properties are measured. Finally the breakdown of the silicate passivation layer is investigated by SEM/EDX in order to gain information about the protection mechanism.

### VI.2 SWAAT performance of pre-treated aluminium substrates

The corrosion performance of silica passivation layers deposited on aluminium brazing sheets (AA4045/3003/4045) is measured during salt spray testing (SWAAT). To vary the layer thickness, different bath concentrations are used (Table VI-1). The details of the deposition conditions are given in Chapter III.

Figure VI.2-1 shows images of optical microscopy (OM) of samples immersed in a 0.2 m (A), 1.1 m (B), 2.0 m (C) and 3.0 m (D) sodium silicate solution after 2 days of SWAAT exposure. No significant differences are observed with the different conditions. Independent of the layer thickness corrosion starts in the re-solidified clad material by an attack of the aluminium matrix next to the nobler silicon located in the eutectic. After 7 days of SWAAT exposure (Figure VI.2-2) only the samples coated with 0.2 m SiO<sub>2</sub> (A) and 1.1 m SiO<sub>2</sub> (B) showed a progress of corrosion attack in the aggressive SWAAT

solution but not the samples coated with 2.0 m SiO<sub>2</sub> (C) and 3.0 m SiO<sub>2</sub> (D). After 12 days of SWAAT exposure (Figure VI.2-3) the cross-sectional view of the specimens coated with 2.0 m (C) and 3.0 SiO<sub>2</sub> (D) still reveal no progress in the corrosion attack. In the coatings made of 0.2 m (A) and 1.1 m SiO<sub>2</sub> (B) the corrosion propagates to the core material via intergranular attack along the grain boundaries.

**Table VI-1:** Deposition conditions for SWAAT.

Bath concentration (m SiO <sub>2</sub> )	Immersion time (sec)	Curing time (min)	Curing temperature (°C)
0.2 (A)	60	30	150
1.1 (B)			
2.0 (C)			
3.0 (D)			

Considering the results a clear tendency is observed: by increasing the bath concentration of the sodium silicate solution the barrier properties of the passivation layer increase. It is concluded that the initiation of corrosion is not affected by the coating, since the corrosion depth after 2 days SWAAT exposure is the same for the various bath concentrations. However after 7 and 12 days the samples immersed in the higher bath concentrations showed a significant reduction of the corrosion propagation. The depth of the corrosion propagation as a function of SWAAT duration is presented in Figure VI.2-4. The plot labelled with as-received shows the behaviour of the bare brazing sheet (without silica coating).

These observations are confirmed with results of Tada et al.<sup>50</sup> They reported for silica coated steel that there is no reduction on the corrosion rate during initiation but for the propagation.

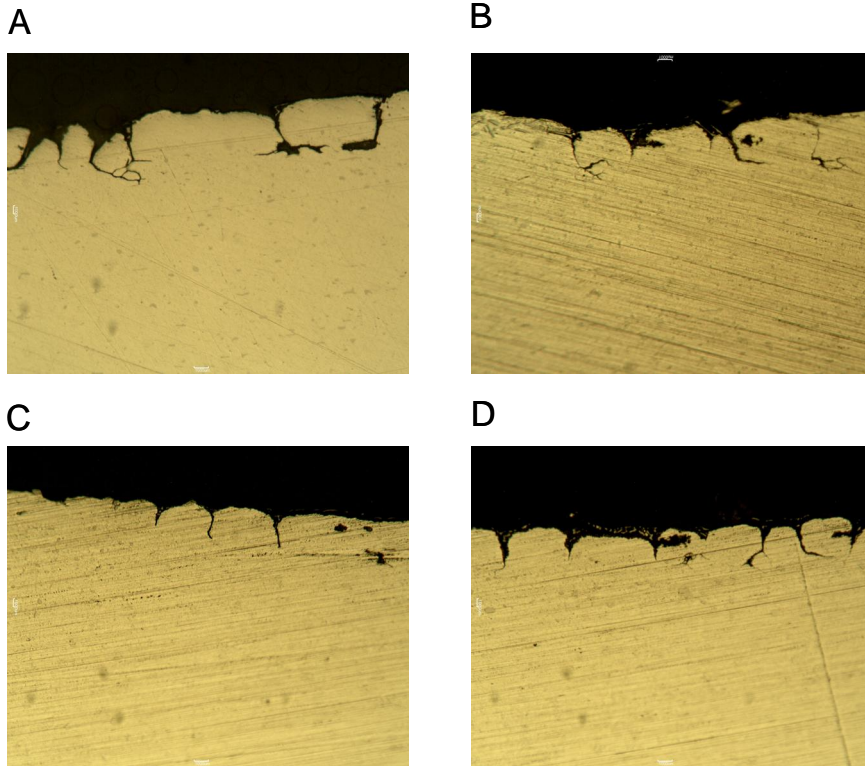


**Figure VI.2-1:** Micrographs (magnification: 200x) of cross-sections of aluminium brazing sheets after two days of SWAAT exposure (Bath concentration: 0.2m SiO<sub>2</sub> (A); 1.1m SiO<sub>2</sub> (B); 2.0 m SiO<sub>2</sub> (C); 3.0 m SiO<sub>2</sub> (D)).

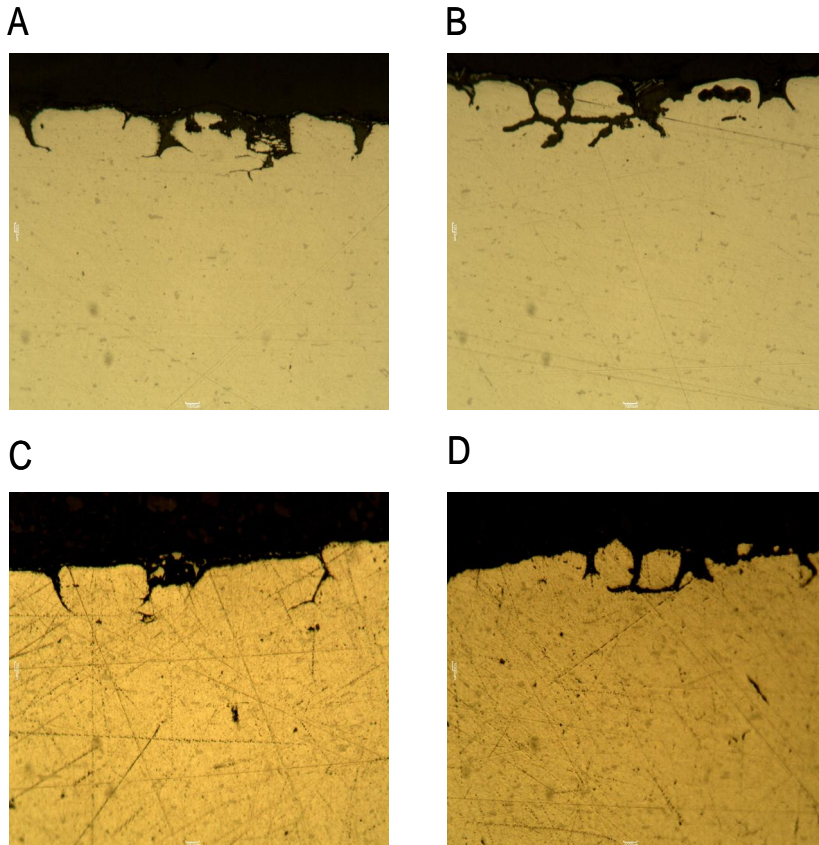


**Figure VI.2-2:** Pictures A to D show the optical micrographs (magnification: 200x) of cross-sections of aluminium brazing sheets pre-treated with different bath concentrations after seven days of SWAAT exposure (A: 0.2m SiO<sub>2</sub>; B: 1.1m SiO<sub>2</sub>; C: 2.0 m SiO<sub>2</sub>; D: 3.0 m SiO<sub>2</sub>).

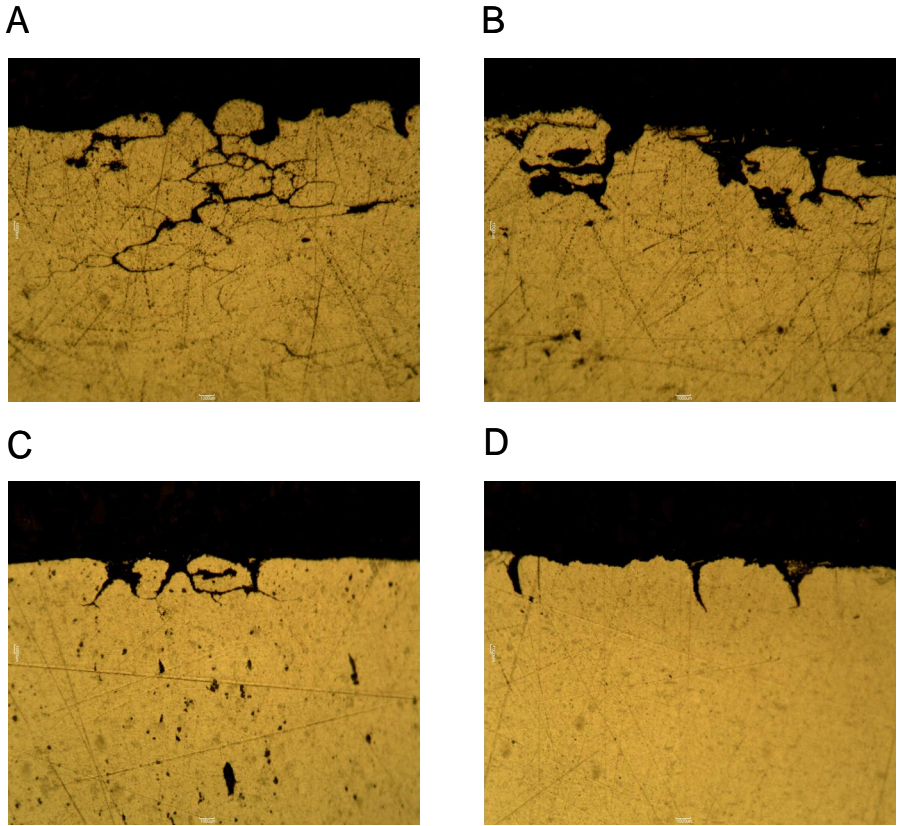


**Figure VI.2-3:** Pictures A to D show the optical micrographs (magnification: 200x) of cross-sections of aluminium brazing sheets pre-treated with different bath concentrations after twelve days of SWAAT exposure (A: 0,2m SiO<sub>2</sub>; B: 1,1m SiO<sub>2</sub>; C: 2,0 m SiO<sub>2</sub>; D: 3,0 m SiO<sub>2</sub>).

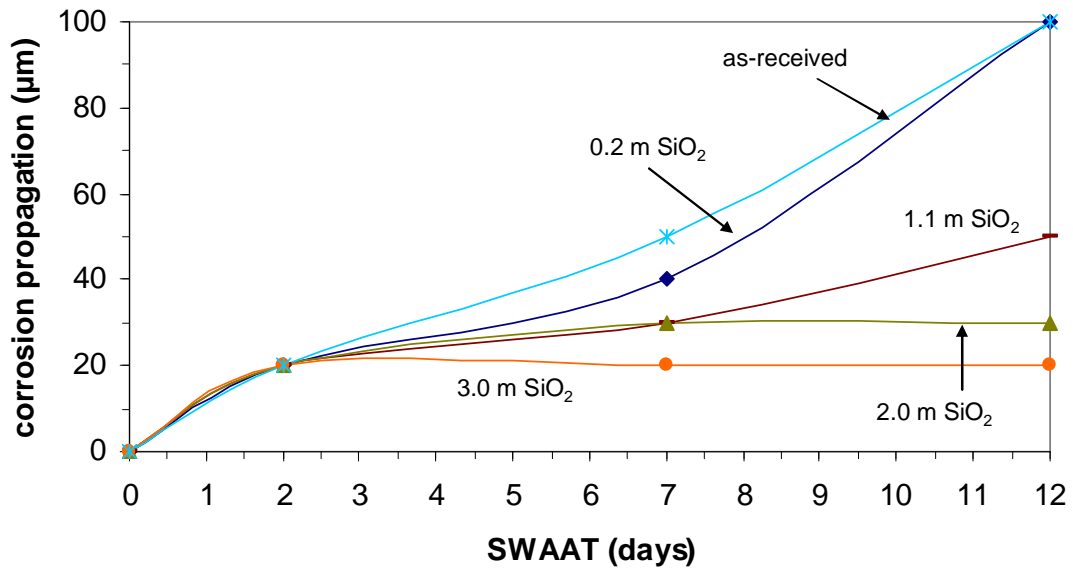


**Figure VI.2-4:** Corrosion depth as function of SWAAT duration.

### VI.3 Breakdown of the passivation layer

In order to investigate the morphology and the elemental composition of an area revealing a breakdown of the silicate passivation layer, FE-SEM/EDS measurements are performed. For this purpose the coatings are applied on Al99.99% substrates with a bath concentration of 0.2 m SiO<sub>2</sub>. The application of the coating is described in detail in Chapter III. Although no reference measurements with SWAAT have been performed on uncoated Al99.99%, this material was used, since the focus of this investigation is given to the properties of the barrier layer without considering the effect on the substrate. Besides, it is of crucial importance to use a silicon free alloy to perform reliable EDS measurements of the coating.

Figure VI.3-1 shows the surface of the sample after 11 days of SWAAT exposure. To gain information about the layer thickness, cross-sections are prepared by bending the samples after immersion in liquid nitrogen. Figure VI.3-1 (A) shows an area where several pits occurred. The EDS measurement in the pit (C) revealed only a strong intensity of aluminium. Oxygen is hardly detected, which means that the aluminium bulk material is reached in the pit. However around the pits the silicate layer is still in good order. The gaps of the layer are an effect of the bending process and hence independent of the corrosion attack. The EDS results received in an area where the layer is still intact (B) reveal a high intensity of silicon and oxygen, in accordance to the silica layer. Besides, the layer thickness (B) around 130 nm is comparable to the thickness calculated prior to the accelerated corrosion testing (Chapter VI). The additional Pt intensity found in the spectra is due to the application of a Pt layer to avoid charging effects and hence will not be considered here.

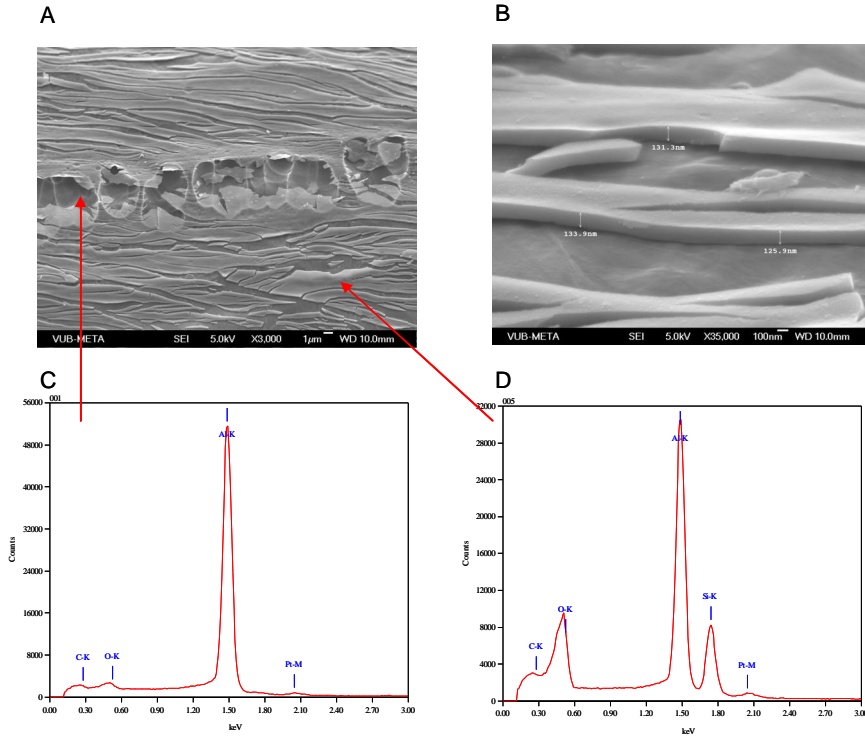


**Figure VI.3-1:** Local breakdown of the silicate passivation layer during accelerated corrosion testing (SWAAT).

Considering the results, the breakdown of the layer is found in local pits with a size of several  $\mu\text{m}$ , enabling attack of the electrolyte to the substrate. Since the pits found on the surface are all formed in a row, it is concluded that the local attack preferentially occurs at defects in the layer, which can be caused by inhomogeneities on the substrate (impurity, scratch). As the constant layer thickness prior and after the SWAAT showed, the coating is not dissolved by the aggressive environment of the SWAAT.

#### VI.4 Electrochemical measurements

In the previous section the influence of the layer thickness (adjusted by different bath concentrations) of the silicate coating on the corrosion performance is shown during conventional salt spray testing (SWAAT). To gain further results on the sensitive layer properties electrochemical techniques are performed to ensure reliable and reproducible results.

#### VI.4.1 Potentiodynamic polarization curves on coated AA4045/3003/4045 brazing sheets

In order to gain information about the susceptibility to localized attack by means of potentiodynamic polarization curves, the focus is given to: (i) position of breakdown potentials, (ii) value of limit current density and (iii) re-passivation behaviour. In Chapter IV these polarization scans have been performed on the uncoated substrates to identify the different breakdown potentials and hence appropriate certain potential ranges to the respective type of localized corrosion. In this section the polarization scans are performed with silica coated substrates. For this purpose aluminium brazing sheets are immersed in an aqueous sodium silicate solution, consisting of 1.1 m SiO<sub>2</sub>. A SWAAT solution was used as electrolyte for the electrochemical scans was as for the uncoated samples. The details for the pre-treatment and the polarization scans are described in Chapter III. In Figure VI.4-1 the polarization scans for aluminium brazing sheets (AA4045/3003/4045) with different material conditions are shown. The values measured are listed in

Table VI-2. Considering the different curves in Figure VI.4-1 the following behaviour is found. The alkaline cleaned surface (Ridoline 34) shows the lowest OCP (-0.52 V) in comparison to a slightly nobler one (-0.51 V) of the bare substrate without a coating (B). An OCP of -0.48 V is measured for the deep-drawn sample after deposition of a silica coating (C) and finally at the plane and coated sample (D) a potential of -0.47 V is measured. At the OCP in the backwards scan the order differs on the following way: The uncoated material (A) shows the lowest OCP (-0.60 V) followed by the alkaline cleaned substrate (B) with -0.55 V. The coated plane material (D) showed -0.54 V and finally the deep-drawn silicate coated material with -0.54 V. At -0.43 V all curves show the first breakdown potential which is attributed to pitting corrosion. Considering the current density the different material conditions are distinguished. The highest current density (-3.96 i/Acm<sup>-2</sup>) is measured on the alkaline cleaned sample (B). Slightly lower is the uncoated material (A) (-4.04 i/Acm<sup>-2</sup>) and finally the deep-drawn silicate coated (C) (-4.51 i/Acm<sup>-2</sup>) and the plane sample coated with silicate (D) (-4.82 i/Acm<sup>-2</sup>). This order is also found at the limit anodic current density. However the deviation between the

different materials is very low. Comparing the curves at a potential at the limit cathodic current density, the deviation is more significant. The lowest current density (-3.23 V) is found for the plane material coated with the silicate passivation layer. A slightly higher current density (-3.16 V) is found in the coated deep-drawn material and higher current densities in the uncoated (-2.92 V) and the alkaline cleaned substrate (-2.83 V).

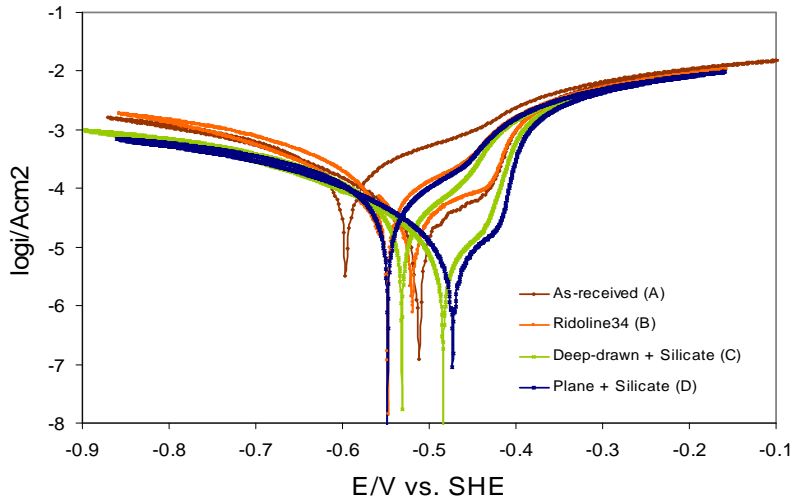


**Figure VI.4-1:** Cyclic voltammety for brazing sheets under different conditions. The uncoated material (A); alkaline cleaned with Ridoline 34 (B); silicate coating on deep-drawn material (C) and silicate coated plane brazing sheets (D).

The existence of a more negative OCP in the forward scan for the two uncoated materials (A, B) is an indication of a higher susceptibility to localized corrosion compared to the coated material. Besides, the higher current densities and the more negative OCP in the backwards scan propose a lower rate for the re-passivation after the local attack. Particularly the more significant decrease of the limit cathodic current density for the coated samples is an indication for the barrier properties of the silica layer reducing the cathodic reaction rate at the intermetallics.

**Table VI-2:** Characteristic potentials found in the polarization curves shown in Figure VI.4-1.

Material conditions	OCP 1 ( $E_{SHE}/V$ )	OCP 2 ( $E_{SHE}/V$ )	Current density ( $\log i/Acm^{-2}$ ): $E_{SHE} = -0,43V$	Current density ( $\log i/Acm^{-2}$ ): $E_{SHE} = -0,8V$
Ridoline34 (B)	-0.52	-0.55	-3.96	-2.83
As-received (A)	-0.51	-0.60	-4.04	-2.92
Deep-drawn + silica (C)	-0.48	-0.53	-4.51	-3.16
Plane + silica (D)	-0.47	0.54	-4.82	-3.23

#### VI.4.2 Potentiodynamic polarization curves on coated Al99,99%

Figure VI.4-2 shows the cyclic voltammetry scan of Al99.99%. The coating is prepared under the same conditions as for the brazing sheets. The OCP in the forward scan was found at -0.59 V for the uncoated and at -0.65 V for the coated material. The values for the OCP in the backwards scan are -0.60 V for the uncoated and -0.65 V for the coated substrates.. Furthermore, the curve attributed to the silicate coated sample showed a significant lower limit anodic and limit cathodic current density in comparison to the bare material.

The more negative OCP of the coated material is an indication of a higher susceptibility to localized corrosion of this material compared to the uncoated sample. However this behaviour cannot clearly be attributed to the silica coating since the OCP is also dependent on factors such as properties of the oxide layer and presence of intermetallics. Besides, the decrease of the current densities for the coated sample indicates good re-passivation properties of the coating after the local attack.

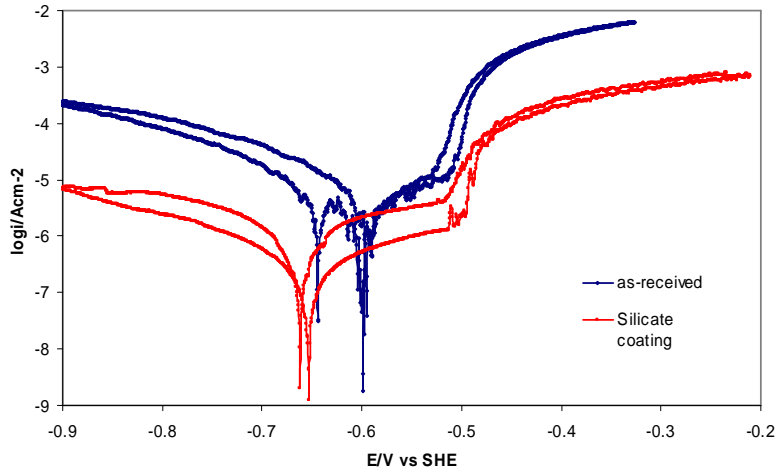


**Figure VI.4-2:** Cyclic voltammetry scans of Al99,99% after deposition of the silicate passivation layer.

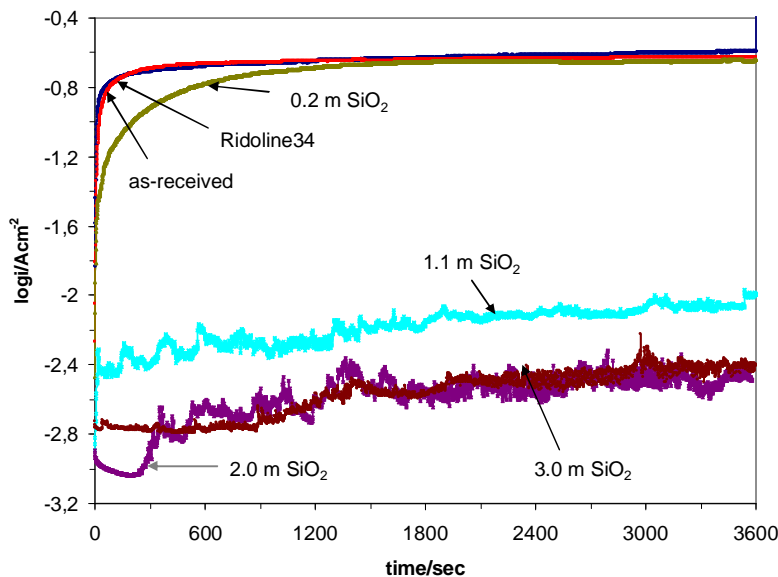
### VI.4.3 Potentiostatic polarization curves with Al 99.99%

As observed in the cyclic voltammetry scans ([Figure VI.4-2](#)), the silicate passivation layers have a strong influence on the anodic and cathodic branch of the polarization curves. This property is used to investigate the influence of different deposition conditions on the barrier properties of the layer. During this study, focus is given to properties concerning the silicate layer without considering the effect of the corrosion on the substrate. For this purpose, a substrate with a homogeneous surface is chosen (Al99.99%) to ensure reproducible conditions for the deposition process. As it is shown during SWAAT exposure, the silicate barrier properties are less significant during corrosion initiation, but during corrosion propagation. For this purpose the applied potential during for the potentiostatic polarization scans is chosen at  $-0.4 \text{ V}$  which is above the second breakdown potential.

### VI.4.3.a Effect of the bath concentration on the potentiostatic polarization measurement

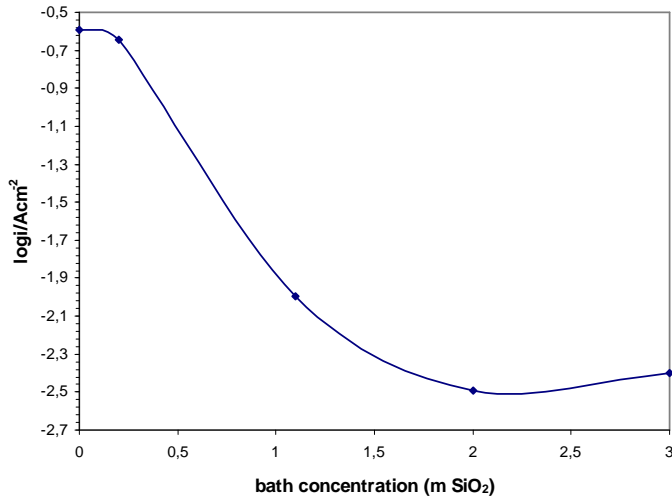
In order to investigate the influence of the layer thickness on the barrier properties, the silicate coatings are applied with various bath concentrations. The remaining deposition conditions are adapted to the standard pre-treatment introduced in Chapter III.

Figure VI.4-3 presents the potentiostatic polarization curves of Al.99.99% under the following deposition conditions: uncoated (A), alkaline cleaned (B), 0.2 m bath concentration (C), 1.1 m bath concentration (D), 2.0 m bath concentration (E) and 3.0 m bath concentration (F). Within the first 50 seconds the as-received (A) as well as the alkaline cleaned sample (B) showed a strong increase in the current transients till a stable value at around  $-1.3 \text{ i/Acm}^{-2}$  is reached. The slope of plot (C) is less strong within the first 10 minutes till it reached a stable value in the same range as the plots (A) and (B). By increasing the bath concentration, the plots (F), (G) and (H) showed just a slight slope during the beginning of the measurements and reached a stable value after around 30 minutes. These values are  $-4.0 \text{ i/Acm}^{-2}$  for 1.1 m  $\text{SiO}_2$  (D) and around  $-5.0 \text{ i/Acm}^{-2}$  for 2.0  $\text{SiO}_2$  (E) and 3.0 m  $\text{SiO}_2$  (F).



**Figure VI.4-3:** Current transients for various bath concentrations, measured at constant potential of  $-0.4 \text{ V}$  vs. SHE.

In [Figure VI.4-4](#) the values of the current densities after 60 min are plotted against the bath concentration. Increasing the bath concentration to 2.0 m SiO<sub>2</sub> a decrease of the current density occurs. Between 2.0 m and 3.0 m SiO<sub>2</sub> the plot is stable.



**Figure VI.4-4:** Current density after 60 min potentiostatic polarization measurements as function of the bath concentration.

Considering these results the increase of the bath concentration resulted in an increase of the barrier properties, since the current density, which is an indication for the corrosion rate, decreased. In concentration between 0.2 m and 2.0 m SiO<sub>2</sub> the plots decreased and remained stable by increasing the concentration to 3.0 m SiO<sub>2</sub>.

### VI.4.3.b Curing temperature

In order to investigate the influence of the curing temperature on the barrier properties, the silicate coatings are applied with various curing temperatures. The remaining deposition conditions are adapted to the standard pre-treatment introduced in Chapter III.

[Figure VI.4-5](#) presents the potentiostatic polarization curves of Al.99.99% under the following deposition conditions: uncoated (A), alkaline cleaned (B), room temperature (C), 50 °C (D), 100 °C (E) and 150 °C (F). The plots of the samples (A)-(E) showed a comparable progress during the measurements. Within the first minutes there is a slope in the plots till a stable current is reached. The time to achieve a stable current is longer and

the stable current is lower as the curing temperature increased. A significantly lower stable current density is found at 150°C (F).

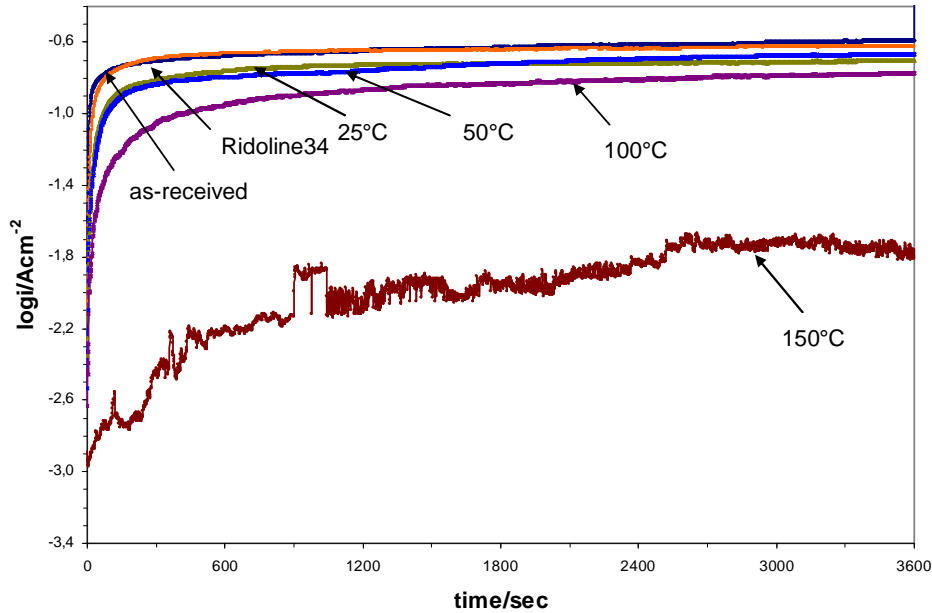


**Figure VI.4-5:** Current transients for various curing temperatures, measured at constant potential of -0,4 V vs. SHE.

In Figure VI.4-6 the values of the current densities after 60 min are plotted against the curing temperature. The curve remained stable up to a temperature of 100°C and decreased by increasing the temperature to 150°C.

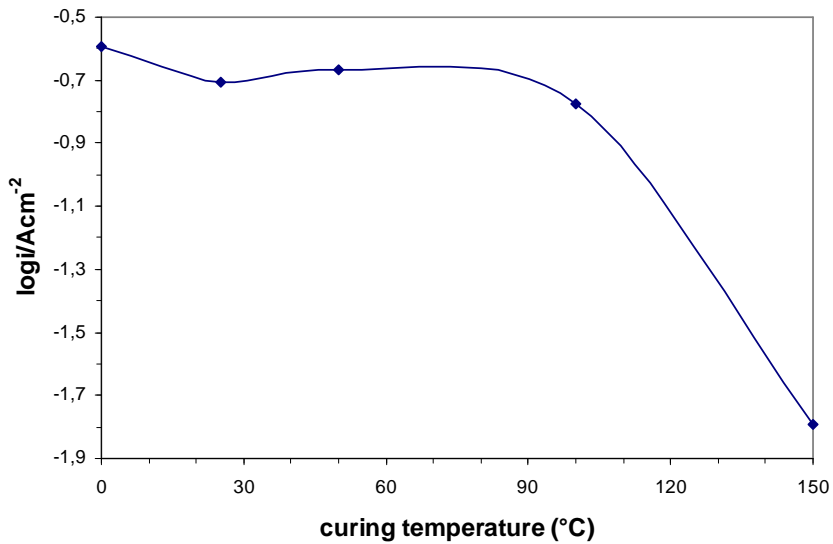


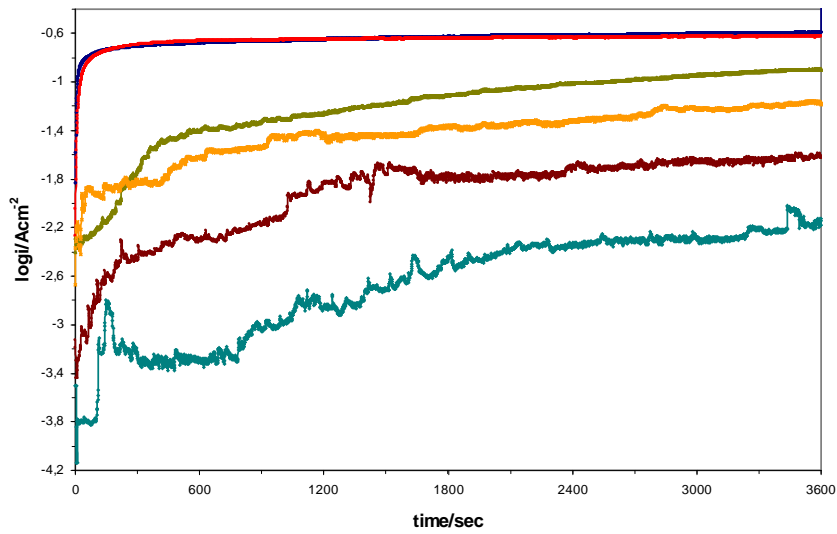
**Figure VI.4-6:** Current density after 60 min potentiostatic polarization as function of the curing temperature.

Considering the results, the curing temperature shows no significant deviation between curing at room temperature and 100°C. For improving the barrier properties a curing temperature of 150°C is necessary.

### VI.4.3.c Curing time

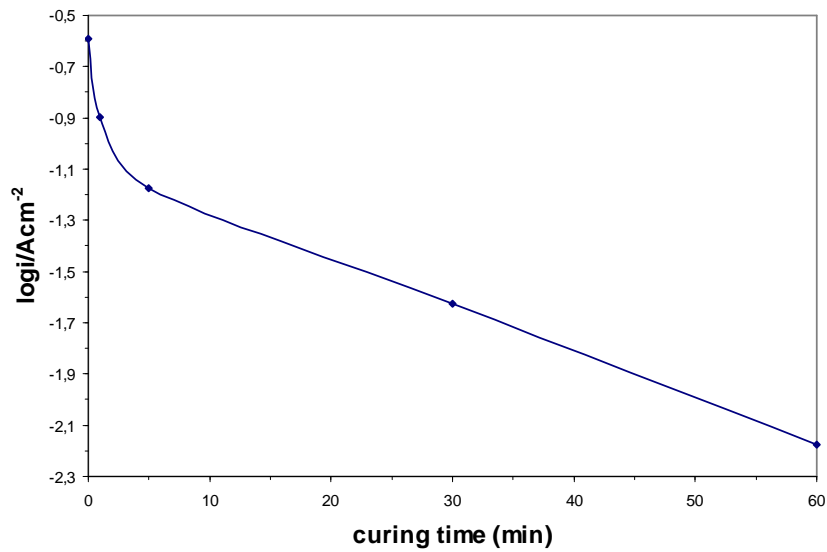
In order to investigate the influence of the curing time on the barrier properties, the silica coatings are applied with various curing times. The remaining deposition conditions are adapted to the standard pre-treatment introduced in Chapter III.

Figure VI.4-7 presents the potentiostatic polarization curves of Al.99.99% under the following deposition conditions: uncoated (A), alkaline cleaned (B), no curing (0 min) (C), 1 min (D), 5 min (E), 30 min (F), 60 min (G). The plots attributed to the coated samples show in comparison to the uncoated samples a less strong increase of the current density and the time to achieve a stable current was longer. Finally the reached stable current density was lower with increasing curing time.



**Figure VI.4-7:** Current transients for various curing times, measured at constant potential of -0.4 V vs. SHE.

In Figure VI.4-8 the values of the current densities after 60 min are plotted against the curing time. The curve decreased by increasing the curing time up to 60 minutes.



**Figure VI.4-8:** Current density after 60 min potentiostatic polarization as function of the curing temperature.

## VI.4.3.d Dipping time

In order to investigate the influence of the dipping time on the barrier properties, the silica coatings are applied with various dipping times. The remaining deposition conditions are adapted to the standard pre-treatment introduced in Chapter III.

Figure VI.4-9 presents the potentiostatic polarization curves of Al.99.99% under the following deposition conditions: uncoated (A), alkaline cleaned (B), 10 sec (C), 60 sec (D), 300 sec (E) and 600 sec (F) dipping time. By increasing the dipping time, the plots showed a less strong increase of the current. Finally the values reached for the stable behaviour of the transient was lower.

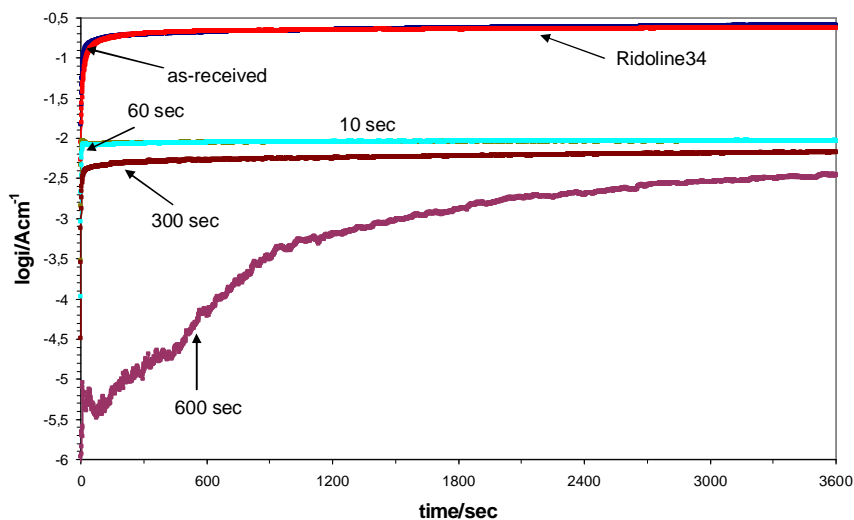


**Figure VI.4-9:** Current transients for various dipping times, measured at constant potential of -0.4 V vs. SHE.

In

Figure VI.4-10 the values of the current densities after 60 min are plotted against the dipping time. The curve decreased by increasing the dipping time up to 600 sec.

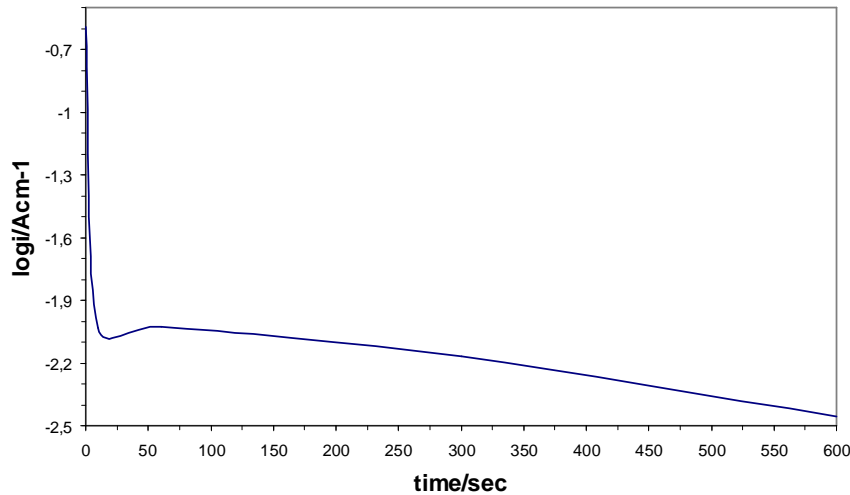


**Figure VI.4-10:** Current density after 60 min potentiostatic polarization as function of the dipping time.

## VI.5 Conclusion

In this chapter the corrosion performance of AA4045/3003/4045 brazing sheets coated with a silicate passivation layer is discussed. Moreover the effect of various pre-treatment conditions on the barrier properties of the silicate layers is investigated.

To investigate the effect of the layer thickness on the corrosion performance, aluminium brazing sheets were exposed to salt spray testing (SWAAT). For this purpose the brazing sheets are immersed in silicate solution with various bath concentrations to adjust the layer thickness. During SWAAT exposure the layer thickness showed hardly any effect on the corrosion initiation but on the propagation. The corrosion propagation (calculated by the corrosion depth) during SWAAT of the silica coated samples was 80% less compared to the uncoated samples.

The study of the barrier properties by means of potentiostatic polarization scans revealed the following correlations:

- Increasing the bath concentration to 2.0 m SiO<sub>2</sub>, the barrier properties increase.
- Increasing the curing temperature to 150°C, the barrier properties increase.
- Increasing the curing time to 60 min, the barrier properties increase.
- Increasing the dipping time to 600 sec, the barrier properties increase.

Moreover the local breakdown in the passivation layer is investigated after SWAAT exposure. Cross-sections of the silicate layer revealed local attack (pits). The initiation occurs probably at defects of the layer due to surface properties (impurities, scratches).

---

## CHAPTER SEVEN

---

# CONCLUSIONS

## VII. Conclusions

The first part of the thesis deals with the morphological and electrochemical behaviour of AA4045/3003/4045 aluminium brazing sheets. By means of SEM/EDS the material was investigated before and after the brazing process to follow the changes in the microstructure due to the influence of the heat treatment. In the post-brazed material different phases such as Al-Fe-Mn-Si (mainly present as  $\alpha$ -Al(Fe,Mn)Si particles),  $Al_6(Fe,Mn)$  and Al-Mn-Si are identified. In comparison to that, the dominant phase present in the pre-brazed material is  $Al_6(Fe,Mn)$ . This change in the elemental composition was initiated by the enhanced diffusion of Si from the core to the clad material, incorporating in precipitates and stimulating increased precipitation of Mn from solid solution, resulting in a dense band of precipitates (DBP). Furthermore the effect of the diffusion process is found in an increased amount of  $[Si]_{ss}$  in the diffusion zone and a decrease of  $[Mn]_{ss}$  in the same area. Cu, which has a lower diffusion rate, was detected in less amounts in solid solution in the diffusion zone and the clad material.

After the morphological characterization by EDS, the electrochemical behaviour of the brazing sheets was studied during SWAAT exposure. The initiation of the corrosion attack was found in the eutectic of the re-solidified clad. The local attack (pitting) started by dissolution of the aluminium matrix, which is in contact to the more noble Si particles. The pitting transforms after a few days of SWAAT exposure to intergranular corrosion. This form of localized attack continues along the grain boundaries through the diffusion zone, due to the enrichment of alloying elements present in the grain boundaries and the resulting potential difference between this area and the aluminium matrix. Finally after 16 days of salt spray testing, perforation of the entire brazing sheet occurred.

Relating the characterization of the microstructure and the electrochemical behaviour, the corrosion propagation of AA4045/3003/4045 brazing sheets can be explained by observing the corrosion potential differences, occurring in the different layers (clad material, diffusion zone, core material). The increase of corrosion potential in the diffusion zone compared to the core material is caused by the higher  $[Si]_{ss}$  and  $[Cu]_{ss}$  content in the diffusion zone, forcing a galvanically driven attack of the core material by the diffusion zone.

In order to overcome the drawbacks of the SWAAT (long duration, low reproducibility), open-circuit-potential, potentiodynamic and potentiostatic measurements were performed to study the effect of the brazing temperature and mechanical transformation on the corrosion performance of the brazing sheets.

Increasing the brazing temperature reduced the susceptibility to localized attack (intergranular corrosion). This enhanced heat treatment caused an increased precipitation of solute atoms in the matrix, reducing the potential differences between matrix and grain boundaries. This change in the morphology was reflected by a shift of the OCP in the negative direction and a reduction of the current densities in the potentiodynamic polarization curves.

The mechanical transformation (Erichsen impression) showed no significant effect on the corrosion behaviour.

A correlation between SWAAT and potentiodynamic and potentiostatic polarization measurements during corrosion initiation and propagation was found. Potentiodynamic polarization curves revealed breakdown potentials on the material, which were correlated to the specific localized attack (pitting and IGC). These forms of localized attack were induced by potentiostatic polarization measurements by applying one potential for one hour. Hence this application offers, within a few hours, the same simulation of corrosion propagation found after several days of SWAAT exposure.

The second part of the thesis was dedicated to the application of a silica passivation layer on aluminium substrates. The focus was on the effect of deposition conditions on the morphology and chemistry of the layer. Different techniques have been used to study the silica layer. Every technique provides information about the various parameters being involved in the silica chemistry and hence helps to reveal a general understanding for the application of the coating.

Raman spectroscopy enables to study the chemistry of silica in solution and after deposition on the substrate. In solution a dependency of the dissociation rate of sodium to the bath concentration was found, indicating a high amount of monomeric or at least less polymeric species in solution. After curing of the silica layer on aluminium substrates

polymerization of the layer occurred, reflected the appearance of a vibrational intensity at higher wavenumbers.

Open-circuit potential (OCP) was recorded during immersion of an aluminium substrate in the aqueous silica solution. This revealed that the deposition of silica mainly takes place during the first 20 sec by physical adsorption. This behaviour is reflected in an initial decrease of the OCP (activation of the aluminium surface by dissolving the native oxide layer in the alkaline environment). After that the potential transient revealed no significant change, indicating an adsorption of silica without redox reactions. Although with aluminium brazing sheets a slight increase of the OCP occurred after the initial decrease, the deposition process is suggested to be based on physical adsorption. It is proposed that the potential increase is caused by the re-passivation reaction of the aluminium substrate in the alkaline solution and not due to adsorption process. This contact of the substrate with the electrolyte is possible, since the electrolyte can penetrate through the silica layer and hence influence the potential transient. Furthermore morphological investigations by FE-SEM have shown that the layer thickness is independent of the substrate (pure aluminium and aluminium brazing sheets), indicating no influence on the deposition rate of the cathodic intermetallic phases only present on the surface of the brazing sheet. Moreover after a dipping time of around 10 to 20 sec. no further increase of the thickness of the layer is observed. It is found that the final thickness of the layer is determined by the silica bath concentration and is independent of dipping times longer than 10 to 20 sec. The same independency is found among the curing time and curing temperature.

The chemical state of the silica layer was measured by FE-SEM/EDS and XPS.

FE-SEM/EDS gave information on the elemental composition of the silica layer in correlation to the deposition conditions is measured. The focus was on the ratios between Si, O and Na as an indication of the effect of various deposition conditions on the uniformity of the silica coating. Different deposition conditions (bath concentrations, curing temperatures, curing times and dipping times) showed no influence on the SiO<sub>2</sub> structure, as reflected in a constant O/Si ratio, but revealed an effect on the O/Na and particularly the Si/Na ratios. A very low deposition of sodium (high Si/Na ratio) was found both with a curing time of 30 min and with a curing temperature of 150°C.

Besides, a maximum amount of sodium (low Si/Na ratio) in the layer was obtained after a dipping time of 600 sec.

To complete the chemical state analysis of the silica layer, XPS measurements were performed. Due to the low penetration depth of the electron beam in comparison to FE-SEM/EDS, this technique enables an elemental analysis of the outer layer of the coating. Moreover it is possible to perform depth profiling by Ar sputtering enabling chemical information layer by layer within the coating and hence gaining the chemical composition of the layers as function of depth.

In the outer surface layer mainly  $\text{Na}_2\text{CO}_3$  was found in correlation to the Raman intensities. This compound is present as “pollution” in aqueous silica solution. Furthermore, the O/Si ratio of 2.5 indicates that silica occurs in a sheet structure. In the bulk of the layer silica modified to higher polymerized forms and occurs in a three dimensional framework structure. This is concluded by observing the shift of the high resolution peak of Si 2p to higher intensities and an O/Si ratio of 2. The interface reveals a complex combination of silica species. After fitting the high resolution spectrum of the Si 2p peak both forms, monomeric and polymeric, were found. This result is also reflected in an O/Si ratio of 2.2, indicating a combination of sheet and framework structure of silica.

The last part of the thesis is dedicated to the barrier properties of the silica layer. After SWAAT exposure of aluminium brazing sheets a significant reduction of the corrosion propagation of the substrates coated with the silica layer in comparison to the substrates without coating is observed. After 12 days in the salt spray test, the corrosion propagation, calculated by the penetration depth within the material, was reduced up to 80% by the presence of the silica coating. This improvement of the corrosion performance is confirmed by electrochemical measurements. The potentiodynamic polarization curves performed on substrates after the deposition of the passivation layer reveal a decrease of the current densities. Moreover the deposition conditions show an effect on the barrier properties of the silica layer. Increasing the silica bath concentration to 2.0 m  $\text{SiO}_2$ , the curing temperature to 150°C, the curing time to 60 min and the dipping

time to 600 sec revealed a decrease of the current density during potentiostatic polarization measurements, indicating an improvement of the deposition conditions.

Although the deposition conditions have an effect on the uniformity of the layer (variations in the Si/Na and O/Na ratios) and on the barrier properties of the layer (variations in the current transients) no clear correlation between the sodium level in the layer and the barrier properties is found. To explain this behaviour, the sodium ions are proposed to act as bridging components in the interface connecting the silica layer with the aluminium substrate and providing good adhesion properties between the coating and the substrate. This mechanism is supposed to be independent of the deposition conditions. Hence, the effect of different deposition conditions on the Si/Na and O/Na ratios can be attributed to the amount of  $\text{Na}_2\text{CO}_3$  on the surface, which is not affecting the barrier properties of the layer. The change of the amount of  $\text{Na}_2\text{CO}_3$  on the surface is confirmed by the modification of the morphology of the surface, observed after applying various deposition conditions.

## References

---

- [1] W. S. Miller, L. Zhuang, J. Bottema, A. J. Wittebrood, P. De Smet, A. Haszler, A. Vieregge, *Materials Science and Engineering*, **2000**, A280 37-49
- [2] S. Meijers, *Corrosion of aluminium brazing sheet*, **2002**, ISBN 90-805661-3-6 (PhD Thesis)
- [3] S. Tierce, N. Pebere, C. Blanc, C. Casenave, G. Mankowski, H. Robidou, *Corrosion Science*, **2007**, *49*, 4581-4593
- [4] W. Zhang, G.S. Frankel, *Electrochimica Acta*, **2003**, *48*, 1193-1210
- [5] R.G. Buchheit Jr., J.P. Moran, G.E. Stoner, *Corrosion*, **1990**, *46*, 610-617
- [6] T. Ramgopal, G. S. Frankel, *Electrochemical Society Proceedings*, **2001**, 2000-23, 411-421
- [7] Ramgopal, P.I. Gouma, G.S. Frankel, *Corrosion*, **2002**, *58*, 687-697
- [8] D. T. L. Alexander, A. L. Greer, *Acta Materialia*, **2002**, *50*, 2571-2583
- [9] G. Svenningsen, M. H. Larsen, J. C. Walmsey, J. H. Nordlien, K. Nisancioglu, *Corrosion Science*, **2006**, *48*, 1528-1543
- [10] F. Andreatta, H. Terry, J. H. W. De Witt, *Electrochimica Acta*, **2004**, *49*, 2851-2862
- [11] A. Afseth, J. H. Nordlien, G. M. Scamans, K. Nisancioglu, *Corrosion Science*, **2002**, *44*, 145-162
- [12] F. N. Speller, *J. Franklin Institute*, **1922**, *193*, 519
- [13] D. Krupa, J. Baszkiewicz, J. Zdunek, T. Borowski, J. Smolik, *Proceedings EUROCORR*, **2009**
- [14] R. D. Armstrong, S. Zhou, *Corrosion Science*, **1988**, *28*, 1177
- [15] S. Tierce, N. Pebere, C. Blanc, C. Casenave, G. Mankowski, H. Robidou, D. Vaumousse, J. Lacaze, *Int. J. of Cast Metals Research*, **2005**, *18*, 370-376
- [16] G. Altenpohl, Aluminium: Technology, applications and environments-A profile of a modern metal, The Aluminium Association & The Minerals, Metals and Materials Society
- [17] J. R. Terrill, C. N. Cochran, J. J. Stokes, W. E. Haupin, *American Welding Society Spring Meeting*, Cleveland **1970**
- [18] J. Lacaze, S. Tierce, M.-C. Lafont, Y. Thebault, N. Pebere, G. Mankowski, C. Blanc, H. Robidou, D. Vaumousse, D. Daloz, *Materials, Science and Engineering*, **2005**, *413-414*, 317-321

## References

---

- [19] Q. Shi, F. Liang, B. Cheadle, *Corrosion*, **2004**, *60*, 492-500
- [20] R. Benedictus, S. D. Meijers, A. J. Wittebrood, J. H. W. de Witt, *Aluminium Alloys*, **1998**, 1577
- [21] G. J. Marshall, R. K. Bolingbroke, A. Gray, *Metall. Trans.*, **1993**, *24A*, 1935-1942
- [22] D. T. L. Alexander, A. L. Greer, *Acta Mater.*, **2002**, *50*, 2571-2583
- [23] S. Wernicke, R. Pinner, P.G. Sheasby, *The surface treatment and finishing of aluminium and its alloys*, ISBN: 0-904477-09-6
- [24] <http://aluminium.matter.org.uk>
- [25] Aluminium Taschenbuch, *Aluminium-Zentrale Düsseldorf*, ISBN 3-87017-106-5
- [26] J.R. Galvele, S.M. De Micheli, *Corrosion Science*, **1970**, *10*, 795-807
- [27] I.L. Muller, J.R. Galvele, *Corrosion Science*, **1977**, *17*, 179-193
- [28] V. Guillaumin, G. Mankowski, *Corrosion Science*, **1999**, *41*, 421-438
- [29] A. Afseth, J. H. Nordlien, G. M. Scamans, K. Nisancioglu, *Corrosion Science*, **2001**, *43*, 2093-2109
- [30] A. Afseth, J. H. Nordlien, G. M. Scamans, K. Nisancioglu, *Corrosion Science*, **2001**, *43*, 2359-2377
- [31] J. T. B. Gundersen, A. Aytac, S. Ono, J. H. Nordlien, K. Nisancioglu, *Corrosion Science*, **2004**, *46*, 265-283
- [32] V. S. Sinyavskii, V. V. Ulanova, V. D. Kalinin, *Protection of metals*, **2004**, *40*, 481-490
- [33] M Zamin, *Corrosion*, **1981**, *37*, 627-632
- [34] R. Iler, *The chemistry of Silica*, ISBN 0-471-02404-X
- [35] J. D. Willey, *Mar. Chem.*, **1974**, *2*, 239
- [36] R. Gout, G. S. Pokrovski, J. Schott, A. Zwick, *Journal of Solution Chemistry*, **2000**, *29*, 1173-1186
- [37] R. Iler, *The colloid chemistry of silica and silicate*, Cornell University Press **1955**
- [38] S. Sjöberg, *J. Non-Cryst. Solids*, **1996**, *196*, 51
- [39] C. F. Baes, Jr., R. E. Mesmer, *The Hydrolysis of Cations* (Wiley, New York) 1976
- [49] P. C. Carmen, *Trans. Faraday Soc.*, **1940**, *36*, 964
- [50] J. L. Bass, G.L. Turner, *J. Phys. Chem.*, **1997**, *101*, 106-38
- [51] I. Halasz, M. Agarwal, R. B. Li, N. Miller, *Catal. Lett.* **2007**, *117*, 34

## References

---

- [52] F. J. Hingston, M. Raupach, *Aust. J. Soil Res.*, **1967**, 5, 295-309
- [53] S. P. Kumaraguru, B. Veeraraghavan, B. N. Popov, *J. of the Electrochemical Society*, **2006**, 153, B253-B259
- [54] T. L. Barr, S. Seal, H. He, J. Klinowski, *Vacuum*, **1995**, 46, 1391-1395
- [55] T. L. Barr, S. Seal, S. Krezoski, D. H. Petering, *Surface and Interface Analysis*, **1996**, 24, 99-112
- [56] J. J. Hahn, N. G. McGowan, R. L. Heimann, T. L. Barr, *Surface and Coatings Technology*, **1998**, 108-109, 403-407
- [57] S. Seal, T. L. Barr, S. Krezoski, D. Petering, *Applied Surface Science*, **2001**, 173, 339-351
- [58] E. Tada, G. S. Frankel, *J. of Electrochemical Society*, **2007**, 154, C312-C317
- [59] E. Tada, G. S. Frankel, *J. of Electrochemical Society*, **2007**, 154, C318-C325
- [60] The Aluminium Association, Registration Record Series Teal Sheets, **2006**
- [61] ASTM Designation: G 85 – 85, Standard practice for modified salt spray (fog) testing, **1990**
- [62] C. H. Hamann, W. Vielstich, *Elektrochemie*, 3. Auflage, ISBN 3-527-27894-X
- [63] M.A. Legodi, D. de Waal, *Spectrochimica Acta*, **2007**, A 66, 135-142
- [64] F. Andreatta, A. Turco, I. de Graeve, H. Terryn, J. H. W. De Witt, L. Fedrizzi, *Surface & Coatings Technology*, **2007**, 201, 7668-7685
- [65] NIST X-ray Photoelectron Spectroscopy Database, <http://srdata.nist.gov/xps>

## **Erklärung**

Ich versichere, dass ich die von mir vorgelegte Dissertation selbständig angefertigt, die von mir benutzten Quellen und Hilfsmittel vollständig angegeben und die Stellen der Arbeit – einschließlich Tabellen, Karten und Abbildungen-, die anderen Werken dem Wortlaut oder dem Sinn nach entnommen sind, in jedem Einzelfall als Entlehnung kenntlich gemacht habe; dass diese Dissertation noch keiner anderen Fakultät oder Universität zur Prüfung vorgelegen hat; dass sie – von unten angegebenen Teilpublikationen - noch nicht veröffentlicht worden ist sowie, dass ich eine solche Veröffentlichung vor Abschluss des Promotionsverfahrens nicht vornehmen werde. Die Bestimmungen der Promotionsordnung sind mir bekannt. Die von mir vorgelegte Dissertation ist von Professor Gerd Meyer betreut worden.

Köln, den \_\_\_\_\_

Datum

\_\_\_\_\_

Unterschrift

## **Publications and presentations**

Kathrin Schäuble, Electrochemical study of evaporators compared to SWAAT testing, Presentation at the 5. International Congress „Aluminium Brazing”, Düsseldorf, Germany, 2008

Kathrin Schäuble, Ulrich Jüptner, Herman Terryn, Gerd Meyer, Electrochemical Analysis versus SWAAT, Proceedings ASST 2009, Leiden, The Netherlands 2009

## Acknowledgement

My time as a PhD researcher in Düsseldorf, Brussels and in Cologne was a great experience. Apart from the interesting subject it was amazing to meet several people as colleagues and to have them now as friends. Due to that I am very glad to have now the chance to thank everybody.

The most important person to name is of course Professor Herman Terryn from the Department of Materials and Chemistry, Research Group of Electrochemical and Surface Engineering from the Vrije Universiteit of Brussel. No matter how desperate and doubtful I was during my work he always found the right words and suggestions to bring me back on the right way!

Words are probably not enough to thank for all the support I received from him, anyway I will try it.

Thanks for everything!

Thanks also to my supervisor Professor Gerd Meyer from the Institute of Inorganic Chemistry from the University of Cologne. Thanks for giving me the chance to perform this thesis and for the support during the last 3 years.

It was a great pleasure and honour for me to be part(-time member) of the Department of Materials and Chemistry at the VUB. Thanks a lot to everybody for the help, the patience and the kindness to me. I will definitely miss the nice events in the department!! And since I definitely bothered some of the smurfs more than others I have to apologize for that to a few in particular:

**Fabiola**, thanks for all the help and for answering all my annoying questions and in particular for reading and reading and reading and refining all of my boring stuff.

And of course apart from work, thanks for making my time in Brussels so much fun!! It would have been very quite without you...

**Belen**, besides Fabiola you probably suffered the most with reading and refining my thesis. Thanks a lot for this! And apart from that, thanks for all the funny time independent of work!

**Oscar**, thanks for your patience, your support with all the measurements and of course for fixing everything that I destroyed..

**Marc**, thanks a lot for the long sessions in front of the FE-SEM and the great images for my work!

**Yves**, actually if I had problems that I did not know how to solve them I asked you! Thanks for having always good suggestions!

**Carine**, thanks for helping me so much with finding accommodation during all my stays. Every time I arrived in Brussels I was really curious to see which condition of living will expect me...

**Roberto**, thanks for sharing the passion for considering the amazing behaviour of Silica and all the interesting discussions concerning that topic.

**Kitty and Priya**, thanks a lot for the support and the help with Raman and IRSE.

And thanks again to everybody for making my stay at the VUB to such a great experience.

Of course I have to thank Henkel for sponsoring my research. Thanks to all my supervisors and colleagues with whom I have worked.

**Dr. Ulrich Jüptner, Dr. Marco Bastian and Dr. Jens Krömer**, thanks for giving me the chance to perform this interesting work at Henkel and the support during the last three years.

**Dipl. Ing. Andreas Nowak**, thanks for all the help, information and enthusiasm about the wonderful world of aluminium pre-treatment!

**Dr. Kirsten Lill**, thanks for attending and supporting me during the entire duration of this thesis. Sincere thanks for taking care of me and my work and tolerating my in your lab although you have never been my official supervisor..

And of course, thanks to all the colleagues being around and answering all my annoying questions!

Last but not least I would like to thank my family. My mother, my father and my sister, who always supported me.